R & M No.3827

R &M No.3827

PROCUREMENT EXECUTIVE, MINISTRY OF DEFENCE

Aeronautical Research Council
Reports and Memoranda

WIND TUNNEL TESTS ON CAMBERED WINGS OF MILD GOTHIC PLANFORM

Parts I and II

by

P.J. Butterworth and P. Lee

Aerodynamics Department, RAE Farnborough, Hants

London: Her Majesty's Stationery Office
1978

PRICE £9 NET

WIND TUNNEL TESTS ON CAMBERED WINGS OF MILD GOTHIC PLANFORM

PART I: FURTHER LOW-SPEED TESTS

by P.J. Butterworth

PART II: TRANSONIC TESTS

by P. Lee

Aerodynamics Department, RAE Farnborough, Hants

Reports and Memoranda No.3827*

February 1977

SUMMARY

Measurements are reported of the longitudinal characteristics of seven wings of mild gothic planform, aspect ratio 1.4, sharp leading edges, and two different thickness ratios. Five of these were cambered to keep the flow attached at the leading edges at lift coefficients of 0.1 or 0.2 The remaining two were symmetrical. Transition was fixed artificially, so preventing separation further downstream on the cambered wings.

All the wings were tested at low speeds and the results complement the transition-free data on three of the wings in ARC CP No.1163. Transonic testing covered a range of Reynolds and Mach numbers on a representative cambered wing.

* Replaces RAE Technical Reports 77018 and 77006 - ARC 37556 and 37523

LIST OF CONTENTS

Part I

Part II

Part I

FURTHER LOW-SPEED TESTS

by

P.J. Butterworth

SUMMARY

The low-speed longitudinal characteristics have been investigated for five cambered and two symmetric wings of mild gothic planform. These were designed, using a linear theory, for attached leading-edge flow at the low values of lift coefficient typical of the cruise of slender aircraft. The purpose of the investigation was to check that cambered wings designed in this way can produce, at the higher lift coefficients appropriate to take-off, substantial reductions in drag relative to a symmetric wing.

The wings all had thickness/chord ratios of 0.09 or 0.04. The cambered wings were designed to have attached leading-edge flow at various values of lift coefficient and position of the centre of pressure.

The force-measurement and flow-visualisation tests show that the design criteria have almost been achieved though inboard separations were observed under transition-free flow conditions. However, roughness bands applied near the leading edges suppressed these separations and the force results which are analysed in detail were all obtained with boundary-layer transition fixed.

1 INTRODUCTION

Possible layouts of slender-wing passenger aircraft which have been considered and tested in recent years include a symmetric thick wing in combination with various forebodies and a similar thinner wing with a conventional aircraft body[1]. These types of aircraft, though having low drag when in a cruise condition, incur a high drag penalty at lift coefficients appropriate to take-off and landing. If such aircraft are flown over short ranges a considerable proportion of their flight occurs at low speeds. The operating economy is then improved if the drag at higher values of the lift coefficient can be reduced without penalising the cruise condition.

As the drag of the wing is the major component of the total drag of such an aircraft, camber could be very effective in improving the performance. To explore the effect of camber, tests have been made on five cambered wings. These were designed for attached-flow conditions at lift coefficients such that, on available evidence (eg Ref 2), substantial reductions should be achieved in drag (compared to a symmetric wing) at the higher lift coefficients appropriate to take-off and landing conditions.

The models were tested in the 4ft × 3ft low-speed wind tunnel at RAE Farnborough with boundary-layer transition from laminar to turbulent either free, or fixed by strips of roughness inboard of the leading edges. The results of transition-free tests on one of the symmetric wings and two of the cambered wings have already been published[3]. It subsequently became evident (see Part II) that under transition-free flow conditions the flow separated from the upper surface of the models near the attached flow condition in a manner which could be suppressed by suitable transition fixing.

Lift, drag and pitching moment were measured on all seven wings at a wind speed of 61 m/s (corresponding to a Reynolds number of 2×10^6 based on the planform centreline chord). Although both transition-free and fixed measurements were taken, emphasis is placed on the transition-fixed results since they are probably more representative of full-scale flow conditions. Where differences do exist, they are related to the existence of upper-surface separations in the transition-free flow field.

Transition-free flow visualisation patterns were obtained at a wind speed of 30.5 m/s and a limited amount of surface static-pressure measurement was carried out on one of the cambered wings to evaluate the effectiveness of the roughness bands used to fix transition.

2 MODEL DETAILS

The planform of all seven wings is given by:

$$\frac{y}{s_T} = \frac{s(x)}{s_T} = 0.25\left[5\left(\frac{x}{c}\right) - \left(\frac{x}{c}\right)^5\right]$$

where s_T is the wing trailing-edge semispan (= 0.1905 m) and c is the centre-line chord (=0.4717 m) (see Fig 1).

The half-thickness distribution is given by:

$$\frac{z}{c} = \frac{B(x)}{c}\left(1 - \frac{y^2}{s(x)^2}\right)$$

where z is the half-thickness, $s(x)$ is the local semispan and $B(x)$ is the centreline thickness distribution which is given by:

$$\frac{B(x)}{c} = \frac{t}{c}\left(\frac{x}{c}\right)\left(1 - \frac{x}{c}\right)\left[3.2471 - 7.5777\left(\frac{x}{c}\right) + 17.8647\left(\frac{x}{c}\right)^2 - 19.2073\left(\frac{x}{c}\right)^3 + 7.6754\left(\frac{x}{c}\right)^4\right].$$

In this equation, t/c is the maximum thickness/chord ratio which equals 0.09 or 0.04 for the thick and thin wings respectively.

The linear theory used to design the cambered wings[4] requires the evolution of a suitable loading distribution for attached flow at the edges of an infinitely thin wing. This loading distribution defines the value of the lift coefficient and the position of the centre of pressure at the attached flow condition (written as $(C_L)_{des}$ and $\left(\frac{x_{c.p.}}{c}\right)_{des}$ respectively). The linear theory then relates the specified loading to the streamwise slope of the camber surface and definition of the trailing-edge shape enables the camber surface to be defined by integration. The incidence at which attached flow is expected (α_{des}) is defined by the angle between the line joining the apex and the centre of the trailing edge and the $z = 0$ plane.

A loading distribution which is zero everywhere defines a flat camber surface with $(C_L)_{des} = 0$, $\alpha_{des} = 0$; $\left(\frac{x_{c.p.}}{c}\right)_{des}$ is indeterminate. This type of camber surface is referred to throughout this Report as 'A'.

It was estimated from previous work on the effects of planform[5] and thickness[6] that at $\alpha_{des} = 0^o$ an uncambered 9% thick wing would have the aerodynamic

centre 0.533c downstream of the apex and this position was chosen as the design centre of pressure for the first two cambered wings. To obtain substantial reductions in drag in the C_L range $0.4 \rightarrow 0.5$, Ref 2 suggests that the camber surface should be designed for $(C_L)_{des} \doteqdot 0.2$ but the design should neither compromise the cruise condition nor exceed the limitations of the linear design theory. For this reason the first two non-zero loading distributions were chosen so that $\left(\frac{x_{c.p.}}{c}\right)_{des} = 0.533$, $(C_L)_{des} = 0.1$ and 0.2 and the trailing edges of the camber surfaces were defined to lie in the $z = 0$ plane to retain compatibility with 'A'. The resultant camber surfaces are referred to as 'B' $[(C_L)_{des} = 0.1]$ and 'C' $[(C_L)_{des} = 0.2]$ and they are geometrically related since the z-ordinate of 'C' is twice that of 'B' everywhere, the loading distribution used to design 'C' being double that of 'B' everywhere. Thus $(C_L)_{des}$ is doubled, the streamwise slope (and hence z-ordinate) of the camber surface is doubled but $\left(\frac{x_{c.p.}}{c}\right)_{des}$ is the same.

The tests described in Ref 3 (on surfaces 'A', 'B' and 'C' with the $t/c = 0.09$ thickness distribution) showed that the theoretical and experimental values of $\frac{x_{c.p.}}{c}$ at $(C_L)_{des}$ differ substantially. To explore this difference further, a new camber surface was designed with $(C_L)_{des} = 0.1$ and $\left(\frac{x_{c.p.}}{c}\right)_{des} = 0.483$. This surface is referred to as 'B''.

A fifth camber surface, referred to as 'B,Gull' is a direct derivative of 'B'; $(C_L)_{des}$, $\left(\frac{x_{c.p.}}{c}\right)_{des}$ and α_{des} are the same but the trailing edge is chosen not to lie in the $z = 0$ plane. Theoretically the performance of the camber surface is only dependent upon longitudinal camber and therefore changes in the spanwise-section shapes due to a non-linear trailing-edge shape have no effect provided the streamwise slopes of the camber surface are unchanged. Therefore, 'B,Gull' as defined in Fig 3 should behave in the same manner as 'B'. The trailing-edge shape of 'B,Gull' was evolved from consideration of aircraft noise problems: substantial reductions in observed noise on the ground can be gained for a slender wing with overwing engines but there is still the problem of sideline noise at take-off and landing. If the engines could be sited in a hollow on the wing's upper surface, there would be a reduction in sideline noise due not only to the shadowing effect of the wing but also to the beneficial refractive effects of a smooth curved surface[7]. A suitable hollow was achieved by defining the trailing edge to have inboard dihedral with a smooth continuation to anhedral outboard. A further advantage of this type of surface is that it has been found that anhedral outboard on a slender wing gives an improvement in lateral stability[8].

The camber-surface planform and centreline thickness distributions are shown in Fig 1, typical chordwise camber distributions in Fig 2 and spanwise camber and thickness distributions in Fig 3. The relevant design parameters of the seven models tested are given in Table 1. The wings are referred to by their camber surface and t/c ratio as summarised below:

Camber surface	t/c
A	0.04, 0.09
B	0.04, 0.09
C	0.09
B'	0.09
B,Gull	0.09

Since a linear theory is used, the effects of camber and thickness are additive; for the cambered wings, in the cross-flow plane, the thickness is added normal to the camber surface. The addition of the thickness is described in detail in Ref 4. In Table 1 it will be noticed that the thickness/chord ratios (defined as usual at right angles to the incidence datum) of the cambered wings differ slightly from those of the corresponding symmetric wings (A,0.09 and A,0.04). This is a result of the slightly increased centreline chord of the cambered wings and the way in which the thickness distribution has been added to the camber surface.

3 PRELIMINARY EXPERIMENTS ON TRANSITION FIXING AND DETAILS OF TESTS

The method for observing the surface air-flow on a model in the 4ft × 3ft wind tunnel which has been found to give best definition requires a suspension of lampblack in paraffin to be painted on the surface and then the tunnel run up to speed. A limitation of this method is that it is impossible to obtain with certainty flow visualisation patterns at wind speeds above about 50 m/s, as the paraffin evaporates before the tunnel is run fully up to speed. Normally, flow visualisation patterns on slender-wing models in the 4ft × 3ft tunnel obtained at 50 m/s differ little from those at lower speeds; a speed of 30.5 m/s (100 ft/s) was chosen to avoid any danger of evaporation before the tunnel is on speed.

Before the effectiveness of the roughness bands used to fix transition was established, all the wings were tested under transition-free conditions. The flow visualisation patterns showed separations inboard of the leading edges at the attachment condition and certain anomalies existed in the force results, notably in;

(i) the relationship between the values of minimum drag coefficient of the two symmetric wings (A,0.09 and A,0.04),

(ii) a pitching-moment instability near the attachment condition of the four t/c = 0.09 cambered wings, and

(iii) a very low value of the linear component of normal force for wing B,0.09.

The latter two of these observations are reminiscent of the results of tests on a 16% thick symmetric slender wing previously tested in the 4ft × 3ft low-speed tunnel[6]. On this wing, in the region of $\alpha = 0^{o}$, the transition-free flow separated from both surfaces just downstream of the point of maximum thickness giving abnormal lift characteristics and longitudinal instability. However, roughness bands near the leading edges fixed transition and the separations were suppressed, sensible force and moment characteristics being obtained.

Further evidence of the need to fix transition came from comparison with tests, described in Part II, on a larger model of B,0.09 which was tested at higher wind-speeds and Reynolds number in the 8ft × 6ft transonic tunnel at RAE, Farnborough. At low speeds the results of transition-free tests in the two tunnels agree but the pitch instability problem is accentuated by increasing Mach number (see Part II). However, it was found that the 'standard' transition fix used in the transonic tunnel eliminated this instability.

Therefore it was considered necessary to retest all the 4ft × 3ft tunnel models with similar transition fixing. The roughness bands used on the models were 3 mm wide and were positioned 6.5 mm inboard of the leading edges on both surfaces (see Fig 1). They consisted of small glass balls (ballotini) sprinkled on bands of glue. The diameters of the glass balls were in the range 0.18 mm to 0.21 mm, giving a Reynolds number of 820 based on the mean diameter at the wind speed of 61 m/s (200 ft/s) used for the force tests.

Because of the speed limitation on flow visualisation techniques mentioned earlier, some crude surface static pressure measurements were made at speeds up to 61 m/s, at various stations in the region of separated flow, to establish the effectiveness of the transition bands. Two typical spanwise pressure distributions are shown in Fig 4 for wing B,0.09 at the incidence at which attached flow was anticipated. These show that separations occur on the upper surface of the cambered wings under transition-free conditions giving an increase in local lift towards the trailing edge and resulting in a nose-down pitching moment. As the incidence is increased above the 'attachment incidence', these separations are suppressed by the developing vortex flow (see Fig 6). The effects of the separations over a wider incidence range are discussed in section 5.

Forces on the seven wings were measured with roughness bands on both wing surfaces. The wind speed for these tests was 61 m/s ($R = 2 \times 10^6$ based on the planform centreline chord). The models were suspended in the tunnel by a conventional wire rig and the raw data was reduced to coefficient form taking account of tunnel blockage and constraint[9] and the effects of the wires[10]. The forces and moments presented in Table 3 are non-dimensionalised with respect to the actual area and centreline chord of the camber surface. (These differ slightly from those of surface 'A' as shown in Table 1.) The pitching moment coefficients are referred to an axis 0.54c from the wing's apex for all seven wings.

4 FLOW VISUALISATION TESTS

These tests were made with the models mounted on a sting attached to the lower surface. For each model a range of angle of incidence up to 25° was investigated and at some incidences the flow patterns were photographed. All the flow patterns are of transition-free flow at a wind speed of 30.5 m/s ($R = 1 \times 10^6$ based on the planform centreline chord). Some of these pictures are reproduced in Figs 5, 6 and 7. Fig 5 shows flow patterns on wings at α_{des}, Fig 6 at $(\alpha_{des} + 10^\circ)$ and Fig 7 at $(\alpha_{des} + 15^\circ)$.

At the attachment incidence (Fig 5) the flow is seen to be attached at the leading edges on all the cambered wings though a separation is visible inboard. This separation appears to start near the apex and affects a large portion of the wing area. This is the separation that the leading-edge roughness bands suppress at the higher wind speed used for the force tests. There is also another separation near the apex visible on the photographs of wings B,0.04; C,0.09 and B',0.09. This is a weaker separation closer to the centreline which persists at higher incidences and Reynolds number. This is verified by Fig 8 which shows a flow pattern on a larger version of B,0.09 which effectively has transition fixed by the many strips of sellotape covering surface static-pressure-measurement tappings. This figure shows that the separation on B,0.09 visible in Fig 5 is suppressed but the second, weaker separation near the apex still persists at the higher Reynolds number of 4×10^6. (Fig 8 is taken from Ref 12.)

At $(\alpha_{des} + 10^\circ)$ it can be seen (Fig 6) that the leading-edge vortices are well established and the strong separations visible in Fig 5 are suppressed by the developed vortex even at the flow visualisation speed of 30.5 m/s. However, on the cambered wings, the weaker separation has become more evident and weak vortices are seen to be swept downstream. The same comments apply to Fig 7 though the swept vortices moved inboard as the incidence was increased (presumably influenced by the inboard movement and strengthening of the leading-edge vortices).

It seems unlikely that these separations near the apex of the model wings with extreme upper surface curvature can be affected by roughness alone and the extent to which they would exist in full-scale flow is conjectural; dependent as they are on the interaction between the pressure gradient associated with the surface curvature and the boundary layer.

More important than this are the wider effects of thickness, camber and incidence on the development of the primary leading-edge vortices (Figs 6 and 7)*.

Comparison of the flow patterns on A,0.09 and A,0.04 (or B,0.09 and B,0.04) shows that at a given angle above the attachment incidence, the primary leading-edge vortices are further inboard on the thin wings than on the thick (*cf* Ref 11). Also, they are further inboard on the symmetric wings 'A' than on the cambered wings 'B' and on C,0.09 they are further outboard than on B,0.09, ie increased camber or thickness impedes the inboard movement of the leading-edge vortices thus implying that the spanwise position of the leading-edge vortices is dependent upon the local slope of the wing surface.

Fig 9 attempts to quantify these effects by showing, at a chordwise station 0.6c from the apex, the point of inflection of the surface flow pattern under the primary leading-edge vortex. The values shown have been measured from photographs such as those in Figs 6 and 7 for wings A,0.09; A,0.04; B,0.09; B,0.04 and C,0.09.

5 FORCE MEASUREMENTS

The results of the force tests on the wings are given in Table 3 and are plotted in Figs 10 to 25.

To establish the limits of the linear design theory for the cambered wings, the analysis of the results of the force tests on the seven wings is discussed in four sections to show:

(a) the effects of varying $(C_L)_{des}$. (Surfaces 'A', 'B' and 'C');

(b) the interaction of camber and thickness (Wings A,0.09; A,0.04; B,0.09 and B,0.04);

(c) the effects of varying $\left(\frac{x_{c.p.}}{c}\right)_{des}$. (Surfaces 'B' and 'B'');

(d) the effects of trailing-edge shape. (Surfaces 'B' and 'B,Gull').

---

* The model A,0.04 on which these flow patterns were obtained was not the model used for the force tests, but was that used in Ref 1 where the effects of deflecting trailing-edge controls were examined. A new model without controls was used for the force tests described here.

Sections (a), (c) and (d) involve the analysis of results for 9% thick wings and (b) shows the interaction between camber and thickness, though near the design condition this effect is small.

5.1 Lift and normal force

The lift characteristics of the seven wings are plotted in Figs 10 to 12. Fig 10 shows the effects of fixing transition for both thick and thin volume distributions on surfaces 'A' and 'B' and for C,0.09. It can be seen that fixing transition on wings B,0.09 and C,0.09 incurs a very small decrement in C_L near the 'attachment incidence'. This is in agreement with the surface static pressure measurements mentioned in section 3 which showed that with fixed transition the upper-surface flow separations (visible in Fig 5) are suppressed with a consequent loss in local lift coefficient. In transition-free flow, on B, 0.09, this separation persists at incidences above the attachment incidence though by $\alpha = 8^o$ it is suppressed by the developing leading-edge vortices. The results for C,0.09 show that at incidences sufficiently lower than α_{des}, when the pressure gradient causing the separation is less severe, there is no difference between the transition-free and fixed results.

The results for B,0.04 (Fig 10b) show no effects of fixing transition though the flow pattern in Fig 5 shows separations on the upper surface. This would imply that on B,0.04 the upper surface separation is suppressed by increasing the Reynolds number from 1×10^6 (used for the flow pattern) to 2×10^6 (used for the force test) without the use of roughness bands.

Similarly for the uncambered wings (with their gentler surface gradient) there is no difference in the lift results although Ref 13 shows that the problem of separations near the trailing edge can arise at low Reynolds number on some 8% thick symmetric wings.

Figs 10a and b show that at high incidences, there is no systematic change in the lift coefficients between transition-free and fixed conditions, thus implying that the roughness bands do not affect the development of the leading-edge vortices on any of the wings.

The flow visualisation patterns show that at the design 'attachment incidence' of each cambered wing, the flow is attached at the leading edges and from Fig 11 it can be seen that the value of C_L at α_{des} (written as $(C_L)_{\alpha_{des}}$) is close to the theoretical value of $(C_L)_{des}$ given in Table 2. The maximum difference (for wings B',0.09 and B,0.09,Gull) is 0.006.

Ref 6 shows that the linear component of normal force and the point of action of this linear component are approximately linearly dependent upon wing thickness. If one linearly extrapolates $(C_L)_{\alpha_{des}}$ for wings B,0.09 and B,0.04 to zero thickness, $(C_L)_{\alpha_{des}}$ for surface 'B' is 0.0993. The difference of 0.0007 between $(C_L)_{des}$ and $(C_L)_{\alpha_{des}}$ is equivalent to an error of 0.03^o in measured angle of incidence, which is within the accuracy of measurement. Thus to the accuracy of the tests, camber surface 'B' realises its design value of C_L but the addition of the thickness distribution with $t/c = 0.09$ reduces $(C_L)_{\alpha_{des}}$ to 0.098 (ie 2% lower). Since camber surfaces 'B' and 'C' are related and since $(C_L)_{des} - (C_L)_{\alpha_{des}}$ for C,0.09 is also approximately 2% of $(C_L)_{des}$, it is reasonable to assume that the same result applies for surface 'C'.

However, surfaces 'B'' and 'B,Gull' with the same dependence on thickness give values of $(C_L)_{\alpha_{des}}$ for zero thickness approximately 8% in excess of the design values. So, even though the design value of C_L was the same for 'B', 'B'' and 'B,Gull', the shape of the camber surface* and of the trailing edge have an important influence on $(C_L)_{\alpha_{des}}$.

Using the values of $(C_L)_{\alpha_{des}}$ in Table 2 it is possible to collapse the lift curves of the cambered wings so that their attachment conditions coincide with those of the symmetric wings. In Fig 12 $\left[C_L - (C_L)_{\alpha_{des}}\right]$ is plotted against $(\alpha - \alpha_{des})^o$ and for clarity the thin wing results are separated from the thick wing results.

To understand the relationship between the lift characteristics of the cambered and symmetric wings, it is useful to analyse the normal force characteristics with regard to the linear component and the occurrence of vortex breakdown. For a symmetric wing, the normal force may be split into its linear and non-linear components[14]:

$$C_N = C_{N_{linear}} + C_{N_{non\text{-}linear}}$$

$$= a\alpha + C_{N_{n.l.}} \quad .$$

The parameter a is determined by the intercept on the C_N/α axis of a plot of C_N/α versus α. The analogous definition for a cambered wing is:

$$C_N = (C_N)_{\alpha_{des}} + a(\alpha - \alpha_{des}) + C_{N_{n.l.}} \quad .$$

---

* The difference between $\left(\frac{x_{c.p.}}{c}\right)_{des}$ and $\left(\frac{x_{c.p.}}{c}\right)_{\alpha_{des}}$ for B',0.09 is significantly larger than for B,0.09 (section 5.3) and it is unlikely that this large error could exist with $(C_L)_{\alpha_{des}}$ little or no different to $(C_L)_{des}$ for B',0.09.

To determine a in this equation it is necessary to plot $\left[C_N - (C_N)_{\alpha_{des}}\right]/(\alpha - \alpha_{des})$ against α and find the value of this function when $\alpha = \alpha_{des}$. This generalised form of C_N/α is plotted in Figs 13 and 14. The inflection of the C_N/α curves at moderate-to-high incidences is attributable to vortex breakdown[1,13].

Consider now $\left[C_L - (C_L)_{\alpha_{des}}\right]$ for the wings A,0.09; B,0.09 and C,0.09 which are three members of a family of cambered wings; at values of $(\alpha - \alpha_{des}) < 15^\circ$, Fig 12 shows that the value for B,0.09 is 4% below that for A,0.09, and the value for C,0.09 is less than 8% below. Although the design of the cambered wings makes no assumptions regarding the $C_L \sim \alpha$ relationship for separated flow, this result shows that the effects of adding thickness and camber to a specified planform are small even for the extreme camber of 'C'.

At higher values of $(\alpha - \alpha_{des})$, $\left[C_L - (C_L)_{\alpha_{des}}\right]$ for B,0.09 equals the value for A,0.09 and this is due to the different effects of vortex breakdown on these two wings. Fig 13 shows that the break in the C_N/α curves indicating vortex breakdown occurs on B,0.09 near $\alpha = 16^\circ$ and is less severe than on A,0.09 where it occurs slightly earlier. Since there is little difference in the linear component of the normal force on the two wings (a = 1.640 and 1.576 for A,0.09 and B,0.09 respectively) the different effects of vortex breakdown account for the crossover of the $\left[C_L - (C_L)_{\alpha_{des}}\right]$ curves in Fig 12.

Fig 11 shows that at all incidences above the attached flow incidence, the thin wings (A,0.04 and B,0.04) produce more lift than the corresponding thick wings (A,0.09 and B,0.09). This increased lift is due to the increased linear component of normal force (*cf* Ref 6) and the delaying of vortex breakdown to a higher incidence on the thin wings (see Fig 13). The incremental change in C_L due to reduced thickness on camber surface 'B' is less than that on the symmetric wing 'A' and Fig 12 shows that the thin cambered wing produces an increasing loss in C_L with increasing α relative to the thin symmetric wing (unlike the thick wing relationship mentioned above). Quantitatively, $\left[C_L - (C_L)_{\alpha_{des}}\right]$ for B,0.04 is not more than 6% lower than that for A,0.04 at any value of $(\alpha - \alpha_{des})$.

Figs 11 and 12 show that at a given incidence above the attachment incidence, the values of C_L for B,0.09 and B',0.09 are similar. However, as the analysis in Fig 14 indicates, B',0.09 has the greater linear component of normal force offsetting the smaller non-linear component; consequently the cumulative effect of cambering the wing to move the centre of pressure forward leads to the lift curve passing through the design point without significant change of shape.

B,0.09,Gull produces considerably more lift than B,0.09 at all incidences (Fig 11) because $(C_L)_{\alpha_{des}}$ is larger, the linear component of normal force is

larger and B,0.09,Gull is not affected by vortex breakdown until $\alpha = 23^{o}$, (see Fig 14). In this last respect, B,0.09,Gull is unique amongst the cambered wings tested: surfaces 'B', 'C' and 'B'' suffer vortex breakdown at about the same value of centreline angle of incidence as 'A', ie for the 9%-thick wings (except B,0.09,Gull) vortex breakdown occurs in the range 13^{o} to 17^{o} and for the thin wings in the range 20^{o} to 22^{o}. Thus the addition of trailing-edge shape to a camber surface, which gives advantageous noise shielding and lateral stability characteristics, can also significantly improve the lift characteristics.

5.2 Drag and axial force

Fig 15 shows that for the cambered wings the laminar drag bucket associated with transition-free flow exists over a range of C_L which includes probable aircraft cruise values. Therefore to compare the drag characteristics of the wings it is essential to use the transition-fixed results which are plotted in Figs 16 and 17.

The types of camber considered here have the effect of transferring the minimum point of the drag polar of the symmetric wing to a positive value of C_L and increasing the minimum value of C_D. All the cambered wings achieve reductions in drag compared with the corresponding symmetric wing at values of C_L greater than $0.8 \times (C_L)_{des}$. To assess their performance throughout the C_L range, the induced-drag factor K is used where

$$C_D = C_{D_0} + \frac{K}{\pi A} C_L^2 ,$$

and C_{D_0} is the minimum value of C_D of the corresponding symmetric wing (ie the value at $C_L = 0$). For a symmetric wing the function K is approximately constant, but for a cambered wing it is a non-linear function of C_L and clearly shows the range of lift coefficient where the largest reductions in C_D have been achieved. (K is plotted against C_L in Fig 18.)

The function K will not, however, show whether the shape of the drag polar has been changed by camber and to investigate this it is necessary to consider a modified function K' where

$$C_D = C_{D_m} + \frac{K'}{\pi A} \left(C_L - C_{L_m}\right)^2$$

and $\left(C_{L_m}, C_{D_m}\right)$ defines the point at which the drag is a minimum*. K' is plotted against $\left(C_L - C_{L_m}\right)$ in Fig 19; for a symmetric wing $K' = K$.

Fig 19 shows the values of K' for A,0.09; B,0.09 and B',0.09 to be similar throughout the range of $\left(C_L - C_{L_m}\right)$; however for C,0.09 K' is up to 20% larger and for B,0.09,Gull approximately 9% smaller. It would appear that the camber of C,0.09 has exceeded the limits of the design theory since the shape of the drag polar has been considerably altered with adverse effects. On the other hand shaping of the trailing edge as represented by B,0.09,Gull has beneficially altered the shape of the drag polar.

For $\left(C_L - C_{L_m}\right) < 0.5$ the relationships between the values of K' for A and B with the thick or thin volume distributions are similar. However, because the onset of vortex breakdown occurs at a lower value of $\left(C_L - C_{L_m}\right)$ on B,0.04 than on A,0.04, their K' curves diverge at higher values of this coefficient with B,0.04 having substantially higher values. For B,0.09 and A,0.09 where vortex breakdown occurs at similar values of $\left(C_L - C_{L_m}\right)$, the K' curves remain close together.

Fig 18 shows that at the higher values of C_L appropriate to low-speed flight K for C,0.09 is not much less than the value for B,0.09. It also shows that for the cambered wings the lowest value of K occurs when C_L is approximately twice $(C_L)_{des}$ (ie near $C_L = 0.2$ for B,0.09 and $C_L = 0.4$ for C,0.09).

Similarly for B,0.04 the maximum reduction in K relative to A,0.04 occurs at $C_L \approx 0.2$ but the reduction rapidly diminishes with increasing C_L; note that the reduction is less than that for B,0.09 relative to A,0.09 when $C_L > 0.5$.

Camber surfaces designed for different centre of pressure positions (ie 'B' and 'B'') have K characteristics which differ little throughout the C_L-range, but the shaping of the trailing edge as represented by B,0.09,Gull produces a greater reduction in K and the maximum reduction occurs at about treble the design value of C_L (*cf* double for camber surfaces 'B', 'C' and 'B'').

Since one of the aims of the camber designs is to substantially reduce C_D at values of C_L appropriate to take-off, it is worth analysing in detail the drag of all the wings at such a typical value of C_L - say, $C_L = 0.5$. The value of C_D for each wing can be read off Figs 16 and 17 but this does not show, for example, why C,0.09 does not produce a much greater reduction in C_D relative to

---

* A method for determining C_{D_0}, C_{L_m} and C_{D_m} is given in the Appendix of Ref 3.

A,0.09 than is achieved by B,0.09. Alternatively the equation defining the axial force coefficient, C_A, may be rewritten to express C_D in terms of C_L, C_A and α, giving

$$C_D = C_L \tan \alpha + C_A \sec \alpha .$$

The table below shows how the values of C_A and α at $C_L = 0.5$ contribute to the reductions in drag achieved by the cambered wings. (C_A is plotted against C_L in Fig 20.)

Wing	$C_L = 0.5$ at $\alpha =$	$C_L \tan \alpha$	C_A at $C_L = 0.5$	$C_A \sec \alpha$	$C_D = C_L \tan \alpha + C_A \sec \alpha$	C_D Figs 16 and 17	ΔC_D	% reduction in C_D
A,0.09	12.95	0.1150	$\bar{0}$.0135	$\bar{0}$.0138	0.1012	0.1015	-	-
B,0.09	16.40	0.1471	$\bar{0}$.0533	$\bar{0}$.0555	0.0916	0.092	0.0095	9.4
C,0.09	19.50	0.1770	$\bar{0}$.0835	$\bar{0}$.0886	0.0884	0.0885	0.0130	12.8
B',0.09	18.30	0.1654	$\bar{0}$.0685	$\bar{0}$.0721	0.0933	0.0935	0.0080	7.9
B,0.09,Gull	15.70	0.1405	$\bar{0}$.0510	$\bar{0}$.0530	0.0875	0.088	0.0135	13.3
A,0.04	12.10	0.1072	$\bar{0}$.0025	$\bar{0}$.0026	0.1046	0.104	-	-
B,0.04	15.65	0.1401	$\bar{0}$.0440	$\bar{0}$.0457	0.0944	0.094	0.0100	9.6

The values of C_D calculated from $C_L (= 0.5)$, C_A and α differ slightly from those obtained from Figs 16 or 17 due to limitations in the accuracy with which values can be read from the figures.

B,0.09 achieves a substantial reduction in C_D relative to A,0.09 because the decrease in $C_A \sec \alpha$ outweighs significantly the increase in $C_L \tan \alpha$; C,0.09 achieves only a further 3.4% reduction because the decrease in $C_A \sec \alpha$ is not double that associated with B,0.09. Thus the changed shape of the drag polar of C,0.09, as mentioned earlier, results from the low absolute value of C_A. For a family of cambered wings detailed analysis of C_A is complex. For the symmetric wing C_A is determined largely by the suctions under the leading-edge vortices acting on the forward facing part of the upper surface; for a cambered wing there is also the effect of the flow associated with the design condition of the camber surface.

The relationship between the drag characteristics of the thick and thin volume distributions on surface 'A' is analysed in Ref 1. For B,0.09 and B,0.04 (relative to A,0.09 and A,0.04 respectively), the increases in $C_L \tan \alpha$ at $C_L = 0.5$ are very similar as are the decreases in $C_A \sec \alpha$.

B',0.09 achieves a lift coefficient $C_L = 0.5$ at an incidence $\alpha = 18.3^\circ$, which is only 1.9° higher than the incidence at which B,0.09 reaches this C_L, whereas the difference in α_{des} is 2.3°, ie for B',0.09, $C_L \tan \alpha$ (= 0.1654) is lower than would be expected and therefore the smaller reduction in C_D results from the smaller negative value of $C_A \sec \alpha$.

The reduced incidence of B,0.09,Gull at $C_L = 0.5$ compared with B,0.09 explains why the gull wing produces a greater reduction in C_D. Some of the reduction in $C_L \tan \alpha$ is however cancelled by the slightly smaller change in $C_A \sec \alpha$. Therefore the changed shape of the drag polar of B,0.09,Gull, as shown by its K' characteristics in Fig 19, is a result of its lower incidence for a given value of C_L.

5.3 Pitching moment

The pitching moment characteristics as plotted in Figs 21 to 23 are measured about a point 0.54c from the wing apex on the line joining the apex and the centre of the trailing edge, and are non-dimensionalised with respect to the wing centreline chord. In discussing the results, reference is made to the centre of pressure position $\frac{x_{c.p.}}{c}$ where

$$\frac{x_{c.p.}}{c} = 0.54 - \frac{C_m}{C_N}$$

and the aerodynamic centre position $\frac{x_{a.c.}}{c}$ derived from

$$\frac{x_{a.c.}}{c} = 0.54 - \frac{\partial C_m}{\partial C_N} .$$

At low values of C_L, where the flow visualisation tests and lift and drag characteristics show that separations can exist on the upper surfaces of the wings, the effects on C_m and $\frac{x_{c.p.}}{c}$ of fixing transition are shown in Fig 21. Since A,0.09 is a symmetric wing, its $C_m \sim C_L$ curves for free and fixed transition pass through the origin, and the increment in C_m between fixed and free transition tests is an odd function of C_L (ie as the sign of C_L changes so does the sign of the increment in C_m). In the transition-free tests on A,0.09, there were separations on both wing surfaces; a similar result has been observed[6] previously on a considerably thicker wing.

On B,0.09 separation occurs only on the upper surface introducing a region of instability near the design attachment condition and fixing transition gives

an increment in C_m (and consequently a decrement in $\left(\frac{x_{c.p.}}{c}\right)$ at values of $C_L < 0.15$. As the incidence of B,0.09 is increased above the attachment incidence, the leading-edge vortices tend to suppress the separation and for $C_L > 0.15$, the free and fixed transition results are indistinguishable. A similar trend is shown for C,0.09, confirming that the separation is a characteristic of the thicker wings[6].

To make a valid comparison of pitching moment characteristics, it is necessary to use the transition-fixed results; C_m (transition-fixed) is plotted against C_L and α in Figs 22 and 23 respectively. All the cambered wings exhibit a positive (nose-up) pitchimg moment near their respective design conditions, and stability characteristics similar to those of the corresponding symmetric wing through most of the incidence range. These two features of the cambered wings ensure that the trailing-edge control deflection required for trimmed flight incurs a lower drag penalty than that associated with the symmetric wings.

Fig 24 shows that the centres of pressure of the cambered wings near their design conditions move rapidly aft with increasing C_L . The position of the centre of pressure at $\alpha_{des}\left[\left(\frac{x_{c.p.}}{c}\right)_{\alpha_{des}}\right]$ obtained from the tests has been read off Fig 24 and compared with the theoretical value. The table below presents these values and shows that on all the cambered wings the experimental position is well forward of the theoretical position.

Wing	$\left(\frac{x_{c.p.}}{c}\right)_{\alpha_{des}}$	$\left(\frac{x_{c.p.}}{c}\right)_{des}$
B,0.09	0.502	0.533
C,0.09	0.503	0.533
B',0.09	0.433	0.483
B,0.09,Gull	0.515	0.533
B,0.04	0.512	0.533

There is evidence to suggest that the second separation near the apex, visible on the flow visualisation patterns (Fig 5) on all the cambered wings except B,0.09,Gull is seriously affecting the value of $\left(\frac{x_{c.p.}}{c}\right)_{\alpha_{des}}$; the pattern on B,0.09,Gull shows no such separation and its value of $\left(\frac{x_{c.p.}}{c}\right)_{\alpha_{des}}$ is greater than that for any of the other cambered wings. The absence of the second separation on B,0.09,Gull is probably due to its sections near the apex having

considerably smaller spanwise gradients than the other camber surfaces (see Fig 3). Despite the fact that the flow pattern on B,0.04 in Fig 5b ($R = 1 \times 10^6$) shows the second separation near the apex, it is possible that at the Reynolds number of the force tests ($R = 2 \times 10^6$) this second separation is suppressed. The following table presents values of $\left(\frac{x_{c.p.}}{c}\right)_{\alpha_{des}}$ derived from different transition-fixed tests on various models of B,0.09:

$\left(\frac{x_{c.p.}}{c}\right)_{\alpha_{des}}$	Reference	Reynolds number	Mach number	Derivation
0.502	Present	2×10^6	0.18	Force measurements
0.515	Part II	4.1×10^6	0.40	Force measurements
0.515	12	6.7×10^6	0.22	Force measurements
0.525	12	6.7×10^6	0.22	Integration of pressure measurements

This table shows that the tests at the highest Reynolds number and Mach number give a value of $\left(\frac{x_{c.p.}}{c}\right)_{\alpha_{des}}$ closer to the design value than the present test and this could be due to the elimination of this second separation near the apex - see section 4.

This argument implies that the values of $\left(\frac{x_{c.p.}}{c}\right)_{\alpha_{des}}$ for wings B,0.09; C,0.09 and B',0.09 given in the table are less representative of full-scale flow than those for the thinner cambered wing B,0.04 and the gull wing B,0.09,Gull.

If the discrepancy between $\left(\frac{x_{c.p.}}{c}\right)_{des}$ and $\left(\frac{x_{c.p.}}{c}\right)_{\alpha_{des}}$ is a result of a second separation near the apex, then it is consistent that for B',0.09 the discrepancy would be greater than for B,0.09 since the spanwise sections near the apex of the former are more cambered than those of the latter (see Fig 3).

For the cambered wings, the distance aft of the aerodynamic centre (Fig 25) exhibits a local minimum just above the design value of C_L, followed by movement aft with increasing incidence until the onset of vortex breakdown.

Vortex breakdown is seen in Figs 22 and 23 as an increase in the C_m curve gradient or more clearly in Fig 25 as a forward movement of the aerodynamic centre. The effect is particularly severe for A,0.09; B,0.09 and B',0.09 at a value of C_L near 0.5 and for A,0.04 at $C_L = 0.95$.

6 CONCLUSIONS

A series of cambered wings designed for attached leading-edge flow at various values of lift coefficient and centre of pressure position has been tested over a range of incidence covering both attached and separated leading-edge flow conditions.

In transition-fixed tests the existence of a second separation near the apex on some of the cambered wings (as discussed in section 5.3) appears to depend on Reynolds number and Mach number. The increment in lift due to this separation need only be very small to account for the difference in centre of pressure position between the present results for B,0.09 and those in Part II or Ref 12, since it acts so far ahead of the pitching moment centre.

The flow visualisation patterns show that in transition-free flow the design theory has succeeded in giving attached flow along the leading edges at the design incidence though there is a separation further aft. However, roughness bands have been used to fix transition and this separation has been suppressed.

The force measurements show the experimental and theoretical values of the lift coefficient at the design attachment incidence to be in good agreement.

For all the cambered wings there exists a positive pitching moment at $C_L = 0$ which ensures that the control deflection required for trimmed flight incurs less drag penalty than on the symmetric wings. The difference between the theoretical and experimental centre of pressure position at the design incidence is significant (especially for the camber surface designed for the forward centre of pressure) but this may be attributable in part to the existence of the second separation near the apex.

Above the attachment condition, the cambered wings demonstrate similar separated-flow characteristics to the symmetric wings, though vortex breakdown can be affected by camber; for example:

(i) by 'gulling' the wing, vortex breakdown can be delayed to a higher lift coefficient than on the corresponding wing with a straight trailing edge;

(ii) on the thin cambered wing vortex breakdown occurs at a lower lift coefficient than on the thin symmetric wing.

All the cambered wings achieve substantial reductions in drag compared to the corresponding symmetric wings at lift coefficients appropriate to the take-off and landing phases of flight. There is evidence of the limitations of the design

theory in so much as doubling the design attachment value of lift coefficient (from 0.1 to 0.2) does not give a much greater drag reduction; this is because the shape of the drag polar is considerably altered when compared with those of the symmetric and basic cambered wings. The thick cambered wings generate less drag than the symmetric wing for all lift coefficients greater than $0.8(C_L)_{des}$ but for the thin wings at high values of C_L, the drag relationship is complicated by the early onset of vortex breakdown on the cambered wing.

Table 1

MODEL GEOMETRY

Parameter \ Wing	A,0.09	B,0.09	C,0.09	B',0.09	B,0.09,Gull	A,0.04	B,0.04
α_{des}	0.0^{o}	5.32^{o}	10.55^{o}	7.62^{o}	5.32^{o}	0.0^{o}	5.32^{o}
$C_{L_{des}}$	0.0	0.1	0.2	0.1	0.1	0.0	0.1
$\left(\frac{x_{c.p.}}{c}\right)_{des}$	-	0.533	0.533	0.483	0.533	-	0.533
t/c	0.0902	0.0894	0.0872	0.0887	0.0894	0.0401	0.0398
T.E. shape	Straight	Straight	Straight	Straight	Gull	Straight	Straight
Wing area S (m^2)	0.1048	0.1054	0.1065	0.1058	0.1054	0.1048	0.1054
Wing chord c (m)	0.4717	0.4740	0.4791	0.4755	0.4740	0.4717	0.4740
Aspect ratio A	1.385	1.378	1.361	1.372	1.378	1.385	1.378

Planform given by $\frac{y}{s_T} = \frac{s(x)}{s_T}$

where

$$\frac{s(x)}{s_T} = 0.25\left(5(x/c) - (x/c)^5\right)$$

where $s_T = 0.1905$ m

and $c = 0.4717$ m.

Thickness distribution given by:

$$\frac{z}{c} = \frac{B(x)}{c}\left(1 - y^2/s^2(x)\right)$$

where B(x) is the centreline thickness distribution:

$$\frac{B(x)}{c} = \frac{t}{c}\frac{x}{c}\left(1 - \frac{x}{c}\right)\left[3.2471 - 7.5777\left(\frac{x}{c}\right) + 17.8647\left(\frac{x}{c}\right)^2 - 19.2073\left(\frac{x}{c}\right)^3 + 7.6754\left(\frac{x}{c}\right)^4\right].$$

t/c is the thickness/chord ratio = 0.09 or 0.04.

Table 2

SUMMARY OF RESULTS

Quantity \ Wing	A,0.09	B,0.09	C,0.09	B',0.09	B,0.09,Gull	A,0.04	B,0.04
α_{des}	0.0°	5.32°	10.55°	7.62°	5.32°	0.0°	5.32°
$C_{L_{des}}$	0.0	0.1	0.2	0.1	0.1	0.0	0.1
$\left(\frac{x_{c.p.}}{c}\right)_{des}$	-	0.533	0.533	0.483	0.533	-	0.533
			Transition fixed				
$(C_L)_{\alpha_{des}}$	0.0	0.0980	0.1965	0.106	0.106	0.0	0.0987
$\left(\frac{x_{c.p.}}{c}\right)_{\alpha_{des}}$	0.541	0.502	0.503	0.433	0.515	0.538	0.512
C_{L_m}	0.0	0.0325	0.0735	0.0310	0.0340	0.0	0.0410
C_{D_m}	0.01030	0.01175	0.01635	0.01215	0.0128	0.00855	0.01050

Table 3

WING: A,0.09. TRANSITION FIXED

V = 61 m/s

α^o	C_L	C_D^a	C_m	C_N	C_A	C_N/α	K	$\frac{x_{c.p.}}{c}$	$\frac{x_{a.c.}}{c}$
-5.03	-0.1699	0.02044	0.00301	-0.1711	0.0055	1.948	1.527	0.5576	
-3.95	-0.1290	0.01602	0.00207	-0.1298	0.0071	1.885	1.495	0.5560	
-2.86	-0.0898	0.01310	0.00100	-0.0903	0.0086	1.809	1.511	0.5511	
-1.88	-0.0583	0.01151	0.00061	-0.0586	0.0096	1.785	1.551	0.5505	
-0.85	-0.0247	0.01051	0.00022	-0.0248	0.0101	1.668	1.529	0.5488	
0.17	0.0045	0.01028	-0.00003	0.0046	0.0103	1.499		0.5465	0.5412
1.20	0.0375	0.01082	-0.00022	0.0377	0.0100	1.797	1.618	0.5459	0.5485
2.23	0.0692	0.01203	-0.00058	0.0696	0.0093	1.786	1.578	0.5483	0.5589
3.32	0.1067	0.01436	-0.00162	0.1073	0.0082	1.855	1.553	0.5551	0.5631
4.30	0.1421	0.01738	-0.00228	0.1430	0.0067	1.907	1.525	0.5560	0.5629
5.33	0.1825	0.02220	-0.00330	0.1838	0.0051	1.975	1.554	0.5580	0.5629
6.32	0.2196	0.02767	-0.00396	0.2213	0.0033	2.007	1.567	0.5579	0.5629
7.41	0.2640	0.03546	-0.00531	0.2663	0.0011	2.060	1.571	0.5599	0.5629
8.45	0.3088	0.04484	-0.00633	0.3121	-0.0010	2.117	1.575	0.5603	0.5629
9.48	0.3510	0.05492	-0.00716	0.3552	-0.0037	2.146	1.576	0.5602	0.5623
10.58	0.4008	0.06845	-0.00836	0.4065	-0.0063	2.202	1.575	0.5606	0.5621
11.57	0.4446	0.08212	-0.00931	0.4520	-0.0087	2.239	1.580	0.5606	0.5619
12.61	0.4880	0.09655	-0.00978	0.4973	-0.0123	2.260	1.575	0.5597	0.5393
13.64	0.5292	0.11252	-0.00922	0.5408	-0.0155	2.271	1.588	0.5570	0.5163
14.68	0.5733	0.13223	-0.00871	0.5881	-0.0174	2.295	1.614	0.5548	0.5396
15.77	0.6143	0.15237	-0.00901	0.6326	-0.0203	2.298	1.637	0.5542	0.5504
16.76	0.6574	0.17387	-0.00964	0.6796	-0.0231	2.323	1.647	0.5542	0.5530
17.80	0.7035	0.19910	-0.01094	0.7307	-0.0255	2.352	1.659	0.5550	0.5632
18.84	0.7504	0.22673	-0.01189	0.7834	-0.0278	2.382	1.672	0.5552	0.5579
19.89	0.8005	0.25675	-0.01312	0.8401	-0.0309	2.420	1.673	0.5556	0.5658
20.94	0.8559	0.29299	-0.01507	0.9041	-0.0322	2.474	1.679	0.5567	0.5655
21.98	0.9053	0.32752	-0.01620	0.9621	-0.0352	2.507	1.684	0.5568	0.5591
23.08	0.9533	0.36438	-0.01712	1.0199	-0.0385	2.532	1.695	0.5568	0.5567
24.02	0.9958	0.39792	-0.01537	1.0715	-0.0418	2.556	1.700	0.5543	0.5558
25.11	1.0431	0.43910	-0.01872	1.1308	-0.0450	2.580	1.714	0.5566	0.5548
26.15	1.0894	0.48297	-0.01979	1.1908	-0.0467	2.609	1.732	0.5566	0.5543

Table 3 (continued)

WING: B,0.09. TRANSITION FIXED

V = 61 m/s

α^o	C_L	C_D	C_m	C_N	C_A	C_N/α	K	$\frac{x_{c.p.}}{c}$	$\frac{x_{a.c.}}{c}$	K'
-2.92	-0.2070	0.03268	0.00946	-0.2084	0.0221	2.130		0.5854		
-1.93	-0.1658	0.02630	0.00854	-0.1666	0.0207	2.091		0.5912		
-0.84	-0.1203	0.02043	0.00743	-0.1206	0.0187	2.033		0.6016		
0.20	-0.0810	0.01660	0.00665	-0.0810	0.0169	2.003		0.6222		
1.23	-0.0440	0.01402	0.00601	-0.0437	0.0150	1.985		0.6774		
2.21	-0.0075	0.01235	0.00526	-0.0070	0.0126	1.934				
3.35	0.0338	0.01175	0.00440	0.0344	0.0098	1.850		0.4122	0.5542	
4.33	0.0678	0.01216	0.00408	0.0685	0.0070	1.707		0.4805	0.5472	
5.36	0.0986	0.01323	0.00389	0.0994	0.0040	2.005	1.305	0.5009	0.5439	1.456
6.39	0.1286	0.01501	0.00380	0.1295	0.0006	1.687	1.233	0.5106	0.5401	1.534
7.41	0.1588	0.01762	0.00381	0.1597	-0.0030	1.691	1.258	0.5161	0.5455	1.588
8.50	0.1952	0.02129	0.00350	0.1962	-0.0078	1.769	1.248	0.5222	0.5542	1.558
9.53	0.2298	0.02559	0.00287	0.2309	-0.0128	1.808	1.254	0.5275	0.5587	1.540
10.51	0.2677	0.03123	0.00202	0.2689	-0.0181	1.887	1.264	0.5325	0.5620	1.525
11.49	0.3010	0.03722	0.00140	0.3024	-0.0235	1.898	1.287	0.5354	0.5677	1.529
12.58	0.3473	0.04687	-0.00018	0.3492	-0.0299	1.982	1.313	0.5405	0.5736	1.534
13.62	0.3885	0.05705	-0.00154	0.3910	-0.0360	2.023	1.341	0.5440	0.5647	1.548
14.66	0.4315	0.06899	-0.00231	0.4349	-0.0424	2.067	1.365	0.5453	0.5639	1.557
15.70	0.4732	0.08183	-0.00310	0.4777	-0.0492	2.096	1.383	0.5465	0.5253	1.562
16.73	0.5125	0.09679	-0.00272	0.5187	-0.0549	2.113	1.426	0.5453	0.5430	1.598
17.77	0.5563	0.11512	-0.00357	0.5649	-0.0602	2.149	1.466	0.5463	0.5683	1.631
18.81	0.6033	0.13569	-0.00515	0.6148	-0.0661	2.195	1.491	0.5484	0.5771	1.647
19.86	0.6524	0.15861	-0.00707	0.6675	-0.0724	2.244	1.509	0.5506	0.5713	1.654
20.90	0.7024	0.18338	-0.00858	0.7216	-0.0793	2.294	1.519	0.5519	0.5704	1.656
21.95	0.7509	0.21028	-0.01009	0.7751	-0.0856	2.333	1.535	0.5530	0.5720	1.665
23.05	0.8080	0.24470	-0.01231	0.8393	-0.0912	2.396	1.554	0.5547	0.5646	1.677
24.09	0.8517	0.27337	-0.01341	0.8891	-0.0981	2.415	1.570	0.5551	0.5632	1.688
25.08	0.8959	0.30471	-0.01468	0.9406	-0.1038	2.443	1.588	0.5556	0.5658	1.701
26.12	0.9399	0.33845	-0.01608	0.9929	-0.1099	2.465	1.608	0.5562	0.5677	1.718

Table 3 (continued)

WING: C,0.09 TRANSITION FIXED

V = 61 m/s

α^o	C_L	C_D	C_m	C_N	C_A	C_N/α	K	$\frac{x_{c.p.}}{c}$	$\frac{x_{a.c.}}{c}$	K'
-0.99	-0.2331	0.04756	0.01486	-0.2339	0.0435	2.137		0.6035		
0.15	-0.1852	0.03869	0.01403	-0.1851	0.0392	2.102		0.6158		
1.14	-0.1445	0.03227	0.01345	-0.1439	0.0351	2.072		0.6335		
2.18	-0.1040	0.02700	0.01272	-0.1029	0.0309	2.050		0.6636		
3.27	-0.0595	0.02234	0.01188	-0.0581	0.0257	2.004		0.7445		
4.25	-0.0227	0.01952	0.01121	-0.0212	0.0211	1.980				
5.28	0.0148	0.01749	0.01054	0.0163	0.0161	1.959				
6.27	0.0514	0.01643	0.00978	0.0529	0.0107	1.922		0.3550	0.5653	
7.40	0.0930	0.01650	0.00881	0.0944	0.0044	1.857		0.4466	0.5588	
8.39	0.1271	0.01749	0.00825	0.1283	-0.0012	1.809		0.4757	0.5572	
9.42	0.1597	0.01938	0.00772	0.1607	-0.0070	1.815	1.523	0.4920	0.5530	1.773
10.50	0.1951	0.02262	0.00740	0.1959	-0.0133	-	1.384	0.5022	0.5471	1.834
11.48	0.2262	0.02636	0.00716	0.2269	-0.0192	1.873	1.342	0.5085	0.5450	1.860
12.50	0.2561	0.03081	0.00707	0.2566	-0.0254	1.766	1.338	0.5124	0.5438	1.880
13.53	0.2898	0.03627	0.00683	0.2902	-0.0326	1.801	1.323	0.5165	0.5457	1.843
14.56	0.3229	0.04244	0.00689	0.3232	-0.0401	1.811	1.318	0.5187	0.5467	1.816
15.60	0.3572	0.04953	0.00649	0.3574	-0.0483	1.826	1.315	0.5218	0.5500	1.784
16.63	0.3919	0.05768	0.00618	0.3920	-0.0569	1.842	1.319	0.5242	0.5584	1.765
17.66	0.4290	0.06749	0.00566	0.4292	-0.0658	1.875	1.329	0.5268	0.5668	1.752
18.70	0.4670	0.07836	0.00482	0.4674	-0.0755	1.905	1.335	0.5297	0.5758	1.734
19.73	0.5080	0.09173	0.00349	0.5091	-0.0852	1.951	1.349	0.5331	0.5758	1.728
20.77	0.5509	0.10720	0.00189	0.5531	-0.0951	1.999	1.365	0.5366	0.5726	1.726
21.81	0.5954	0.12491	0.00030	0.5991	-0.1053	2.048	1.383	0.5395	0.5722	1.725
22.90	0.6392	0.14514	-0.00115	0.6453	-0.1151	2.082	1.411	0.5418	0.5767	1.742
23.95	0.6856	0.16858	-0.00311	0.6950	-0.1242	2.131	1.440	0.5445	0.5828	1.759
24.93	0.7241	0.18989	-0.00510	0.7367	-0.1331	2.153	1.465	0.5469	0.5900	1.775
25.98	0.7745	0.21830	-0.00813	0.7919	-0.1430	2.211	1.483	0.5503	0.5951	1.779

Table 3 (continued)

WING: B',0.09 TRANSITION FIXED

V = 61 m/s

α^{o}	C_L	C_D	C_m	C_N	C_A	C_N/α	K	$\frac{x_{c.p.}}{c}$	$\frac{x_{a.c.}}{c}$	K'
-0.92	-0.2069	0.03174	0.01660	-0.2074	0.0284			0.6200		
0.12	-0.1636	0.02551	0.01542	-0.1635	0.0259			0.6343		
1.16	-0.1223	0.02036	0.01467	-0.1218	0.0228			0.6604		
2.20	-0.0814	0.01653	0.01364	-0.0807	0.0196			0.7090		
3.23	-0.0421	0.01388	0.01276	-0.0413	0.0162	1.909		0.8490		
4.27	-0.0036	0.01223	0.01201	-0.0027	0.0125	1.842				
5.30	0.0313	0.01172	0.01140	0.0323	0.0088	1.795	6.253	0.1867	0.5545	
6.33	0.0655	0.01218	0.01092	0.0664	0.0049	1.714	1.892	0.3757	0.5508	
7.31	0.0971	0.01319	0.01071	0.0979	0.0007	1.312	1.323	0.4307	0.5445	1.027
8.39	0.1293	0.01543	0.01071	0.1302	-0.0036	1.875	1.323	0.4577	0.5400	1.464
9.41	0.1608	0.01821	0.01061	0.1616	-0.0083	1.812	1.318	0.4744	0.5478	1.551
10.50	0.1954	0.02180	0.01004	0.1961	-0.0142	1.812	1.300	0.4888	0.5561	1.540
11.48	0.2307	0.02621	0.00943	0.2313	-0.0202	1.875	1.289	0.4992	0.5597	1.521
12.51	0.2677	0.03194	0.00861	0.2682	-0.0268	1.912	1.303	0.5079	0.5600	1.523
13.55	0.3060	0.03889	0.00799	0.3066	-0.0339	1.948	1.317	0.5139	0.5604	1.525
13.49	0.3036	0.03854	0.00843	0.3042	-0.0334	1.944	1.321	0.5123	0.5604	1.532
14.58	0.3474	0.04783	0.00723	0.3482	-0.0412	2.002	1.342	0.5192	0.5621	1.537
15.62	0.3863	0.05756	0.00635	0.3875	-0.0486	2.023	1.366	0.5236	0.5628	1.551
16.71	0.4353	0.07139	0.00510	0.4374	-0.0568	2.095	1.391	0.5283	0.5557	1.563
17.70	0.4723	0.08396	0.00491	0.4755	-0.0636	2.106	1.424	0.5297	0.5418	1.590
18.78	0.5160	0.10054	0.00426	0.5209	-0.0710	2.135	1.462	0.5318	0.5684	1.621
19.83	0.5645	0.12012	0.00244	0.5718	-0.0785	2.190	1.486	0.5357	0.5754	1.636
20.82	0.6085	0.13934	0.00087	0.6183	-0.0860	2.228	1.503	0.5386	0.5733	1.645
21.91	0.6565	0.16237	-0.00078	0.6697	-0.0944	2.264	1.522	0.5412	0.5733	1.656
22.85	0.7009	0.18513	-0.00249	0.7178	-0.1016	2.305	1.535	0.5435	0.5733	1.663
23.95	0.7545	0.21479	-0.00435	0.7767	-0.1100	2.357	1.549	0.5456	0.5733	1.670
25.05	0.8043	0.24511	-0.00627	0.8324	-0.1184	2.391	1.566	0.5475	0.5733	1.680
26.04	0.8503	0.27640	-0.00809	0.8853	-0.1249	2.427	1.588	0.5491	0.5733	1.698

Table 3 (continued)

WING: B,0.09,GULL. TRANSITION FIXED

V = 61 m/s

α^o	C_L	C_D	C_m	C_N	C_A	C_N/α	K	$\frac{x_{c.p.}}{c}$	$\frac{x_{a.c.}}{c}$	K'
-2.90	-0.1887	0.03151	0.00467	-0.1901	0.0219			0.5645		
-1.81	-0.1471	0.02545	0.00462	-0.1479	0.0208			0.5712		
-0.83	-0.1123	0.02107	0.00456	-0.1126	0.0194			0.5805		
0.21	-0.0722	0.01714	0.00391	-0.0721	0.0174			0.5943		
1.24	-0.0338	0.01451	0.00366	-0.0334	0.0152	1.972		0.6496		
2.27	0.0044	0.01294	0.00318	0.0049	0.0128	1.918			0.5484	
3.31	0.0409	0.01264	0.00293	0.0416	0.0103	1.864	6.047	0.4696	0.5463	
4.34	0.0758	0.01320	0.00269	0.0765	0.0074	1.783	2.190	0.5049	0.5449	
5.32	0.1060	0.01437	0.00245	0.1068	0.0045	-	1.569	0.5171	0.5437	
6.40	0.1394	0.01652	0.00248	0.1403	0.0009	1.767	1.388	0.5223	0.5432	1.450
7.43	0.1731	0.01931	0.00232	0.1742	-0.0032	1.825	1.303	0.5267	0.5446	1.457
8.46	0.2058	0.02269	0.00210	0.2069	-0.0078	1.823	1.267	0.5299	0.5484	1.451
9.49	0.2411	0.02701	0.00166	0.2422	-0.0131	1.858	1.246	0.5331	0.5577	1.435
10.47	0.2784	0.03245	0.00077	0.2796	-0.0187	1.920	1.238	0.5373	0.5616	1.425
11.56	0.3184	0.03947	0.00001	0.3199	-0.0251	1.955	1.246	0.5400	0.5600	1.428
12.59	0.3593	0.04815	-0.00084	0.3611	-0.0313	2.003	1.270	0.5423	0.5624	1.447
13.63	0.4047	0.05943	-0.00189	0.4073	-0.0376	2.071	1.299	0.5446	0.5639	1.470
14.68	0.4529	0.07283	-0.00319	0.4566	-0.0443	2.140	1.320	0.5470	0.5655	1.482
15.72	0.5001	0.08793	-0.00450	0.5052	-0.0509	2.194	1.344	0.5489	0.5635	1.498
15.77	0.5031	0.08851	-0.00453	0.5082	-0.0516	2.200	1.338	0.5489	0.5635	1.490
16.76	0.5459	0.10362	-0.00542	0.5526	-0.0582	2.232	1.356	0.5498	0.5590	1.501
17.81	0.5963	0.12325	-0.00648	0.6054	-0.0650	2.286	1.376	0.5507	0.5609	1.513
18.85	0.6469	0.14524	-0.00767	0.6592	-0.0716	2.338	1.396	0.5516	0.5661	1.527
19.90	0.6997	0.17043	-0.00923	0.7160	-0.0779	2.393	1.416	0.5529	0.5661	1.541
20.90	0.7496	0.19554	-0.01061	0.7700	-0.0847	2.438	1.428	0.5538	0.5633	1.546
21.99	0.8010	0.22612	-0.01187	0.8274	-0.0903	2.476	1.457	0.5543	0.5602	1.570
23.04	0.8533	0.25991	-0.01302	0.8870	-0.0948	2.522	1.485	0.5547	0.5590	1.594
24.13	0.8974	0.29090	-0.01398	0.9379	-0.1014	2.531	1.509	0.5549	0.5593	1.616
25.12	0.9417	0.32408	-0.01505	0.9902	-0.1064	2.556	1.533	0.5552	0.5640	1.636
26.17	0.9902	0.36289	-0.01683	1.0487	-0.1109	2.588	1.558	0.5560	0.5687	1.658
27.21	1.0340	0.40042	-0.01831	1.1026	-0.1166	2.606	1.580	0.5566	0.5708	1.679

Table 3 (continued)

WING: A,0.04. TRANSITION FIXED

V = 61 m/s

α^o	C_L	C_D	C_m	C_N	C_A	C_N/α	K	$\frac{x_{c.p.}}{c}$	$\frac{x_{a.c.}}{c}$
-4.82	-0.1725	0.02023	0.00145	-0.1735	0.0056	2.061	1.708	0.5484	
-3.74	-0.1291	0.01494	0.00118	-0.1298	0.0065	1.990	1.669	0.5491	
-2.75	-0.0916	0.01165	0.00075	-0.0921	0.0072	1.917	1.606	0.5481	
-1.67	-0.0521	0.00959	0.00023	-0.0524	0.0081	1.801	1.669	0.5444	
-0.64	-0.0208	0.00868	-0.00006	-0.0209	0.0084	1.876	1.261	0.5370	
0.34	0.0098	0.00852	-0.00012	0.0099	0.0085	1.674		0.5517	
1.37	0.0436	0.00945	-0.00012	0.0438	0.0084	1.832	2.053	0.5427	0.5457
2.45	0.0816	0.01111	-0.00059	0.0820	0.0076	1.916	1.672	0.5472	0.5555
3.44	0.1191	0.01417	-0.00109	0.1198	0.0070	1.997	1.722	0.5491	0.5537
4.47	0.1585	0.01852	-0.00151	0.1594	0.0061	2.043	1.726	0.5495	0.5499
5.46	0.1984	0.02423	-0.00194	0.1998	0.0052	2.097	1.732	0.5497	0.5489
6.55	0.2454	0.03232	-0.00237	0.2474	0.0041	2.165	1.718	0.5496	0.5477
7.59	0.2886	0.04139	-0.00270	0.2915	0.0029	2.201	1.715	0.5493	0.5470
8.68	0.3393	0.05364	-0.00295	0.3435	0.0018	2.266	1.704	0.5486	0.5428
9.68	0.3857	0.06660	-0.00302	0.3914	0.0008	2.318	1.697	0.5477	0.5406
10.72	0.4330	0.08120	-0.00314	0.4405	-0.0007	2.355	1.686	0.5471	0.5410
11.76	0.4815	0.09797	-0.00328	0.4913	-0.0022	2.393	1.678	0.5467	0.5410
12.81	0.5329	0.11723	-0.00317	0.5456	-0.0038	2.441	1.665	0.5458	0.5422
13.80	0.5837	0.13815	-0.00349	0.5999	-0.0051	2.490	1.654	0.5458	0.5469
14.91	0.6437	0.16516	-0.00376	0.6645	-0.0060	2.554	1.644	0.5457	0.5389
16.01	0.6958	0.19095	-0.00320	0.7215	-0.0083	2.583	1.639	0.5444	0.5272
17.00	0.7479	0.21890	-0.00253	0.7793	-0.0094	2.626	1.636	0.5432	0.5300
18.05	0.8036	0.25082	-0.00198	0.8418	-0.0106	2.672	1.632	0.5423	0.5326
19.15	0.8609	0.28571	-0.00136	0.9070	-0.0126	2.713	1.627	0.5415	0.5290
20.15	0.9137	0.32097	-0.00058	0.9683	-0.0135	2.753	1.628	0.5406	0.5213
21.19	0.9497	0.35102	0.00220	1.0124	-0.0159	2.738	1.652	0.5378	-
22.22	0.9866	0.38528	0.00497	1.0590	-0.0164	2.731	1.684	0.5353	0.5308
23.32	1.0376	0.42690	0.00487	1.1218	-0.0186	2.757	1.690	0.5357	0.5445
24.36	1.0869	0.47131	0.00452	1.1845	-0.0190	2.786	1.704	0.5362	0.5400
25.35	1.1278	0.51098	0.00514	1.2380	-0.0211	2.798	1.718	0.5358	0.5380
26.44	1.1762	0.56011	0.00503	1.3025	-0.0222	2.822	1.734	0.5361	0.5430

Table 3 (concluded)

WING: B, 0.04. TRANSITION FIXED

V = 61 m/s

α^o	C_L	C_D	C_m	C_N	C_A	C_N/α	K	$\frac{x_{c.p.}}{c}$	$\frac{x_{a.c.}}{c}$	K'
-2.87	-0.2123	0.03419	0.00593	-0.2138	0.0235			0.5677		
-1.88	-0.1717	0.02742	0.00581	-0.1725	0.0218			0.5737		
-0.85	-0.1308	0.02142	0.00549	-0.1311	0.0195			0.5818		
0.24	-0.0836	0.01626	0.00476	-0.0835	0.0166			0.5970		
1.23	-0.0431	0.01318	0.00415	-0.0428	0.0141			0.6371		
2.27	-0.0049	0.01119	0.00374	-0.0044	0.0114					
3.30	0.0315	0.01033	0.00327	0.0320	0.0085			0.4378		
4.33	0.0665	0.01059	0.00297	0.0671	0.0055			0.4957	0.5476	
5.41	0.1019	0.01169	0.00275	0.1026	0.0020	1.655	1.308	0.5132	0.5397	1.389
6.39	0.1320	0.01361	0.00293	0.1326	-0.0012	1.746	1.258	0.5179	0.5382	1.625
7.42	0.1657	0.01665	0.00289	0.1664	-0.0049	1.812	1.279	0.5227	0.5423	1.712
8.45	0.2002	0.02034	0.00277	0.2010	-0.0093	1.849	1.274	0.5262	0.5456	1.681
9.48	0.2381	0.02532	0.00245	0.2390	-0.0143	1.914	1.281	0.5297	0.5511	1.652
10.52	0.2778	0.03209	0.00194	0.2790	-0.0192	1.972	1.321	0.5330	0.5534	1.667
11.56	0.3223	0.04128	0.00142	0.3241	-0.0242	2.058	1.364	0.5356	0.5531	1.684
12.65	0.3719	0.05338	0.00081	0.3746	-0.0294	2.146	1.404	0.5378	0.5490	1.695
13.69	0.4159	0.06599	0.00049	0.4197	-0.0343	2.188	1.438	0.5388	0.5418	1.709
14.68	0.4589	0.07938	0.00060	0.4640	-0.0395	2.228	1.457	0.5387	0.5388	1.707
15.78	0.5076	0.09679	0.00046	0.5148	-0.0449	2.272	1.483	0.5391	0.5323	1.716
16.77	0.5512	0.11436	0.00118	0.5608	-0.0495	2.306	1.508	0.5379	0.5329	1.727
17.86	0.6044	0.13857	0.00122	0.6178	-0.0535	2.366	1.542	0.5380	0.5442	1.747
18.86	0.6502	0.16055	0.00077	0.6672	-0.0582	2.400	1.557	0.5388	0.5497	1.750
19.90	0.7029	0.18781	0.00023	0.7248	-0.0627	2.455	1.571	0.5397	0.5504	1.752
20.95	0.7498	0.21402	-0.00006	0.7768	-0.0682	2.481	1.583	0.5401	0.5533	1.754
21.99	0.7977	0.24278	-0.00109	0.8306	-0.0736	2.511	1.594	0.5413	0.5434	1.756
23.10	0.8606	0.28411	-0.00084	0.9031	-0.0763	2.588	1.611	0.5409	0.5380	1.763
24.09	0.9077	0.31755	-0.00093	0.9582	-0.0806	2.620	1.624	0.5410	0.5439	1.770
25.13	0.9535	0.35283	-0.00127	1.0131	-0.0855	2.641	1.640	0.5413	0.5450	1.780
26.18	1.0068	0.39678	-0.00143	1.0785	-0.0881	2.688	1.659	0.5413	0.5455	1.793

LIST OF SYMBOLS

a	linear normal force parameter
A	aspect ratio $= \frac{s_T^2}{S}$
c	model centreline chord
C_A	axial force coefficient
C_D	drag coefficient
C_L	lift coefficient
C_m	pitching moment coefficient taken about 0.54c from wing apex
C_N	normal force coefficient
C_{D_0}	minimum drag of symmetric wing
C_{D_m}	minimum drag of cambered wing
C_{L_m}	value of C_L when $C_D = C_{D_m}$
$C_{N_{n.l.}}$	non-linear component of normal force
K	induced drag factor $= \pi A \left(C_D - C_{D_0}\right) / C_L^2$
K'	induced drag factor $= \pi A \left(C_D - C_{D_m}\right) / \left(C_L - C_{L_m}\right)^2$
R	Reynolds number
s	local semi-span
$s(x)$	equation of leading edge
s_T	trailing edge semispan
S	wing area
t/c	thickness/centreline chord ratio of wing
x	chordwise distance from apex
$\frac{x_{c.p.}}{c}$	position of the centre of pressure as a fraction of chord
$\frac{x_{a.c.}}{c}$	position of the aerodynamic centre as a fraction of chord
y	spanwise distance from centreline (positive to starboard)
z	third axis forming right handed system of axes with x and y
α	centreline angle of incidence

Subscripts

des	the theoretical value of the quantity
α_{des}	the value of the quantity at the theoretical design incidence

REFERENCES

No.	Author	Title, etc
1	D.A. Kirby A.G. Hepworth	Low-speed wind-tunnel tests on some slender airbus configurations. RAE Technical Report 71216 (ARC R & M No.3747) (1971)
2	J.E. Barsby	Flow past conically cambered slender delta wings with leading-edge separation. ARC R & M No.3748 (1972)
3	P.J. Butterworth	Low-speed wind-tunnel tests on a family of cambered wings of mild gothic planform of aspect ratio 1.4. ARC CP No.1163 (1970)
4	Patricia J. Davies	The design of a series of warped slender wings for subsonic speeds. ARC CP No.1263 (1971)
5	D.A. Kirby	An experimental investigation of the effect of planform shape on the subsonic longitudinal stability characteristics of slender wings. ARC R & M No.3568 (1967)
6	D.A. Kirby D.L.I. Kirkpatrick	An experimental investigation of the effect of thickness on the subsonic longitudinal stability characteristics of delta wings of 70° sweep-back. ARC R & M No.3673 (1969)
7	F.G. Leppington	Curvature effects in the diffraction of short waves into a shadow. ARC CP No.1193 (1970)
8	W.J.G. Trebble D.A. Kirby	Reduction of the rolling moments of slender wing models by the application of full- and part-span anhedral. RAE Technical Report 67300 - ARC 30084 (1967)
9	H.C. Garner (Editor)	Subsonic wind tunnel wall corrections. AGARDograph 109 (1966)

REFERENCES (concluded)

No.	Author	Title, etc
10	D.J. Kettle	Notes on a Mercury programme for estimating corrections due to wire support rigs in low-speed tunnels. RAE unpublished material (1964)
11	D.L.I. Kirkpatrick	A study of the leading-edge vortices above slender wings. RAE unpublished material (1970)
12	P.J. Butterworth D.G. Dobney	RAE Technical Report - to be issued
13	D.L.I. Kirkpatrick D.A. Kirby	An experimental investigation of the subsonic longitudinal characteristics of five slender-wing models with gothic planforms. ARC R & M No.3720 (1971)
14	D.L.I. Kirkpatrick	Investigation of the normal force characteristics of slender delta wings with various rhombic cross-sections in subsonic flow. ARC CP No.922 (1965)

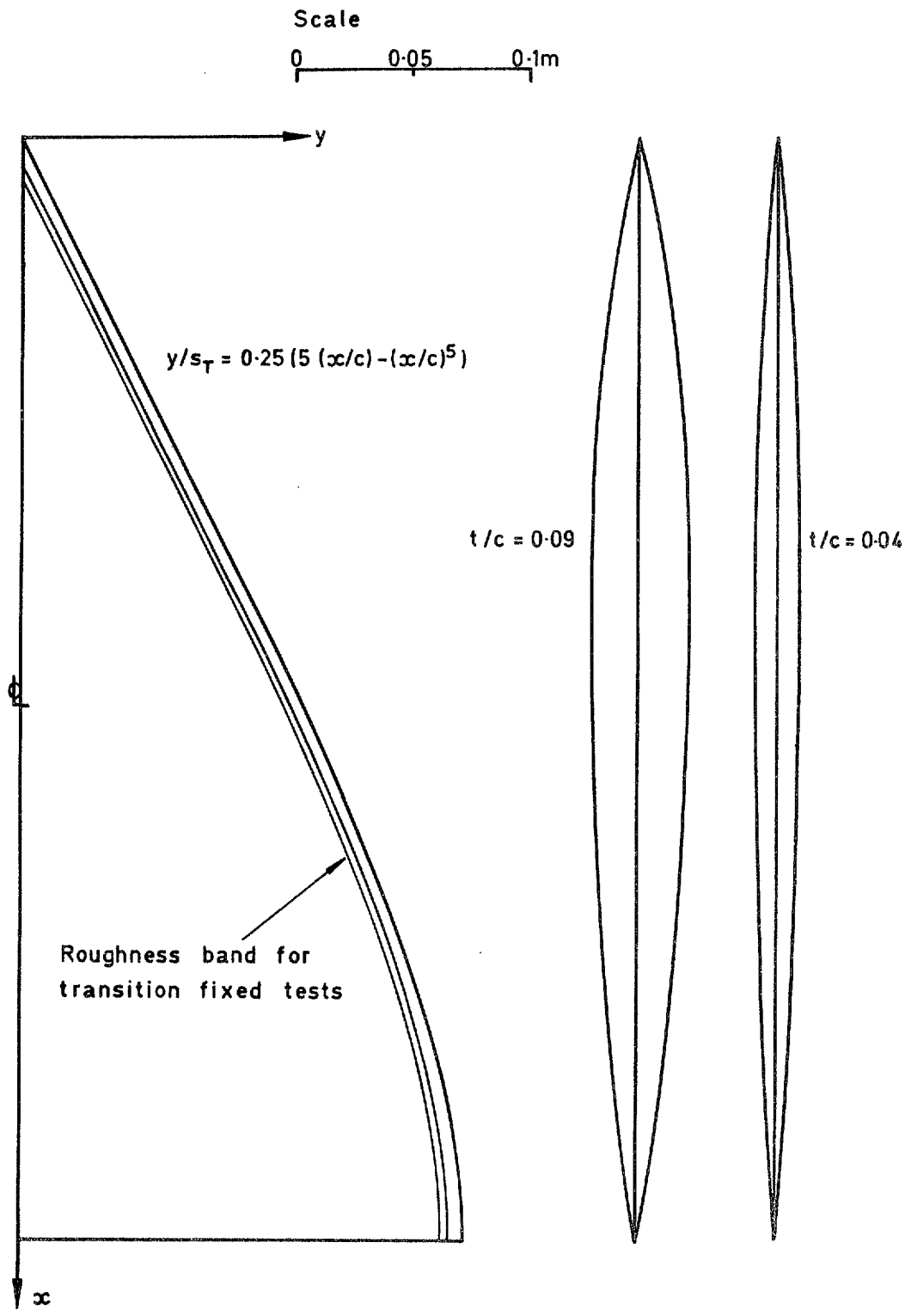

Fig 1 Planform and centreline thickness distributions

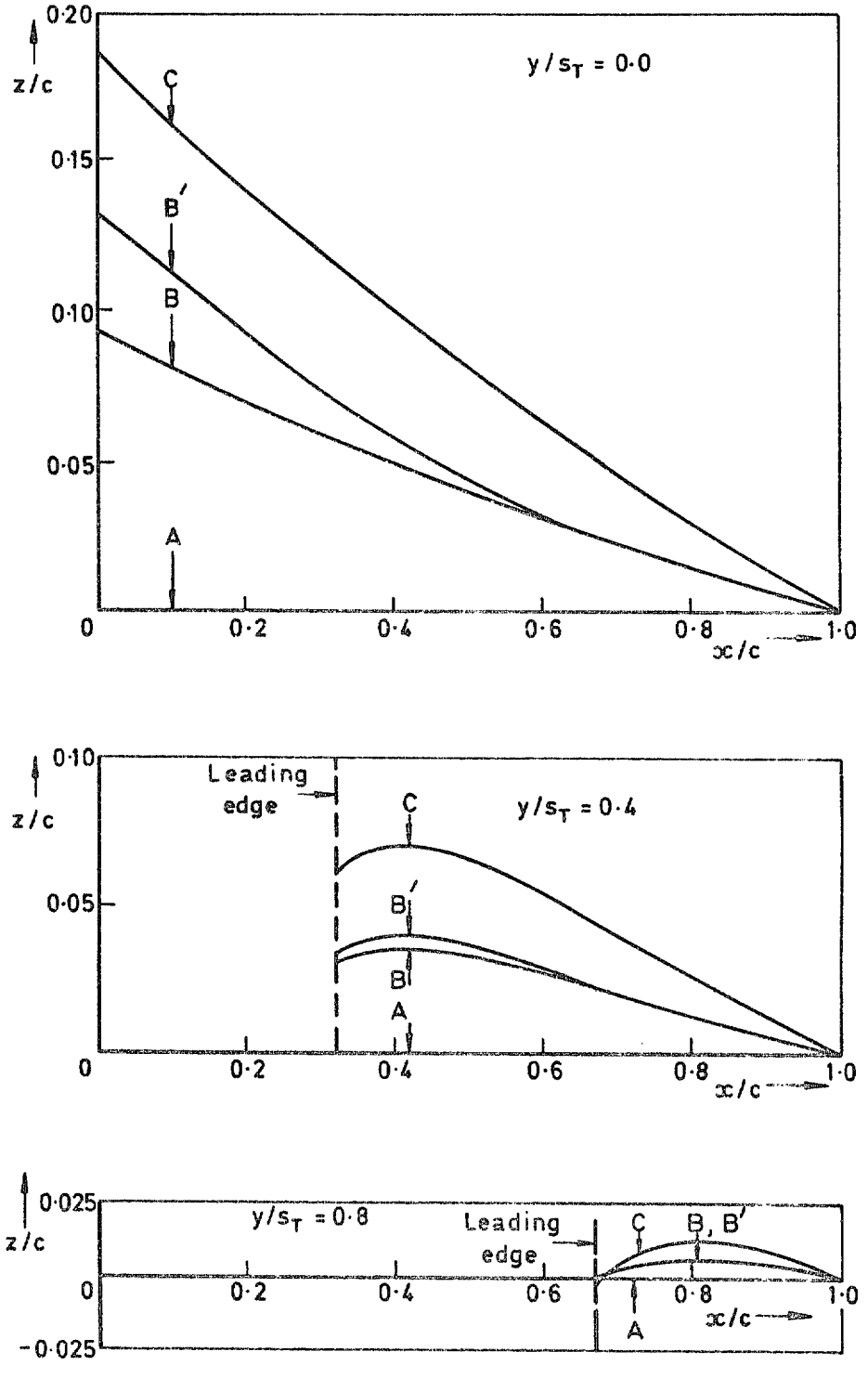

Fig 2 Some chordwise sections of the camber surfaces

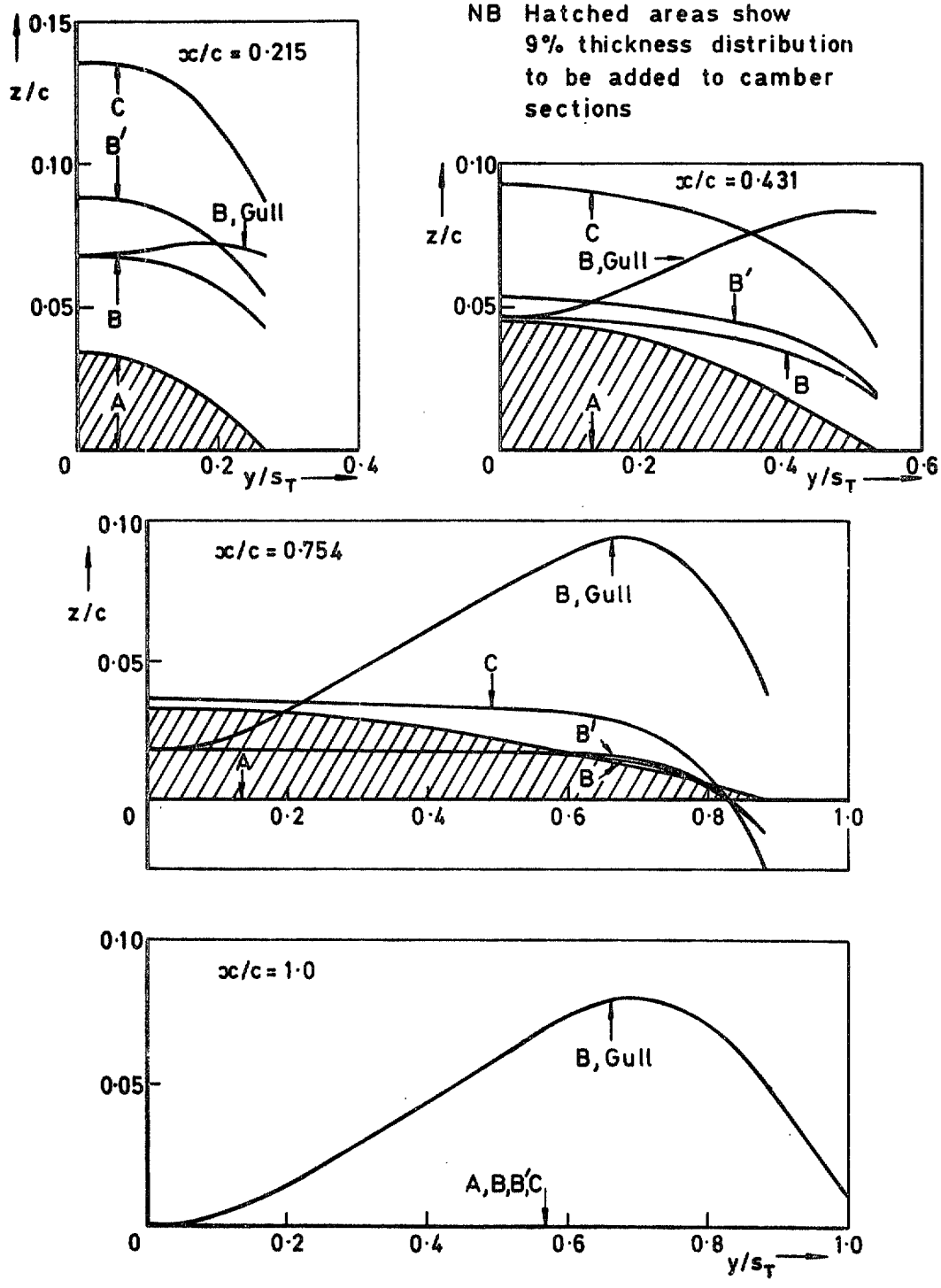

Fig 3 Some spanwise sections of the camber surfaces and corresponding 9% thickness distribution

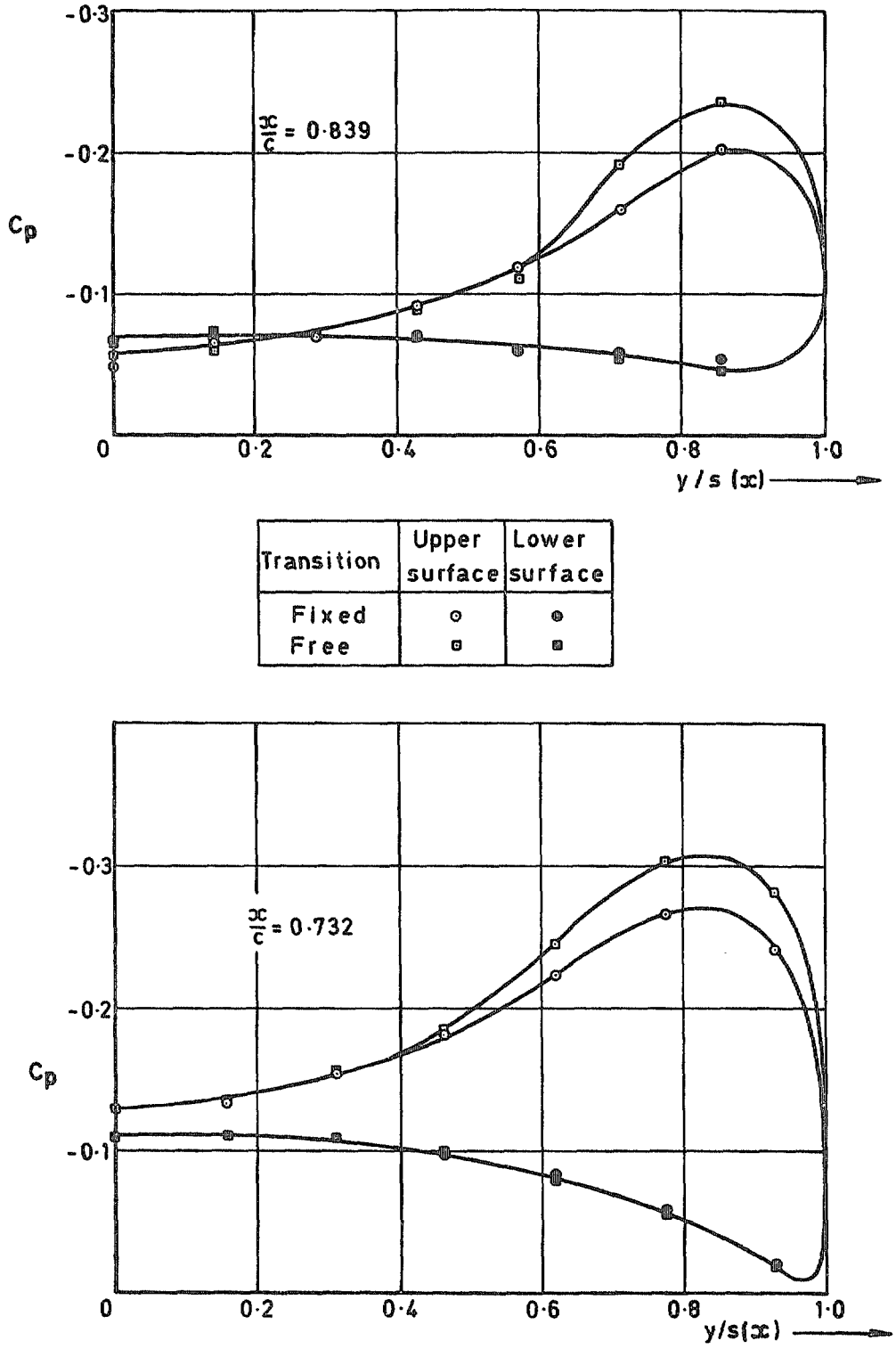

Fig 4 Spanwise pressure distributions on wing B,0.09 (transition fixed and free) V = 55 m/s

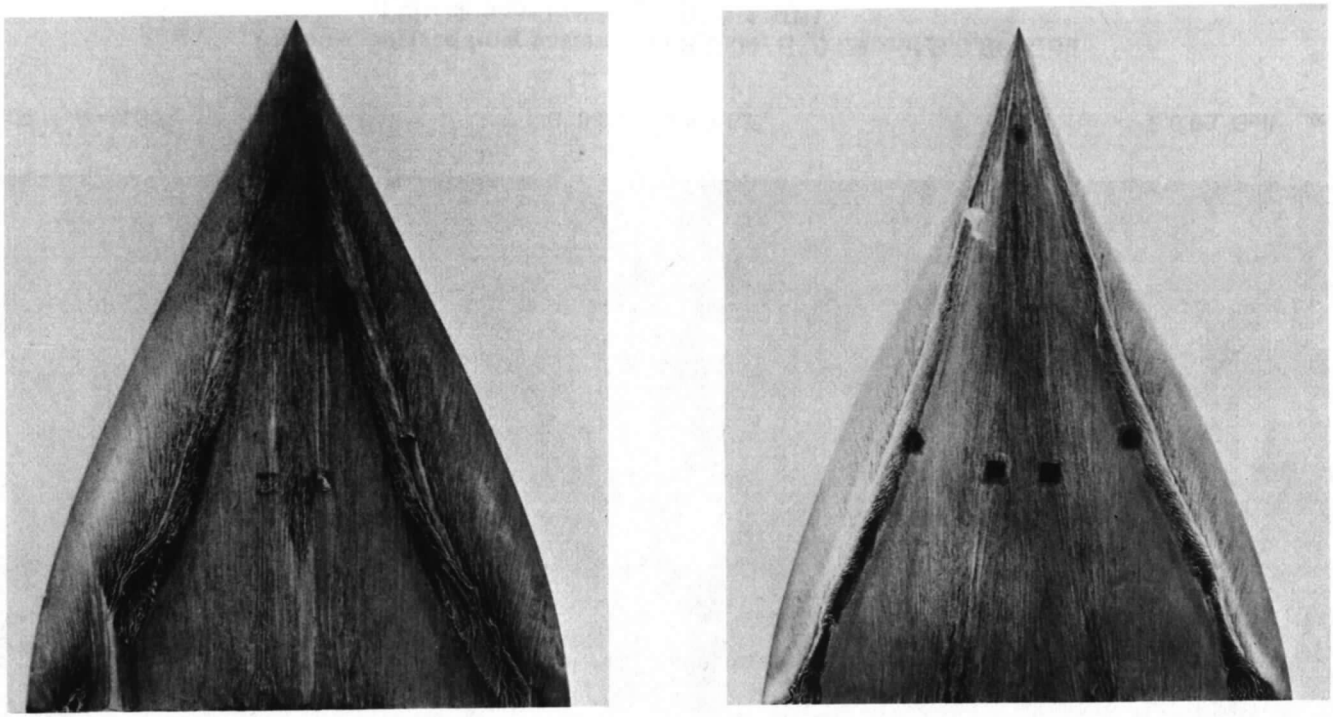

B,0.09 $\alpha = 5.32^{\circ}$ C,0.09 $\alpha = 10.55^{\circ}$

Fig 5a Surface flow patterns on B,0.09 and C,0.09 at attachment incidence ($R = 1.10^6$)

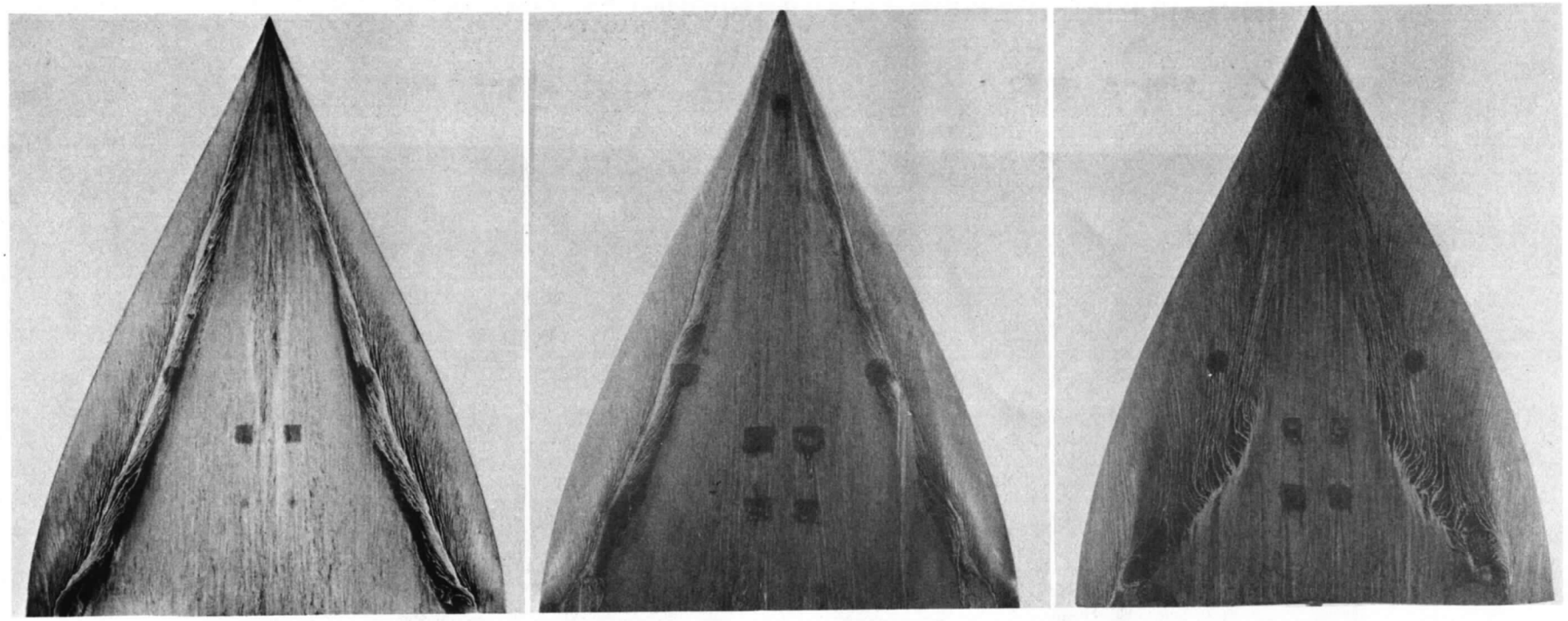

B,0.04 $\alpha = 5.32^\circ$ B′,0.09 $\alpha = 7.62^\circ$ B,0.09, Gull $\alpha = 5.32^\circ$

Fig 5b Surface flow patterns on B,0.04; B′,0.09 and B,0.09, Gull at attachment incidence ($R = 1.10^6$)

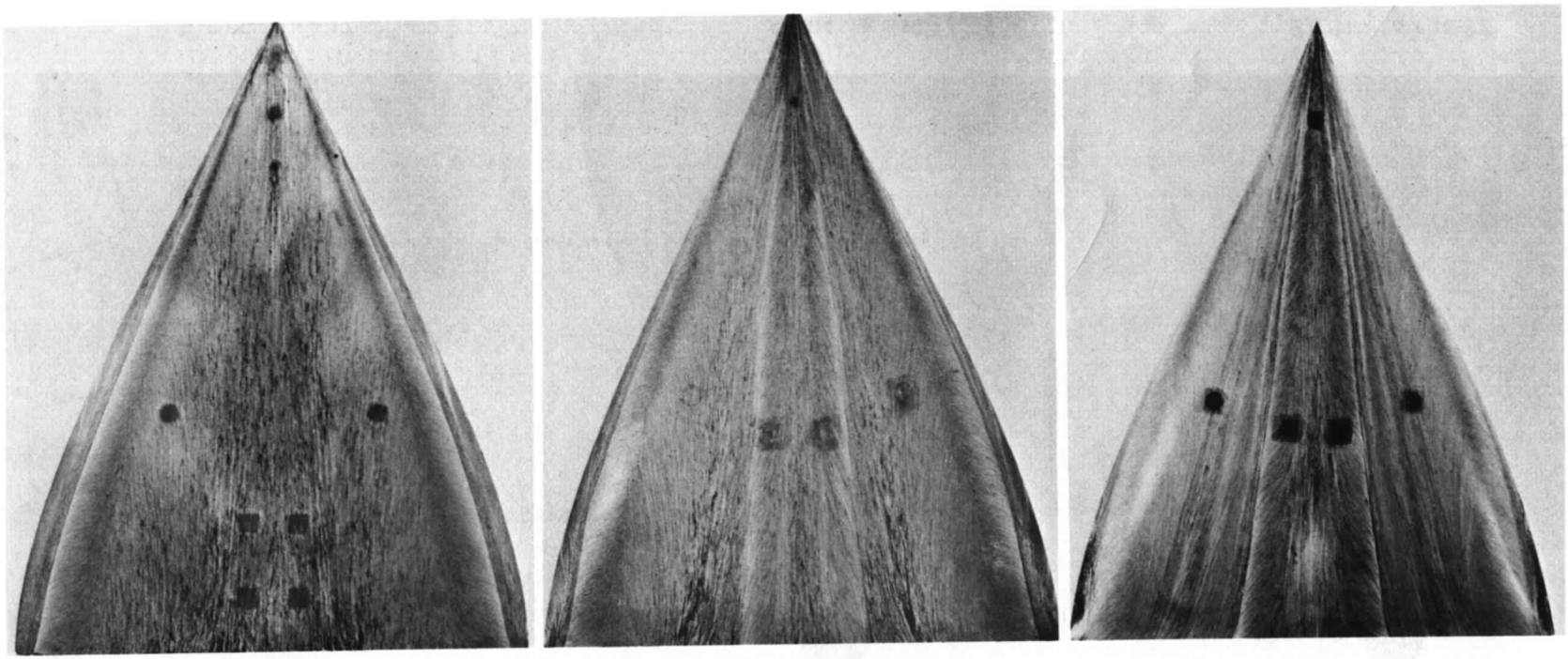

A, 0.09 $\alpha = 10^{\circ}$ B,0.09 $\alpha = 15.32^{\circ}$ C,0.09 $\alpha = 20.55^{\circ}$

Fig 6a Surface flow patterns on A,0.09; B,0.09 and C,0.09. 10° above attachment incidence ($R = 1.10^6$)

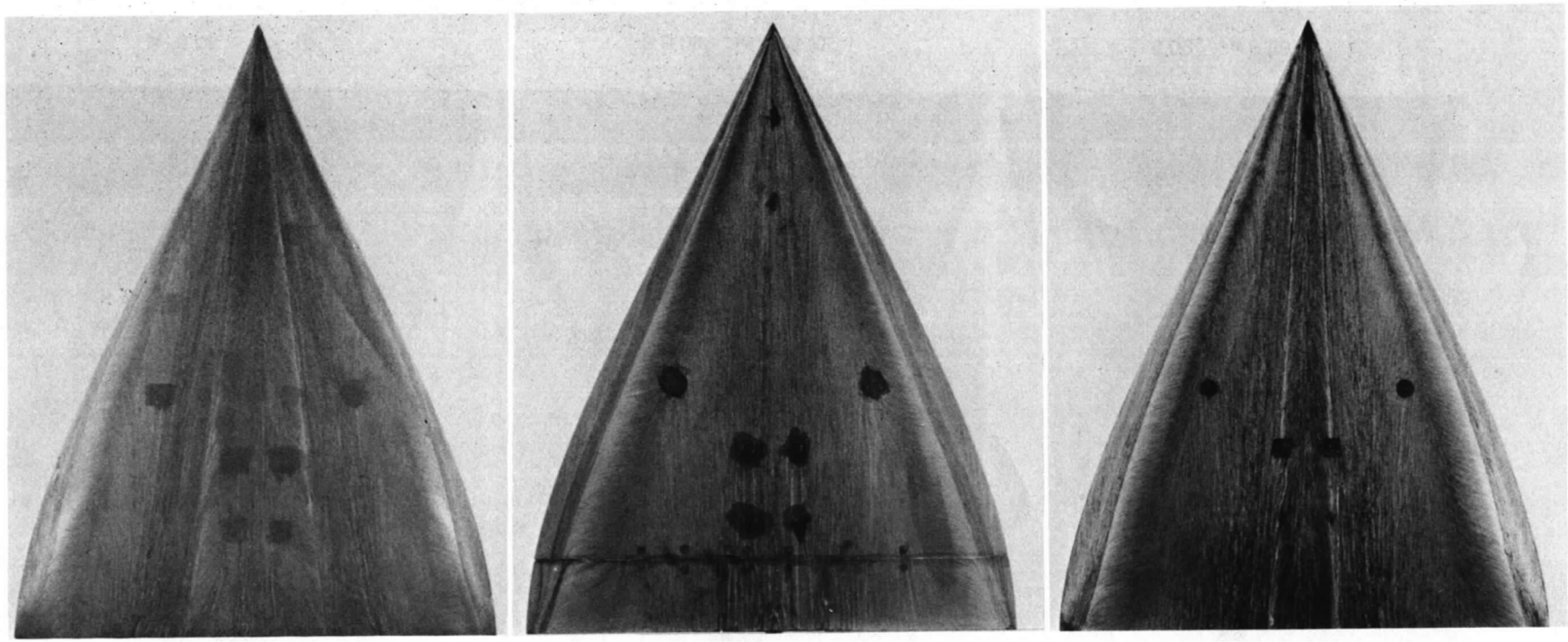

B′,0.09 $\alpha = 17.62^\circ$ A,0.04 $\alpha = 10^\circ$ B,0.04 $\alpha = 15.32^\circ$

Fig 6b Surface flow patterns on B′,0.09; A,0.04 and B,0.04. 10° above attachment incidence ($R = 1.10^6$)

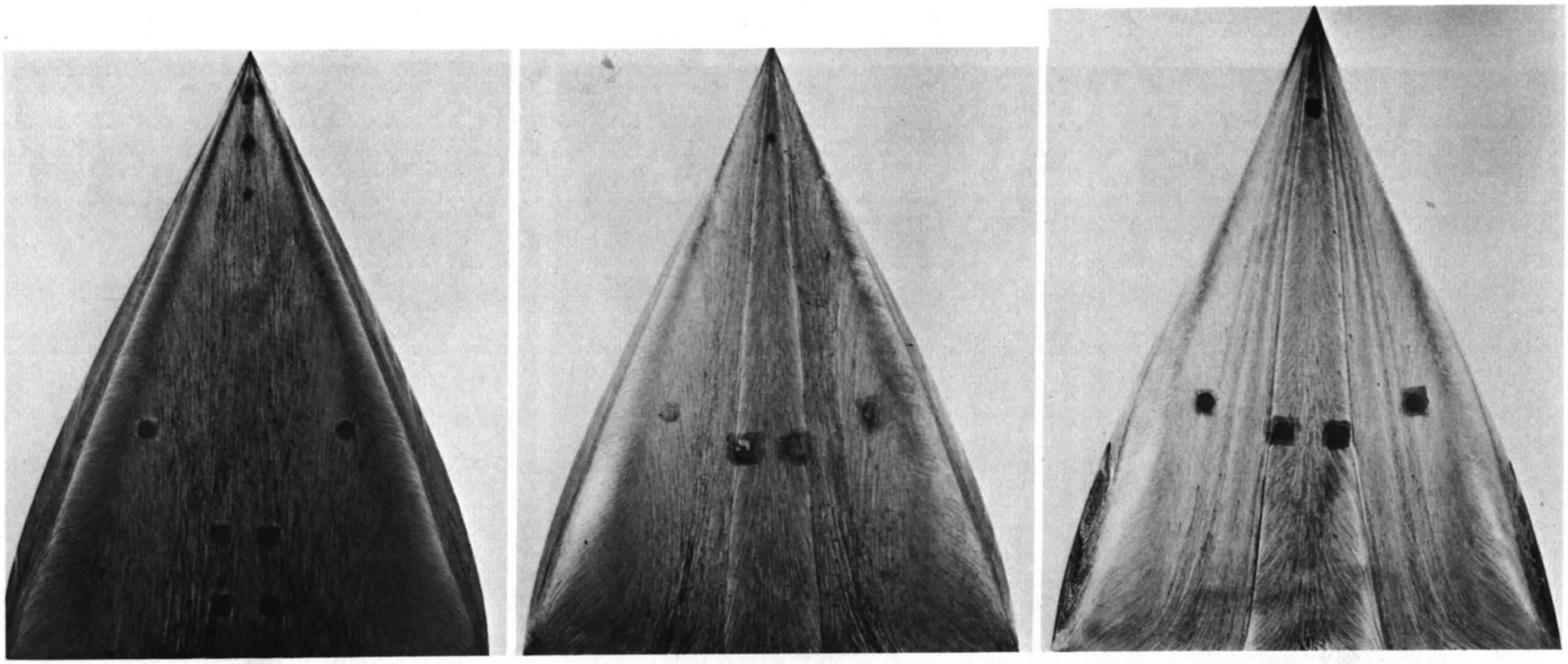

A,0.09 $\alpha = 15^{\circ}$

B,0.09 $\alpha = 20.32^{\circ}$

C,0.09 $\alpha = 25.55^{\circ}$

Fig 7a Surface flow patterns on A,0.09; B,0.09 and C,0.09. 15° above attachment incidence (R = 1.10^6)

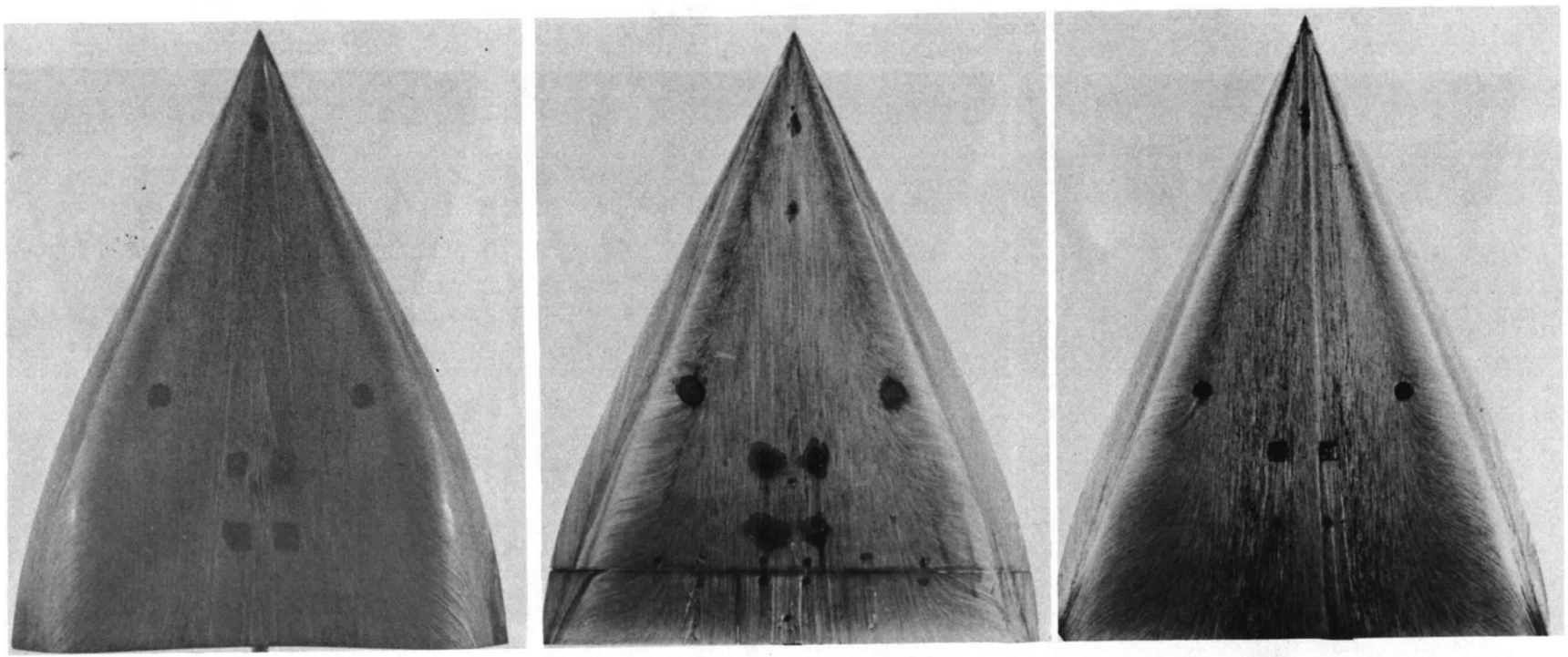

B,0.09, Gull $\alpha = 20.32^\circ$ A,0.04 $\alpha = 15^\circ$ B,0.04 $\alpha = 20.32^\circ$

Fig 7b Surface flow patterns on B,0.09, Gull; A,0.04 and B,0.04. 15° above attachment incidence ($R = 1.10^6$)

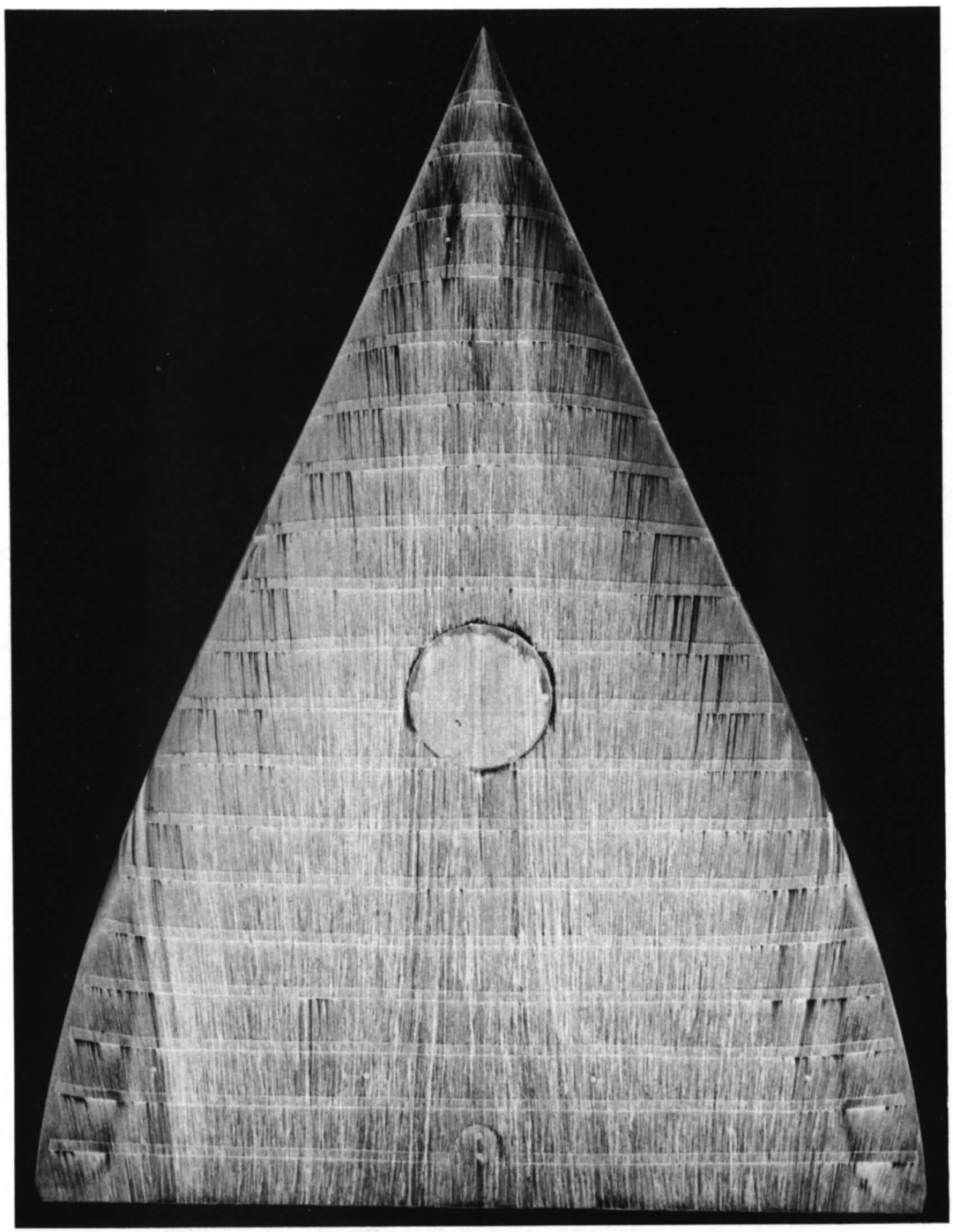

Fig 8 Surface flow pattern on larger version of B,0.09, $\alpha = 5.32°$. $R = 4.10^6$

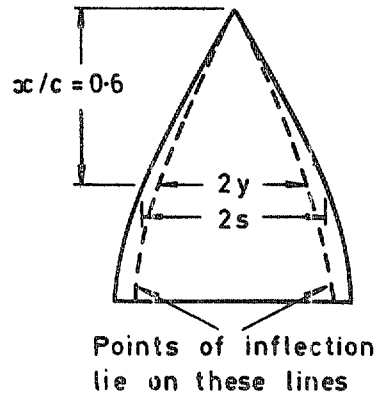

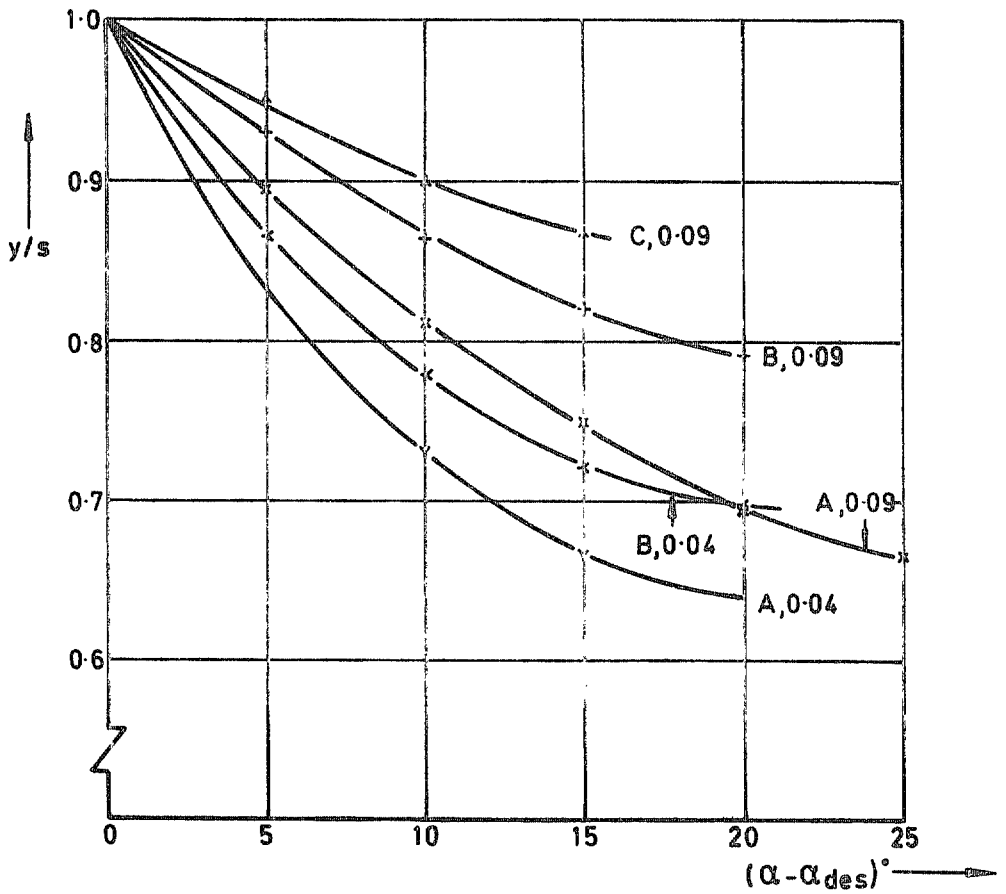

Fig 9 Spanwise position of point of inflection at x/c = 0.6

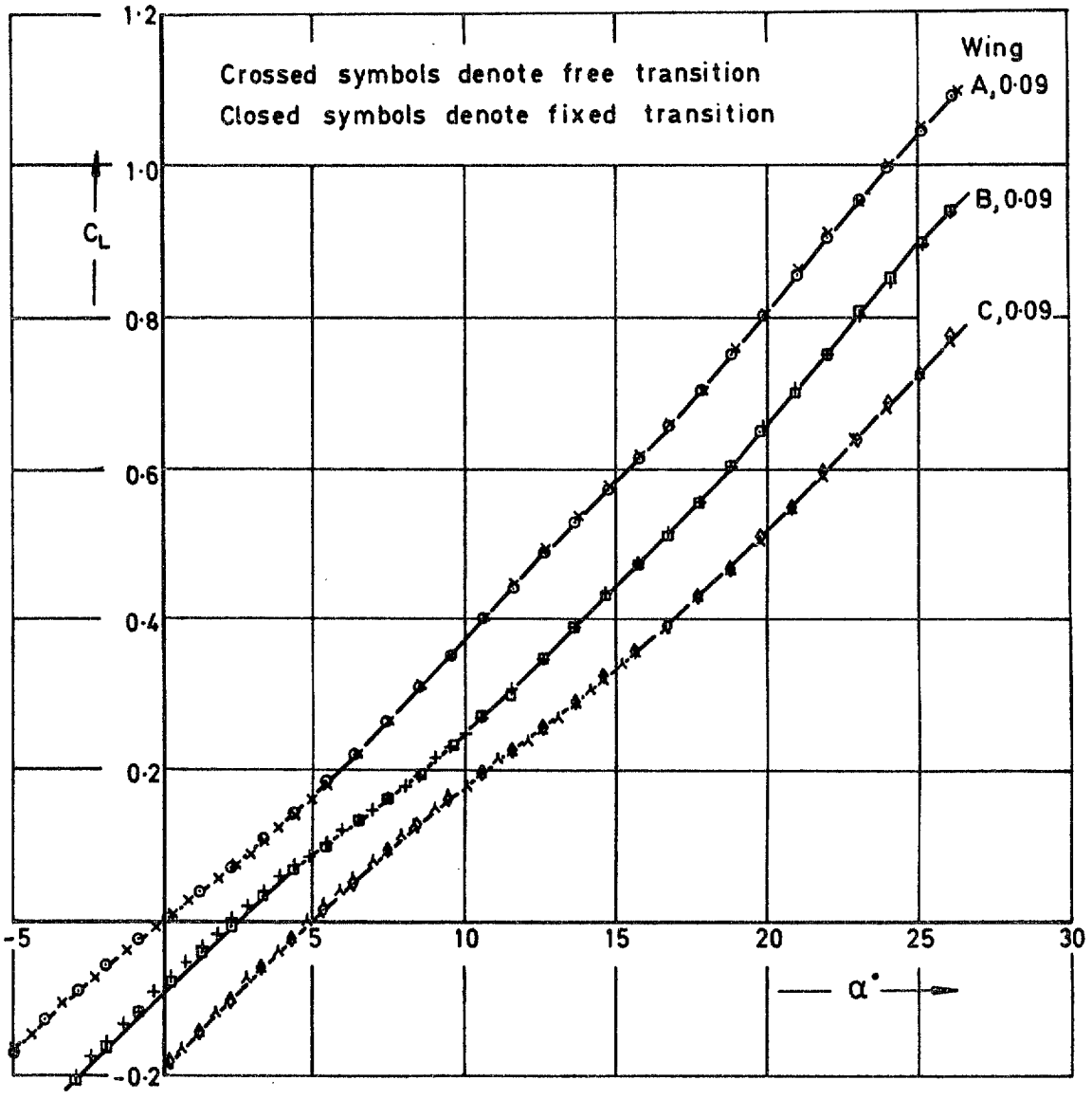

Fig 10a Effect of fixing transition on the lift characteristics
t/c = 0.09

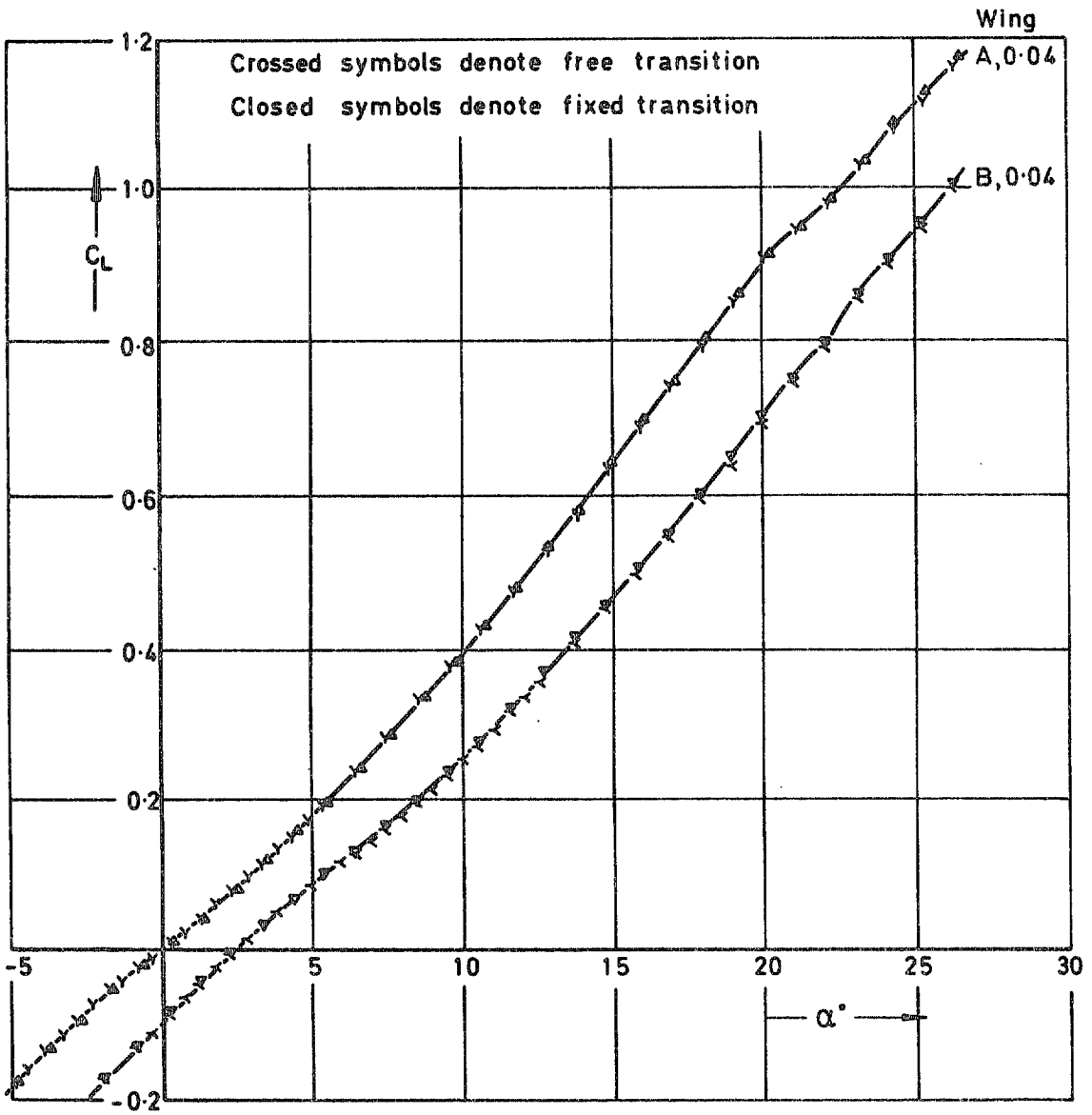

Fig 10b Effect of fixing transition on the lift characteristics
t/c = 0.04

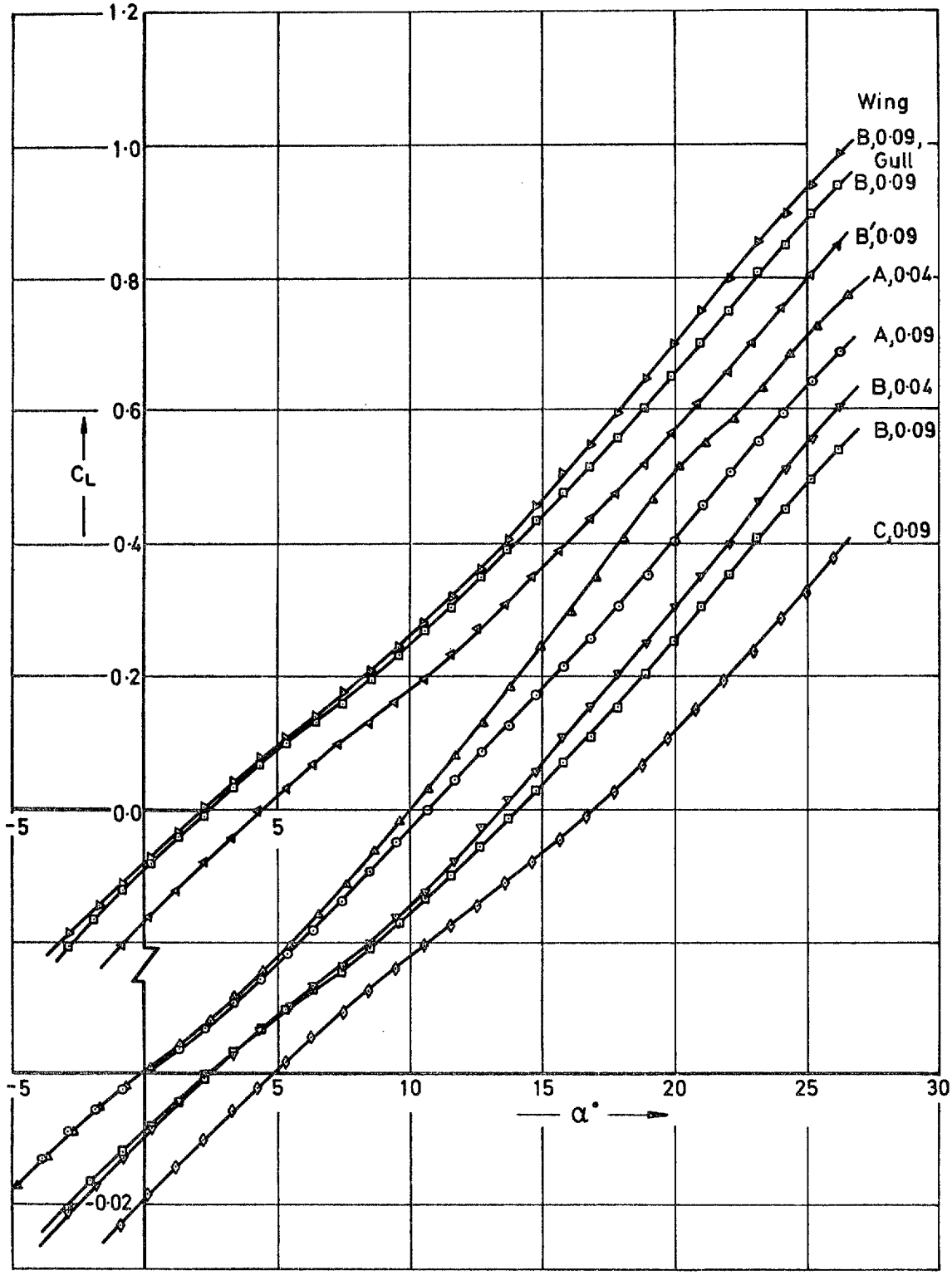

Fig 11 The lift characteristics of the seven wings (transition fixed)

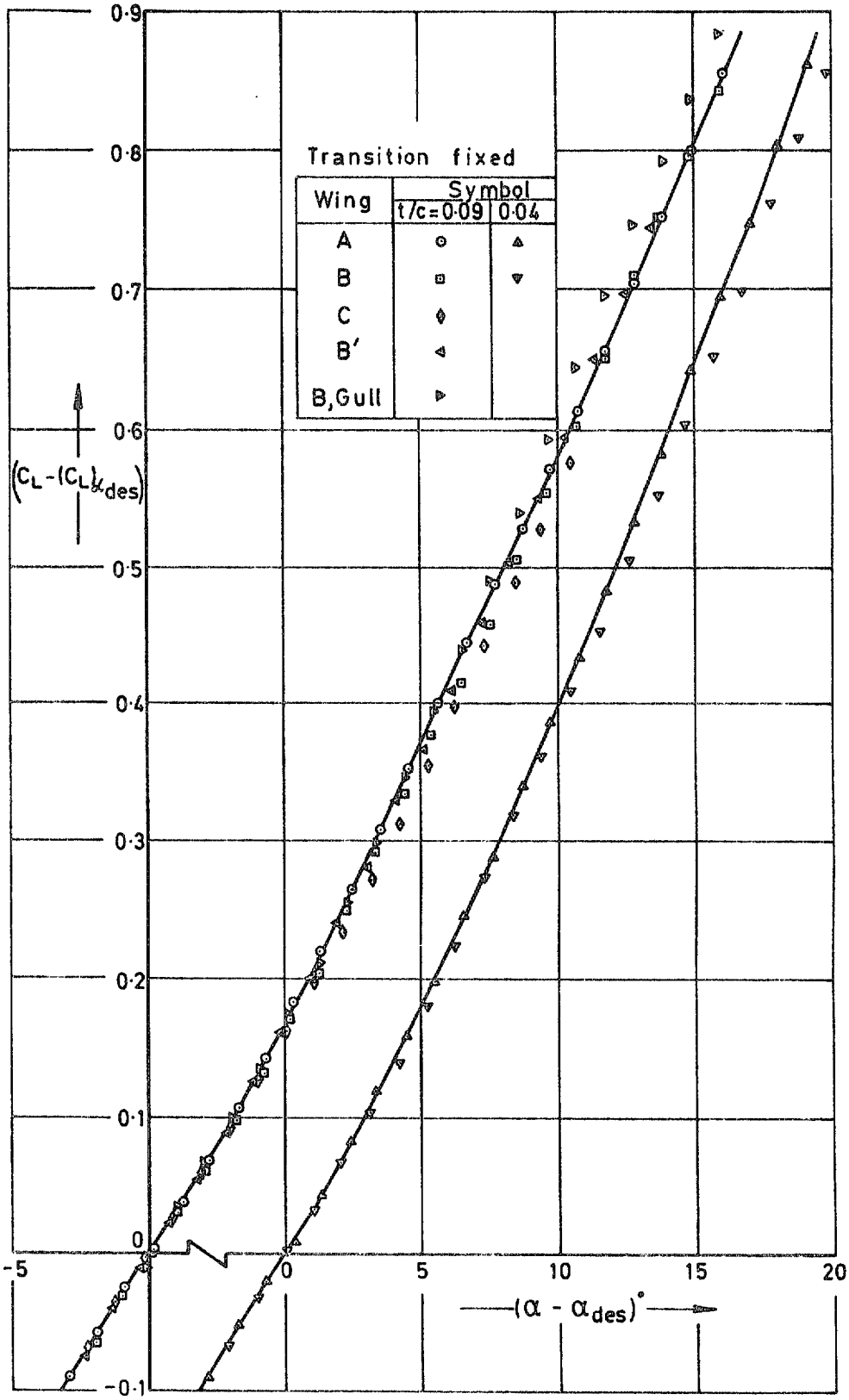

Fig 12 Collapse of lift curves

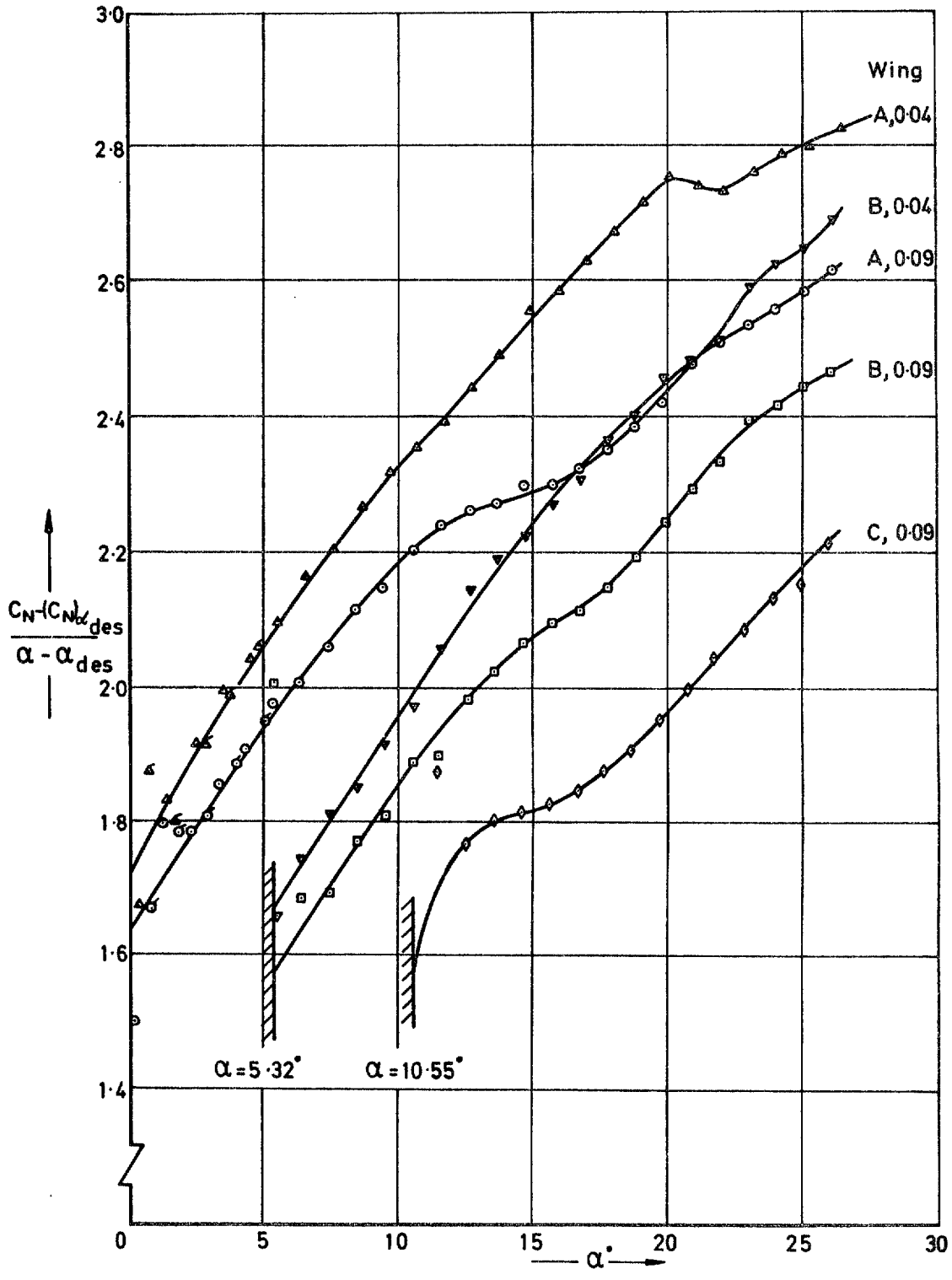

Fig 13 C_N/α vs α (transition fixed)

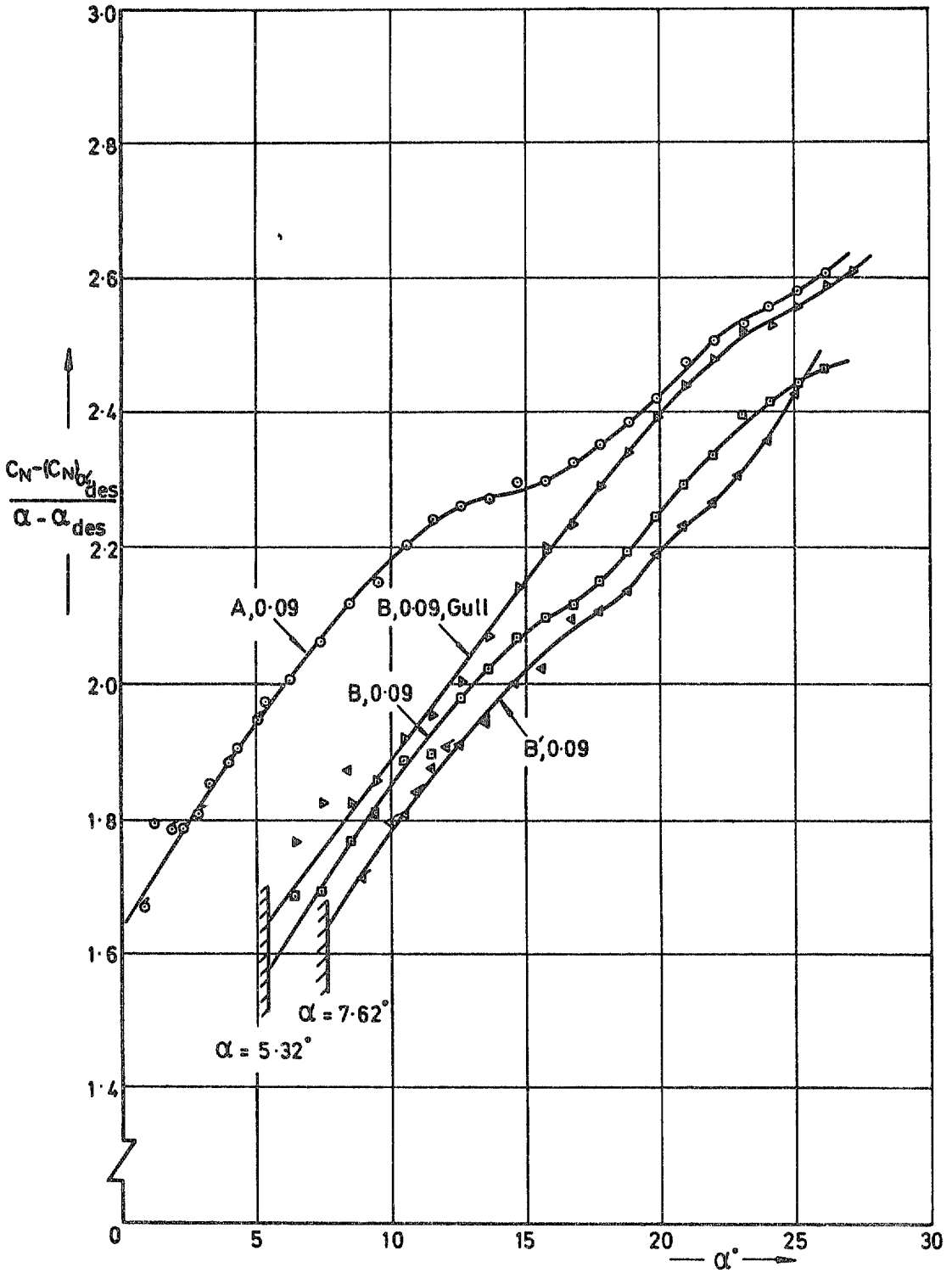

Fig 14 C_N/α vs α (transition fixed)

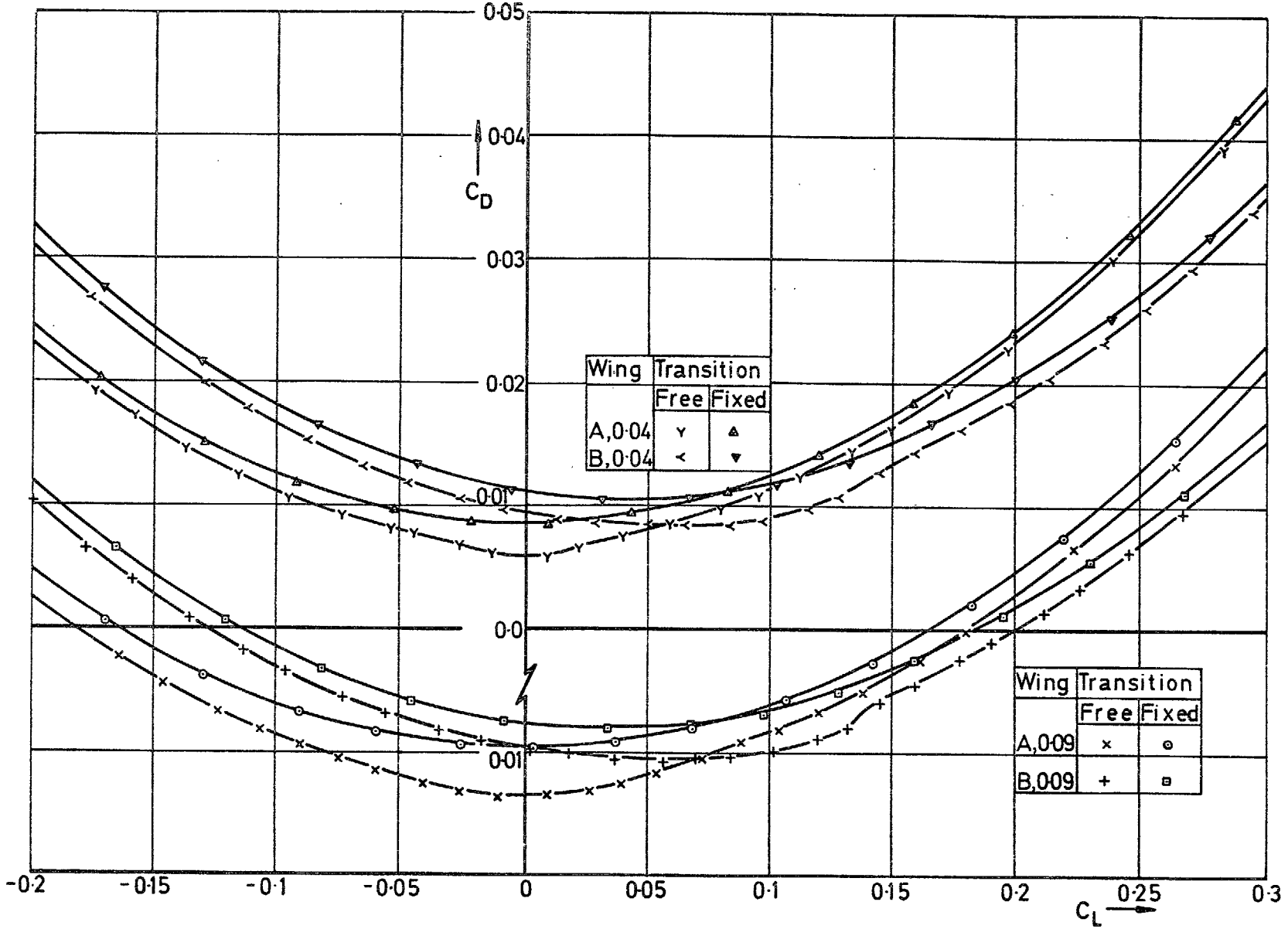

Fig 15 Effect of transition on some drag polars

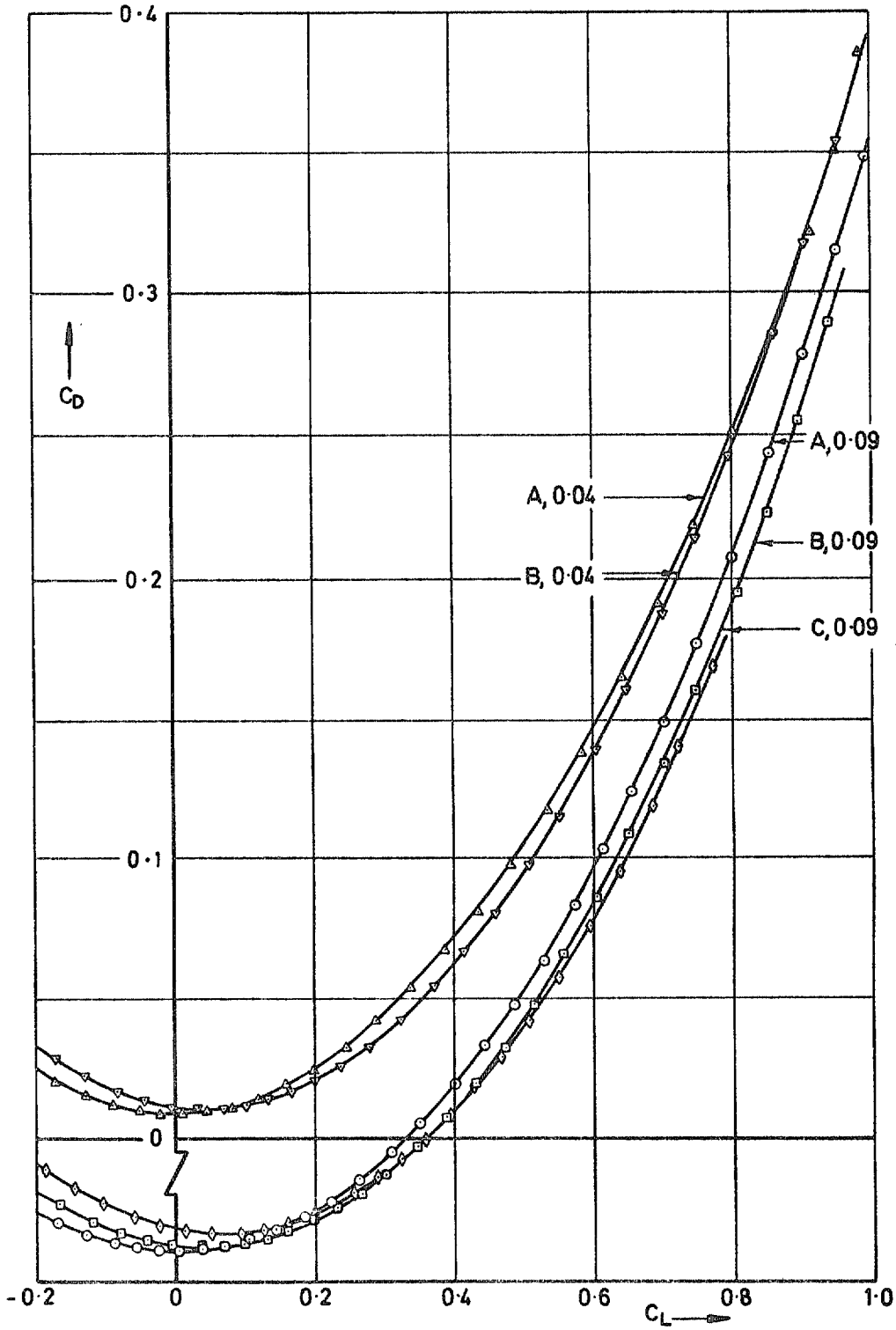

Fig 16 Drag polars of five wings (transition fixed)

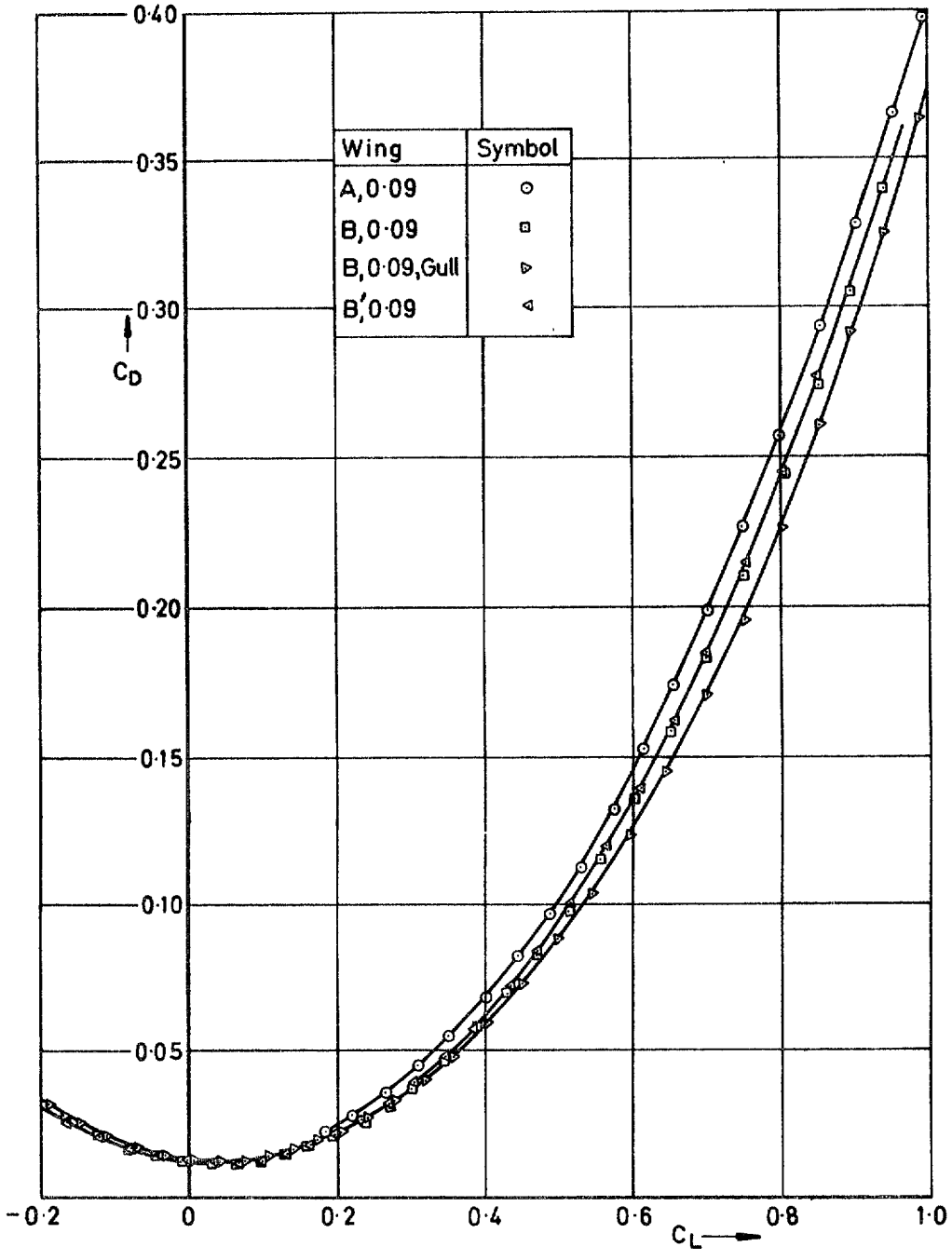

Fig 17 Drag polars of surfaces A, B, B-Gull and B, t/c = 0.09

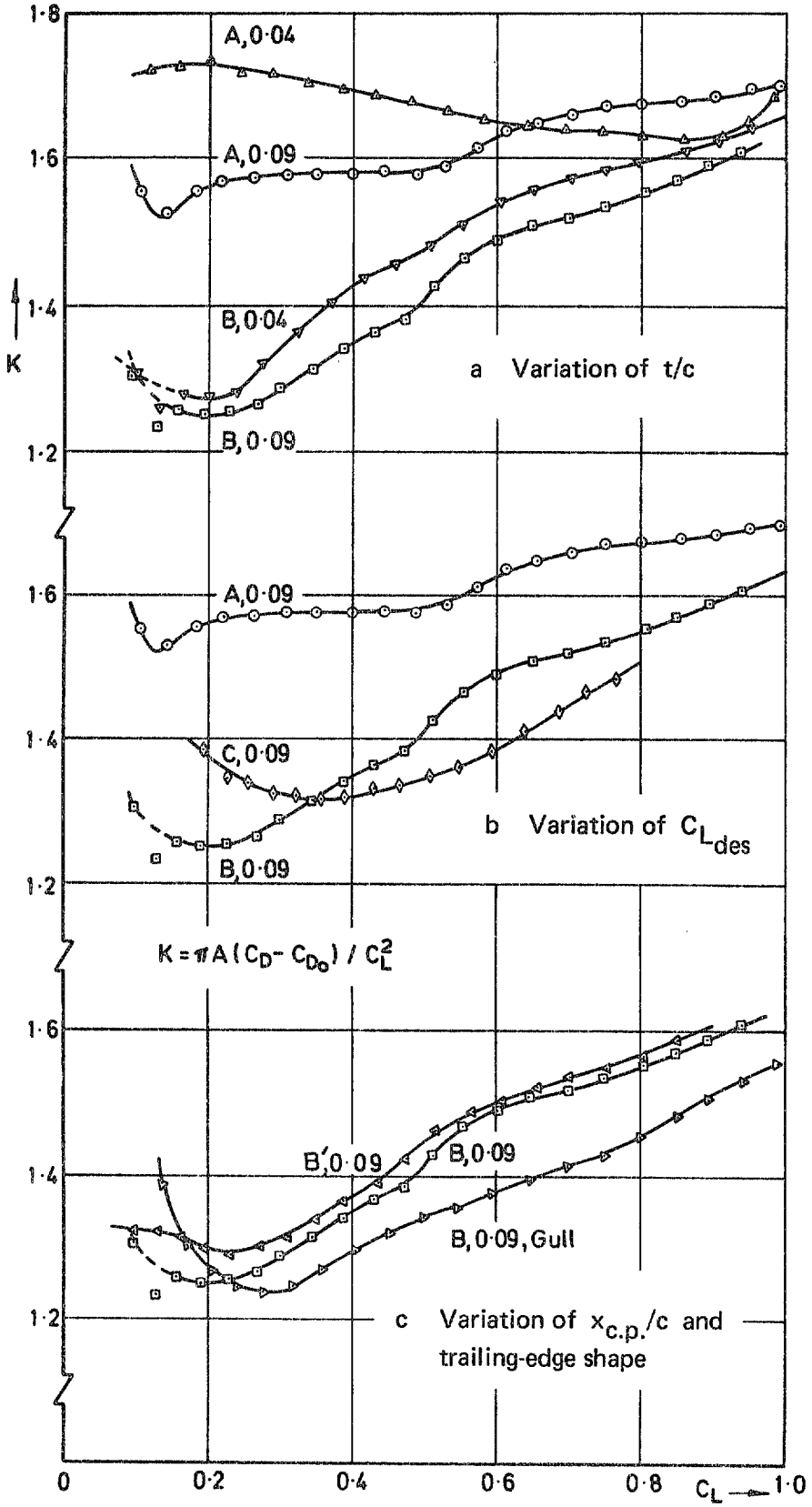

Fig 18a-c Induced drag factor, $K \sim C_L$ for the seven wings

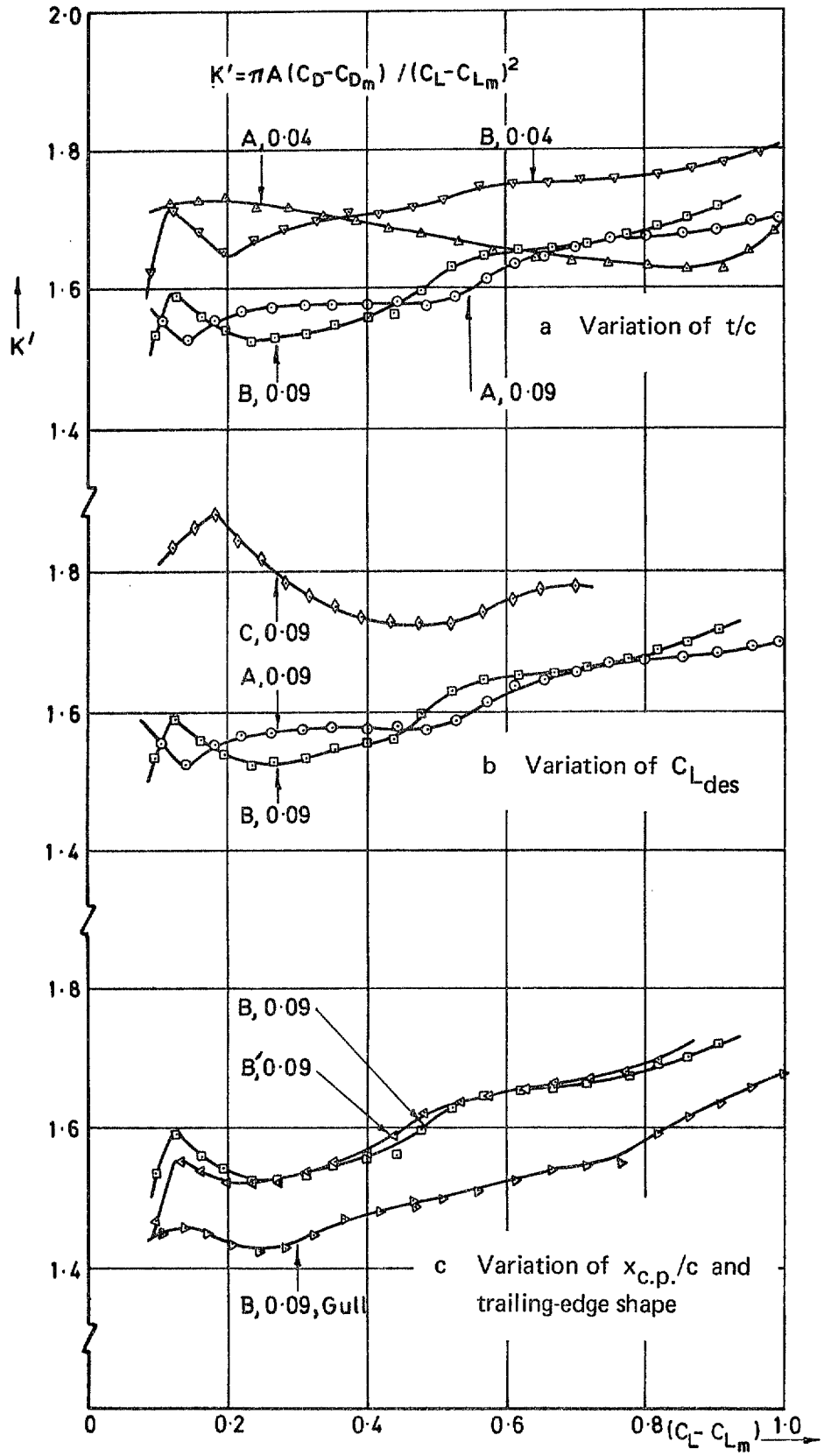

Fig 19a-c K′ vs $(C_L - C_{L_m})$ for the seven wings

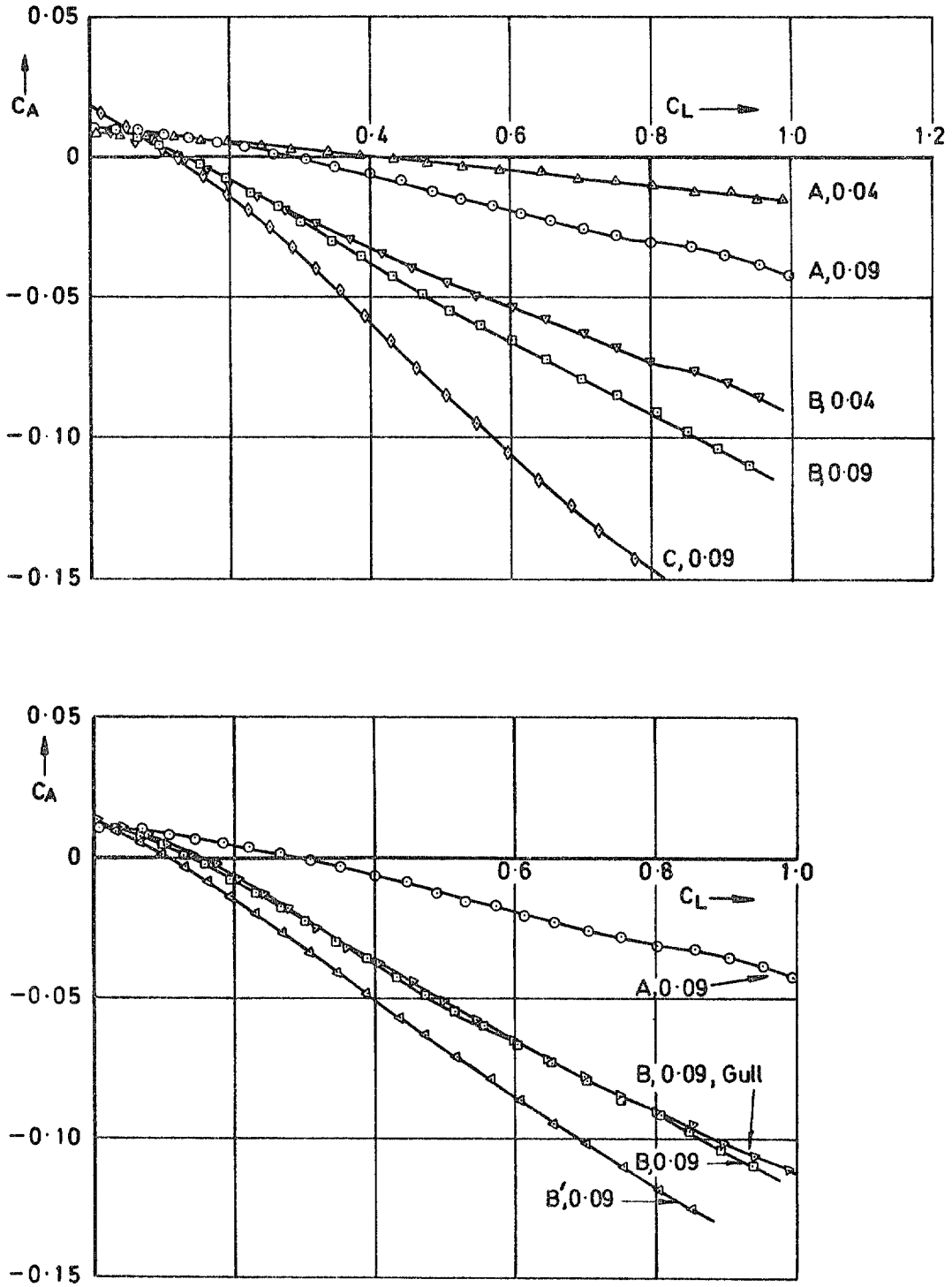

Fig 20 $C_A \sim C_L$ for the seven wings

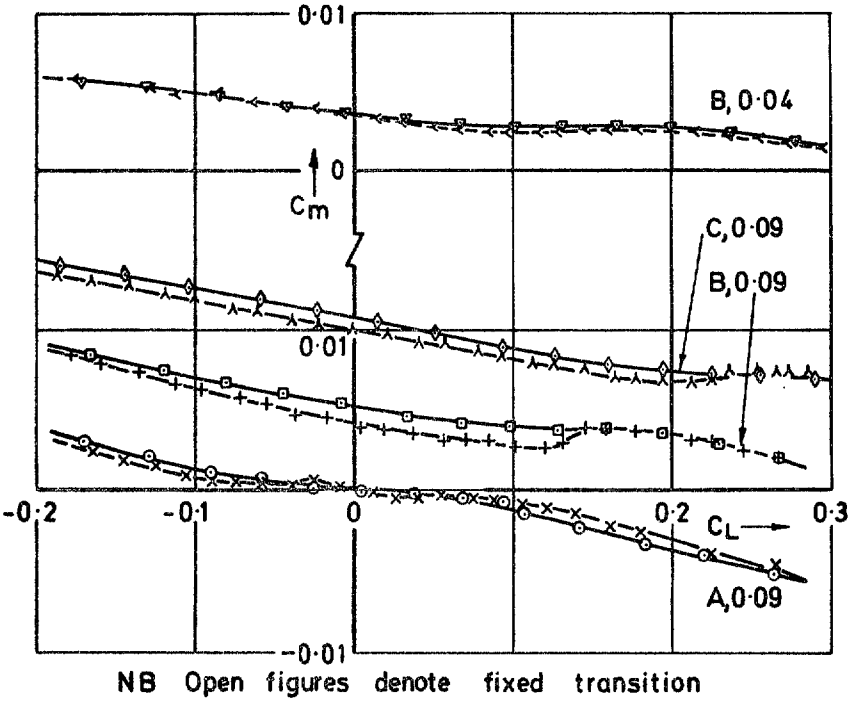

NB Open figures denote fixed transition

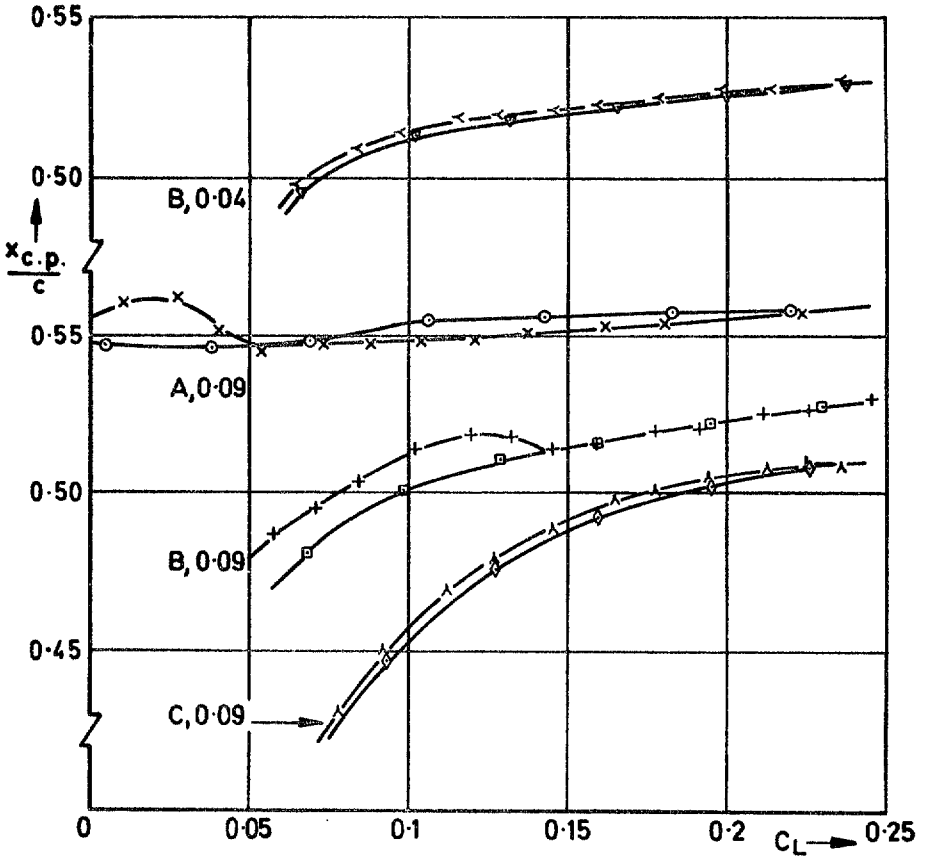

Fig 21 Effects of transition on C_m and $x_{c.p.}/c$

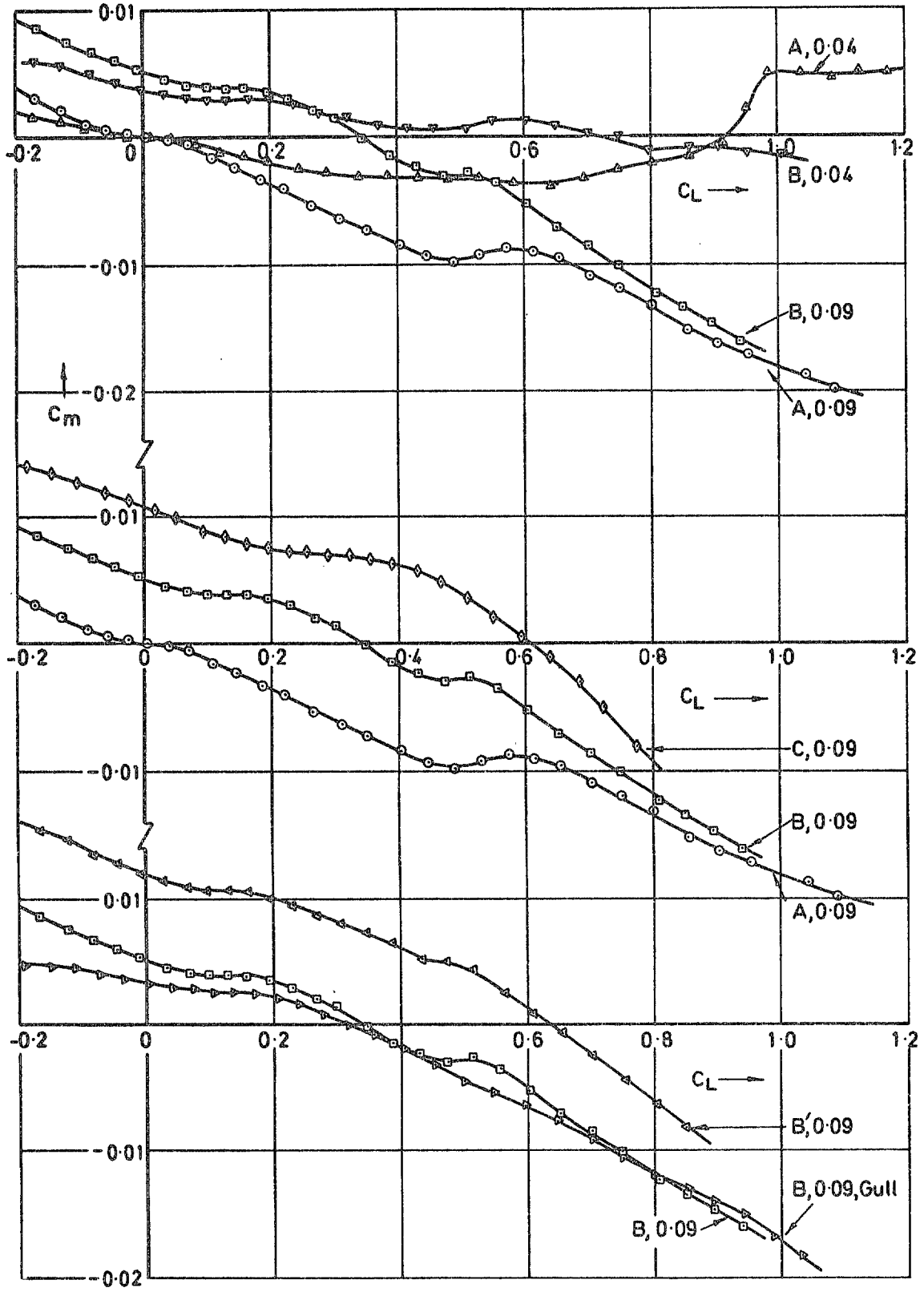

Fig 22 C_m vs C_L for the seven wings

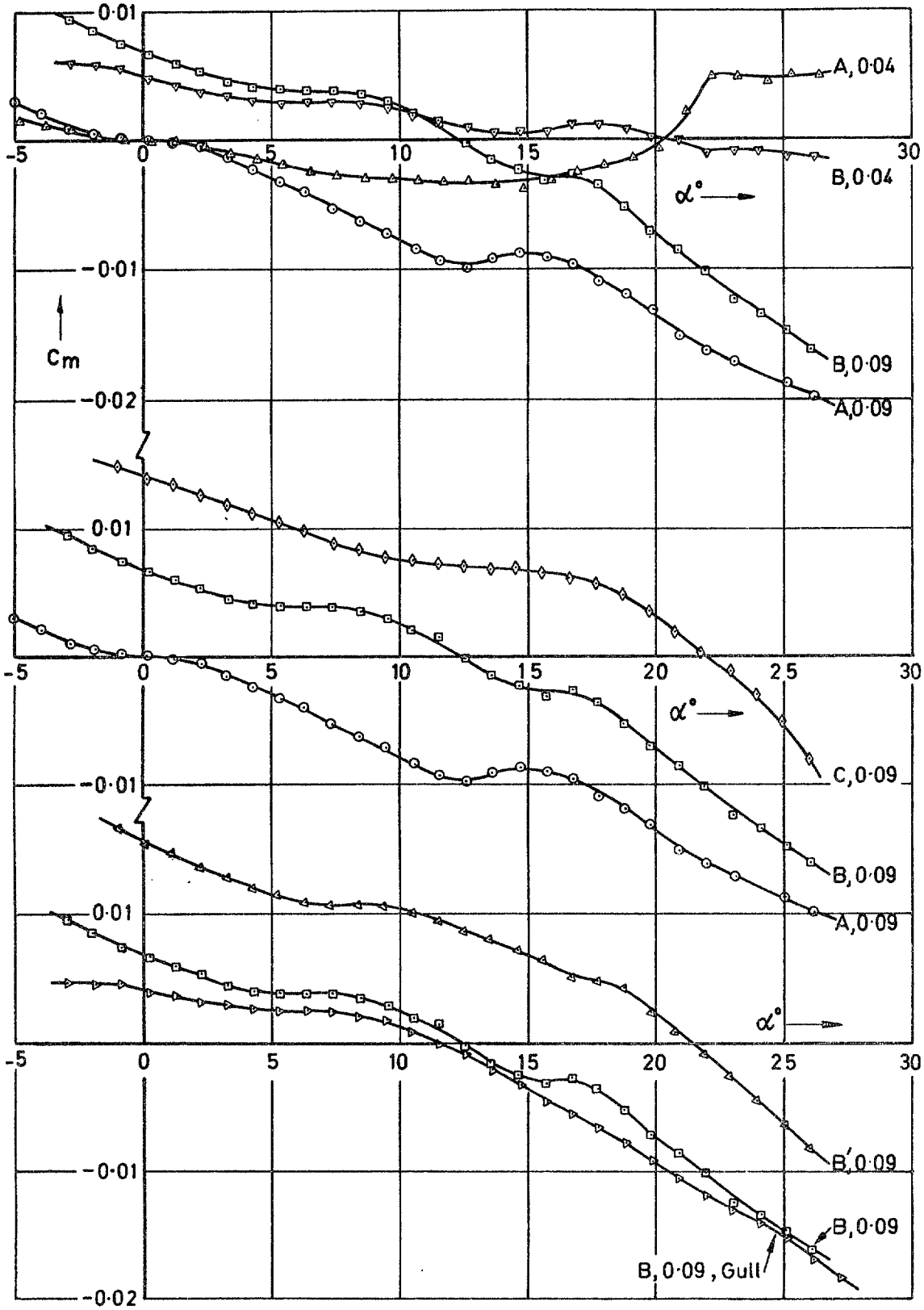

Fig 23 C_m vs α for the seven wings

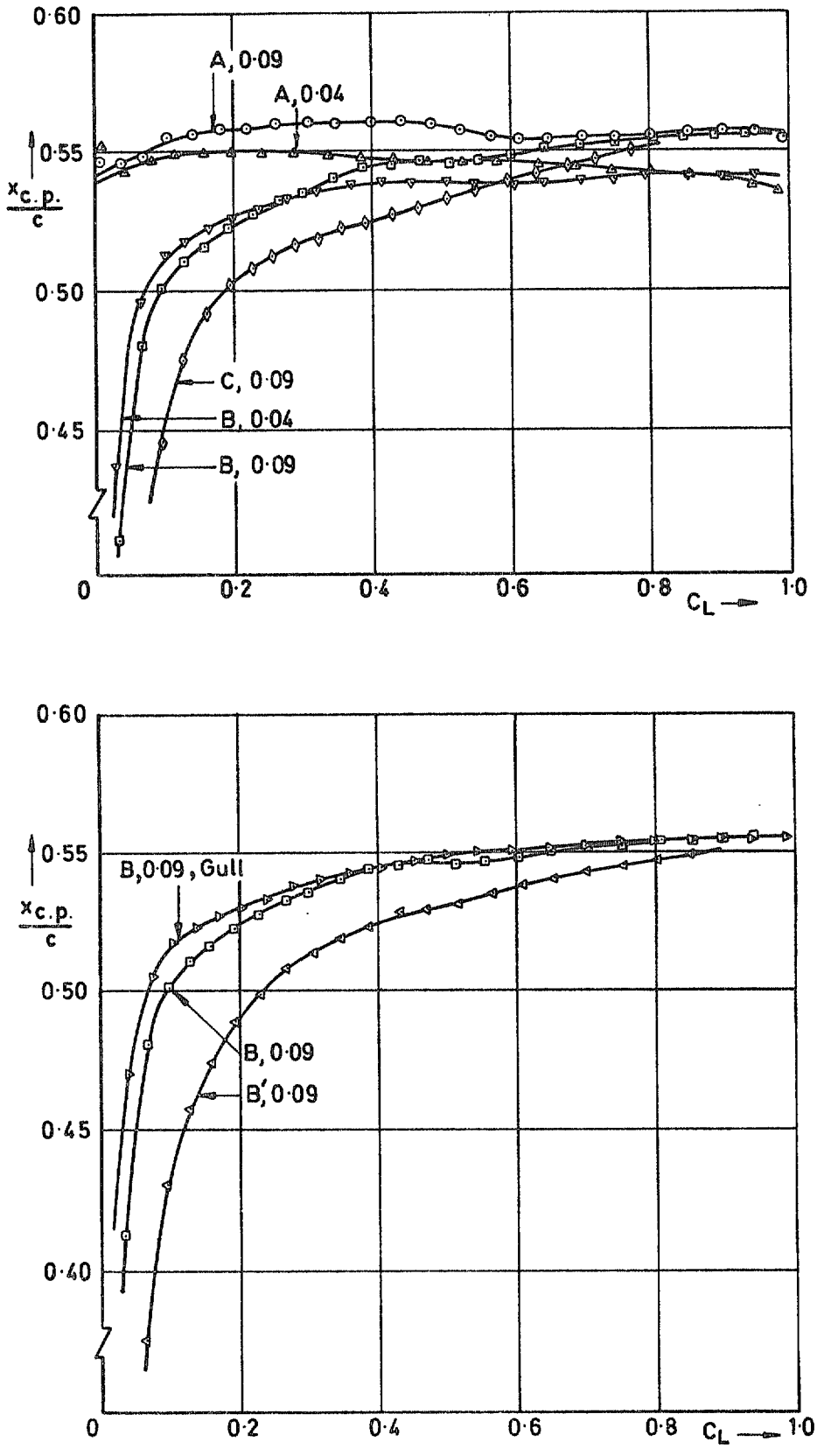

Fig 24 Centre of pressure position, $x_{c.p.}/c$ vs C_L

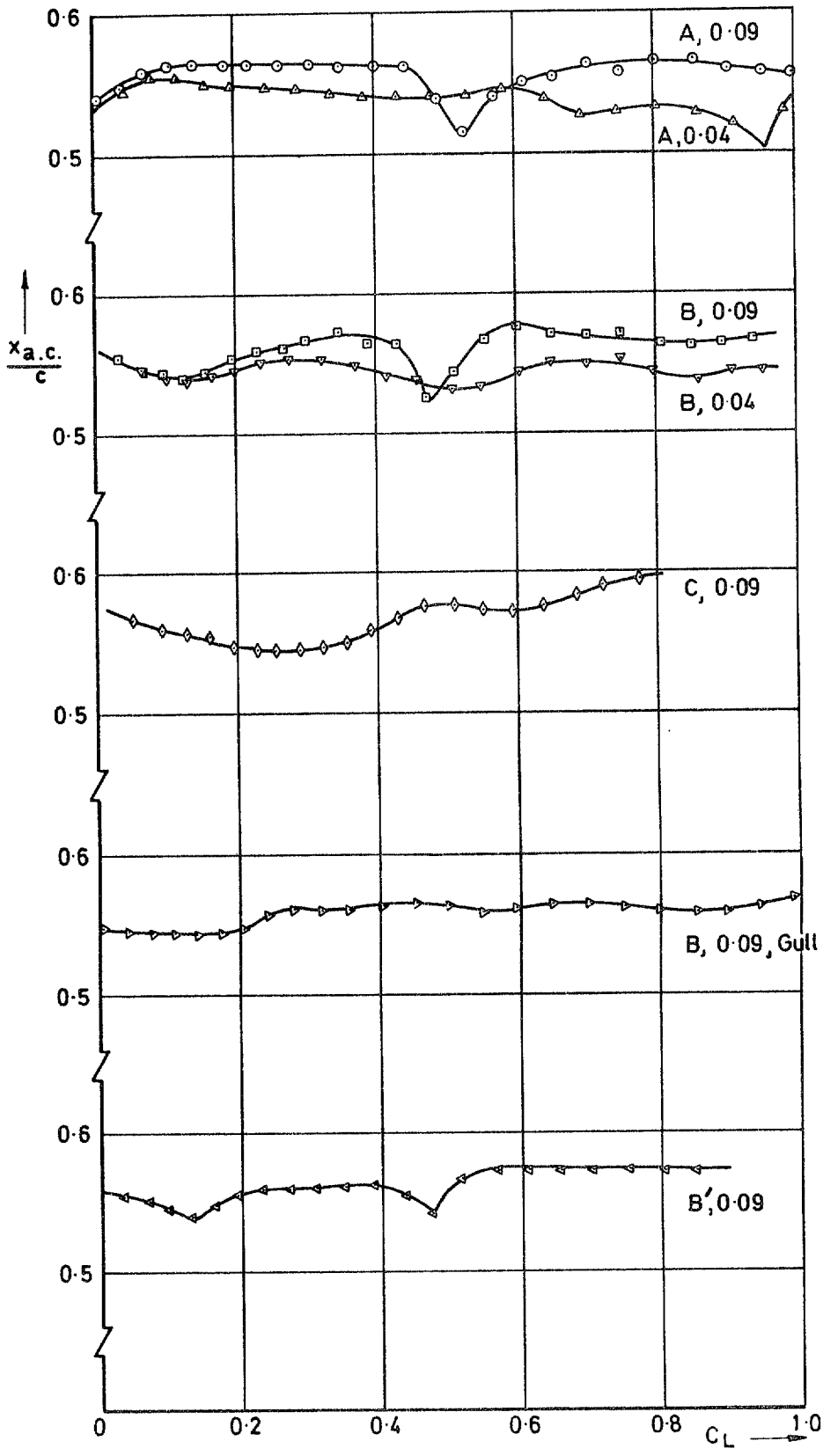

Fig 25 Aerodynamic centre, $x_{a.c.}/c$ vs C_L

Part II

TRANSONIC TESTS

by

P. Lee

SUMMARY

A larger version of one of the wings of Part I, a 9% thick wing of mild gothic planform, designed to have attached leading-edge flow at a lift coefficient of 0.1, has been tested in the RAE 8ft × 6ft transonic tunnel over a Mach number range M = 0.40 to 1.15. Measurements were made of normal force, axial force and pitching moment. The investigation included the effect of varying the test Reynolds number and also the effects of various roughness bands for artificially fixing the boundary-layer transition.

The results at a Reynolds number of 4.1×10^6, based on the wing centre line chord, show that transition fixing on the upper surface forward of the point of maximum chordwise curvature is required to prevent the laminar boundary layer separating at this point. For the condition with transition fixed near the wing leading edge, the non-linear variation of both C_L and C_m with incidence up to a Mach number of 0.94 is basically similar to that at low speed. Increase in Mach number from M = 0.94 to 1.05 at a fixed incidence causes large changes in loading and centre of pressure position. The zero-lift drag-rise Mach number is 0.92, but this decreases to M = 0.89 as C_L is increased to 0.35.

1 INTRODUCTION

Measurements of normal force, axial force and pitching moment acting on a 9% thick cambered wing of mild gothic planform have been made over a Mach number range M = 0.40 to 1.15 in the RAE 8ft × 6ft transonic wind tunnel (Fig 1). This wing is geometrically similar to wing B of Ref 1 (wing B,0.09 of Part I) and utilises a camber surface designed in Ref 2, to give, at low speeds, attached leading-edge flow at a lift coefficient of 0.1 and a centre of pressure position 0.533c downstream of the apex. The incidence for this attached flow condition was calculated to be 5.32°. The results given in Ref 1 show that this design aim was in fact achieved at low subsonic speeds. However, analysis of the results showed that near the design incidence for a test Reynolds number of $R_c = 4.1 \times 10^6$ both normal force and pitching moment were dependent on whether boundary-layer transition was allowed to occur naturally or was artificially fixed. The differences between the transition free and fixed results became very significant at high subsonic Mach numbers.

In view of these results the test programme was extended to investigate the effects of transition fixing and, for a limited incidence range, the effects of increasing Reynolds number with transition occurring naturally.

2 MODEL DETAILS

The wing planform and typical spanwise sections are shown in Fig 2, the main dimensions are listed in Table 1 and the co-ordinates of the spanwise sections illustrated in Fig 2 are given in Table 2. The wing starboard leading edge is defined by $y = S(x) = 0.083344 \left(5\frac{x}{c} - \left(\frac{x}{c}\right)^5\right)$ m; the trailing edge is straight and normal to the centre-line chord.

The model was machined from a billet of light alloy and, with the exception of the trailing edge region, conformed to the theoretical co-ordinates to within ±0.05 mm. On the model the trailing edge had a finite thickness of 0.25 mm. The centre of the wing was machined away to accommodate an existing six component strain gauge balance that had been manufactured with an integral cranked sting. This supporting sting protruded from the wing lower surface forward of the trailing edge (Fig 3) and was partly covered by a shield.

3 EXPERIMENTAL DETAILS

All the transition free and fixed test conditions are listed in Table 3. Geometric details of the various roughness band arrangements referred to in this table are given in Figs 7 and 8, together with dimensions of the ballotini grain

sizes used. At all test conditions measurements were made of the normal force, pitching moment and axial force acting on the model. The mean static pressure in the balance compartment was measured so that the axial force measurements could be adjusted to the condition of free stream static pressure acting on the base of the model. The base area was taken as the total projected area of the opening on the lower surface of the wing when viewed in the direction of arrow X (Fig 3). The measured forces were resolved to give lift and drag, and the pitching moments were transferred to an axis position 54% of the centre-line chord aft of the wing leading-edge apex (0.4477 m). In reducing the results to coefficient form, the gross wing area (0.3223 m^2) and the centre-line chord (0.8291 m) were used as reference area and length respectively.

Theoretical methods of calculating constraint corrections in slotted wall tunnels are suggested in Ref 3 but in view of the uncertainty of their applicability to slender wings no such corrections have been applied to the present results at subsonic speeds*. The results for the Mach number range M = 1.0 to 1.10 are subject to some extent to the influence of reflected bow waves striking the model forward of the trailing edge; however, the strength of the reflected waves is attenuated at the slotted-wall boundary. At M = 1.15 the bow wave is reflected clear of the model and the results are completely free from wall constraint effects. At all Mach numbers the results are subject to the effect of sting interference, this is considered in section 4.2. The estimated balance accuracy, at M = 0.80, $R_c = 4.1 \times 10^6$, for the measured loads in coefficient form is:- $C_L \pm 0.003$; $C_m \pm 0.0003$; $C_D \pm 0.0003$ at $C_L = 0$ changing to $C_D \pm 0.001$ at $C_L = 0.5$. At other test conditions an idea of the accuracy can be obtained by scaling the above values in inverse proportion to the dynamic pressure.

4 PRELIMINARY DISCUSSION OF RESULTS

4.1 Effects of Reynolds number and choice of transition fix

It can be seen from Figs 4 and 5 that for the transition-free condition, an increase in the test Reynolds number in the region of the design incidence of $\alpha = 5.32^\circ$ has an influence on both lift and pitching moment, especially at the higher Mach numbers where only a small increase in Reynolds number is required to cause a marked effect. At all Mach numbers the severity of the instability that occurs between $C_L = 0.1$ and 0.15 is reduced as the Reynolds number is increased

---

* Straightforward application of the method of Ref 3 using the maximum open area ratio at the model position gave an incidence correction $\Delta\alpha = -0.50C_L$ degrees, which significantly degrades the agreement with the low speed work of Ref 1.

and at the higher Mach numbers the marked reduction in $\frac{\partial C_L}{\partial \alpha}$ that occurs at $\alpha \doteq 6^o$, $R_c = 4.1 \times 10^6$, is almost eliminated.

The reason for this large influence of Reynolds number is attributed to the fact that at $R_c = 4.1 \times 10^6$ the flow on the wing upper surface from the leading edge to the point of maximum chordwise curvature (subsequently referred to as the 'shoulder') is largely laminar at the design incidence and flow separations are induced. When the Reynolds number is increased this region of separated flow is progressively suppressed.

The existence of shoulder separations is however not evident from flow pictures taken at $R_c = 4.1 \times 10^6$ (Fig 26) but it is suggested that the presence of the roughness introduced by the flow visualization indicator (castor oil and titanium oxide) gives rise to a turbulent boundary layer. This reasoning is supported by results and flow pictures at $M = 0.96, \alpha = 4.2^o$ given in Fig 15. For this condition there are large differences between the transition fixed and free results for lift and pitching moment, but the loads measured during the transition-free flow-visualization run are in close agreement with the transition fixed results given in Figs 13 and 14. In an effort to obtain visual evidence of a shoulder separation a less viscous flow-visualization indicator, which flowed at very low speeds without rippling, was used and at $M = 0.085, R_c = 1.66 \times 10^6$ a flow picture was obtained which showed the flow separating from the shoulder (Fig 6).

To prevent the results being influenced by shoulder separations, various roughness bands were tried on the wing, positioned as detailed in Figs 7 and 8. The shoulder bands were intended to provoke transition just in front of the transition-free separated region and the leading-edge bands were aimed at ensuring a fully turbulent boundary layer starting near the leading edge. In conjunction with one of the shoulder bands a rear band was added in an attempt to re-energise the boundary layer and thus prevent shock-induced separations occurring in the trailing-edge region at high subsonic Mach numbers (Figs 27 and 28).

Figs 9 and 10 show that the presence of the shoulder roughness bands has a similar effect to increasing the Reynolds number. At all Mach numbers the instability near the design condition is reduced and at $M = 0.94$ and 0.96 the severe kink in the C_L vs α curves is eliminated. The addition of the rear roughness band in conjunction with the shoulder bands at $M = 0.94$ and 0.96 (Fig 11) causes a slight loss of lift and a nose-up change of moment, but it does not have any beneficial effects on stability.

The differences in lift and pitching moment caused by the leading-edge roughness bands (Figs 12 to 14 and 16) are also similar to the changes resulting

from increasing the test Reynolds number. Comparison of the results for the shoulder and leading-edge bands shows that although both roughness configurations have an almost identical effect on lift at high subsonic speeds, the leading-edge bands are more effective in reducing the instability that occurs near the design incidence. Of the two leading-edge roughness bands tried the 120 grade band is, with the exception of M = 0.98, slightly more effective in this respect than the band formed with the large ballotini. Based on these results it was considered that the 120 grade leading-edge roughness bands effectively fixed boundary layer transition at all test Mach numbers at a Reynolds number of 4.1×10^6.

4.2 Comparison with previous low speed tests

The lift and pitching moment results at M = 0.4 derived from the 8ft × 6ft tunnel tests are compared in Figs 17 and 18 with results from tests made on a geometrically similar model in a low speed wind tunnel.

It can be seen from Fig 17 that although the M = 0.4 results are displaced from the low speed values by an incidence increment of approximately $\Delta\alpha = 0.3^\circ$ the variation of C_L with incidence is basically similar for both tests, $\frac{\partial C_L}{\partial \alpha}$ having a minimum value in the region of the design condition.

The pitching moment comparison, Fig 18, also shows similar features for both sets of results, $\frac{\partial C_m}{\partial C_L}$ having minimum values at approximately the design loading and also at $C_L \simeq 0.5$ where vortex breakdown occurs[1]. The reduction in $\frac{\partial C_m}{\partial C_L}$ at the design point is more severe for the low speed results than for the M = 0.4 results and is possibly due to the low speed transition fixing not being completely effective at this Reynolds number. No explanation is offered for the differences in pitching moment that occur between the two tests at vortex breakdown. Over the range $C_L = -0.1$ to 0.45 the pitching moments for the low speed tests are slightly more nose up than for the M = 0.4 results.

The low speed results used in this comparison have been fully corrected for tunnel wall constraint and support interference. No corrections of this type have been applied to the M = 0.4 8ft × 6ft tunnel results. It is not thought that the differences between the two sets of lift results (Fig 17) are due to the need for a constraint correction on the latter, as the differences do not depend on lift coefficient and occur at $C_L = 0$ where wall constraint effects would be virtually zero. Sting interference is thought to be the most likely cause of these differences, since the presence of the sting and its associated shield (Fig 3) effectively increase the camber over the rear of the wing at the centre section. This

would be expected to cause an increase in lift and a nose-down moment, although in this case the balance only measures the loads on the shield and the loads that the sting induces on the wing.

From the comparisons given in Figs 17 and 18 it is estimated that the sting interference at low incidence amounts to

$$\Delta C_L \triangleq 0.01 , \qquad \Delta C_m \triangleq -0.0004 .$$

These corrections have not been applied to the results discussed in section 5 as they are only strictly applicable at low subsonic Mach numbers.

5 ANALYSIS OF RESULTS

5.1 Variation with Mach number

5.1.1 Lift and pitching moment

The lift and pitching moment data for the tests with transition fixed at the leading edge by 120 grade ballotini bands are given in Figs 19 to 25. Flow visualization pictures showing the development of the flow on the wing upper surface are presented in Figs 26 to 28. These flow pictures were obtained without transition fixing roughness bands but as mentioned in section 4.1 it is considered that the presence of the flow visualization indicator acted as a transition trip.

Figs 19 and 20 show that the low-speed, non-linear variation of C_L with incidence is not dramatically altered as the speed is increased subsonically. $\frac{\partial C_L}{\partial \alpha}$ has a minimum value between $\alpha = 4^o$ to 6^o and increases progressively as the incidence is raised above this range. These changes in $\frac{\partial C_L}{\partial \alpha}$ correspond, at low speed, to the condition of attached flow at the leading edge and the development of leading-edge vortices. It can be seen from Fig 26 that at the design incidence of 5.32^o the upper surface flow remains attached as the Mach number is increased from M = 0.40 to M = 0.94 but that at M = 0.94 (Fig 27) the flow from the upper surface leading edge separates as the incidence is increased above $\alpha = 5.32^o$.

Fig 23 shows that below $C_L = 0.4$ and up to a Mach number of 0.94 the variation of C_m vs C_L is basically similar to that at low speed, $\frac{\partial C_m}{\partial C_L}$ having a minimum value in the region of $C_L = 0.1$ to 0.2.

The reduction in stability that occurs in this C_L range becomes somewhat more severe as the Mach number is increased above M = 0.70. The second reduction in stability that occurs at $C_L \triangleq 0.5$, M = 0.4 and is associated with vortex breakdown is present in the C_m vs C_L curves for M = 0.55 and 0.70 but is disappearing by M = 0.80.

Increasing Mach number through the transonic speed range, M = 0.94 to 1.05, causes large changes in the variation of both C_L vs α and C_m vs C_L. Between M = 0.94 and M = 0.98 the variation of C_L with incidence (Fig 20) becomes increasingly non-linear but as the Mach number is further increased to supersonic speeds the relationship becomes almost linear. Similarly the variation of C_m vs C_L goes through a highly non-linear phase, M = 0.96 to 1.00 (Fig 22) before also becoming almost linear at M = 1.05. The dependence of pitching moment on small changes in Mach number in the transonic range is clearly illustrated by Fig 25; for instance for C_L = 0.1 and 0.2, the pitching moment increases between M = 0.94 and 0.98 and then rapidly decreases between M = 0.98 and 1.05. This forward movement of the centre of pressure, followed by a sudden rearward movement, can be attributed to the development and suppression of shock induced separated regions on the wing upper surface in the region of the trailing edge, prior to the shockwave being located firmly at the trailing edge at low supersonic speeds. For the Mach number range M = 1.05 to 1.15 the variation of both C_L vs α and C_m vs C_L is almost linear.

5.1.2 Drag

Figs 29 to 31 give the transition fixed (leading-edge bands, 120 grade ballotini) drag results in the form of C_D vs C_L and C_D vs M curves. It can be seen from Figs 29 and 30 that C_D varies smoothly with C_L at all Mach numbers and that the minimum drag occurs at $C_L \triangleq 0.05$. The drag rise Mach number (Fig 31) at zero lift is M = 0.92; this value decreases with increasing lift coefficient, becoming M = 0.89 at C_L = 0.35. At the higher lift coefficients the value of the drag coefficient at the onset of the drag rise is less than the low speed value. For the C_L range covered by the tests it can be seen from Fig 31 that C_D continues to rise steeply as the Mach number is increased above the drag rise value and C_D reaches a maximum between M = 1.05 and 1.10.

5.2 Comparison of design parameters with theory

The variation with Mach number of the lift coefficient and centre-of-pressure position at the design incidence of $\alpha = 5.32^{\circ}$ is shown in Figs 32 and 33. At M = 0.4 at this incidence, C_L = 0.112 and the centre-of-pressure is at 0.519c, whereas the subsonic theory predicts for this incidence C_L = 0.1 and a centre-of-pressure at 0.533c. At this speed most of the discrepancy between the measured and theoretical lift loading can be attributed to sting interference effects, discussed in section 4.2, and these also have a small effect on centre-of-pressure position. $(C_L)_{\alpha=5.32^{\circ}}$ increases by 0.008 as the Mach number is raised from M = 0.4 to 0.8 but the centre-of-pressure position does not change. Between

M = 0.80 and 0.94 the value of $(C_L)_{\alpha=5.32^o}$ continues to increase, reaching a maximum subsonic value at M = 0.94 which is 0.017 above the low speed value. This is associated with a 0.01c forward change in the centre-of-pressure position.

Increase of Mach number in the transonic speed range M = 0.94 to 1.05 causes much larger changes in lift and centre-of-pressure position. For this speed range $(C_L)_{\alpha=5.32^o}$ reaches a minimum value at M = 0.98 and the centre-of-pressure position is then furthest forward; a maximum value of lift coefficient and a most rearward centre-of-pressure position occurs at M = 1.05. Between these two speeds $(C_L)_{\alpha=5.32^o}$ increases by 0.047 and the corresponding centre-of-pressure shift is as much as 0.14c. The centre-of-pressure position remains almost constant from M = 1.05 to 1.15 and as the speed is increased over this range $(C_L)_{\alpha=5.32^o}$ decreases more slowly.

6 CONCLUSIONS

Investigation of the longitudinal forces and moments measured on this 9% thick cambered mild gothic wing has shown that:

(1) At the main test Reynolds number of 4.1×10^6 boundary-layer transition fixing is required to prevent flow separations occurring at the point of maximum chordwise curvature.

(2) Transition fixed, the non-linear variation of C_L and C_m with incidence is basically similar to the pattern at low speed up to M = 0.94.

(3) Large changes in lift loading and centre of pressure position occur as the Mach number is increased from M = 0.94 to 1.05.

(4) The zero-lift drag rise Mach number is 0.92, decreasing to M = 0.89 if C_L is increased to 0.35.

(5) At M = 0.4, most probably due to sting interference, the measured lift coefficient at the design incidence $\alpha = 5.32^o$ is greater than the theoretical value by $\Delta C_L = 0.012$. The lift acts 0.014c forward of the position predicted.

(6) Increase of Mach number over the range M = 0.98 to 1.05 at the design incidence causes a loading increase of $\Delta C_L = 0.047$ and a corresponding centre-of-pressure shift 0.14c aft.

Table 1

Model details

Wing area	0.3223 m^2
Centre line chord	0.8291 m
Aspect ratio	1.378
Maximum thickness chord ratio	8.9%
Slenderness ratio	0.402
Pitching moment centre aft of wing leading-edge apex	0.4477 m (0.54c)

Thickness distribution given by $z = \pm B(x)(1 - y^2/S^2(x))$

where $S(x) = 0.083344\ (5(x/c) - (x/c)^5)$ is the starboard leading edge and

$$B(x) = 0.82548x/c(1 - x/c)(0.29224 - 0.68199\ x/c + 1.60782(x/c)^2 - 1.72866(x/c)^3 + 0.69079(x/c)^4)$$

is the centre-line thickness distribution (in metres).

Table 2

SPANWISE SECTIONS (ALL DIMENSIONS IN MILLIMETRES)

For system of axes used see Fig 2

x/c = 0.06		x = 49.530	
Upper surface		Lower surface	
y	z	y	z
0	82.687	0	58.778
0.833	82.674	0.833	58.793
1.669	82.641	1.669	58.839
2.499	82.586	2.499	58.915
3.332	82.501	3.332	59.019
4.168	82.390	4.168	59.149
5.113	82.248	4.892	59.296
6.071	82.067	5.601	59.464
7.048	81.844	6.289	59.649
8.049	81.575	6.957	59.847
9.073	81.257	7.597	60.056
10.122	80.889	8.217	60.282
11.189	80.462	8.814	60.521
12.273	79.974	9.398	60.772
13.363	79.428	9.977	61.036
14.448	78.811	10.559	61.311
15.517	78.130	11.156	61.587
16.561	77.379	11.781	61.869
17.564	76.563	12.441	62.144
18.519	75.677	13.152	62.400
19.416	74.729	13.924	62.639
20.249	73.729	14.757	62.842
21.013	72.682	15.662	63.015
21.709	71.592	16.632	63.144
22.337	70.460	17.671	63.228
22.903	69.286	18.773	63.261
23.409	68.105	19.936	63.276
23.861	66.909	21.148	63.266
24.270	65.682	22.405	63.228
24.648	64.437	23.696	63.195
25.004	63.195	25.004	63.195

x/c = 0.30		x = 247.650	
Upper surface		Lower surface	
y	z	y	z
0	81.951	0	15.636
4.331	81.905	3.993	15.664
8.666	81.768	7.978	15.751
13.012	81.542	11.953	15.898
17.371	81.211	15.916	16.091
21.742	80.772	19.865	16.327
26.124	80.226	23.805	16.604
30.518	79.566	27.732	16.922
34.922	78.786	31.648	17.275
39.337	77.892	35.552	17.663
43.762	76.876	39.451	18.085
48.189	75.733	43.345	18.537
52.616	74.465	47.236	19.020
57.043	73.068	51.130	19.530
61.460	71.542	55.034	20.066
65.867	69.880	58.951	20.627
70.254	68.087	62.885	21.209
74.610	66.154	66.848	21.808
78.933	64.069	70.846	22.403
83.213	61.824	74.887	22.990
87.442	59.433	78.979	23.553
91.608	56.822	83.134	24.082
95.705	54.064	87.358	24.567
99.720	51.133	91.664	25.011
103.645	48.031	96.060	25.395
107.472	44.768	100.554	25.723
111.189	41.341	105.159	25.979
114.790	37.755	109.878	26.152
118.265	34.018	114.724	26.238
121.608	30.145	119.700	26.238
124.816	26.149	124.816	26.149

Table 2 (concluded)

x/c = 0.60		x = 495.300	
Upper surface		Lower surface	
y	z	y	z
0	60.950	0	-9.581
8.118	60.891	8.118	-9.563
16.238	60.716	16.238	-9.505
24.356	60.419	24.356	-9.406
32.474	60.005	32.474	-9.272
40.592	59.484	40.592	-9.091
48.712	58.852	48.712	-8.860
56.830	58.108	56.830	-8.585
64.948	57.262	64.948	-8.255
73.066	56.342	73.066	-7.841
81.186	55.334	81.186	-7.363
89.304	54.239	89.304	-6.812
97.422	53.068	97.422	-6.180
105.542	51.831	105.542	-5.458
113.660	50.523	113.660	-4.648
122.349	49.139	121.206	-3.749
130.741	47.676	129.052	-2.766
138.953	46.139	137.076	-1.709
147.086	44.511	145.181	-0.589
155.209	42.769	153.292	0.572
163.375	40.871	161.364	1.740
171.607	38.786	169.367	2.885
179.908	36.482	177.305	3.985
188.260	33.904	185.191	4.991
196.621	31.003	193.065	5.862
204.940	27.678	200.985	6.492
213.147	23.873	209.012	6.812
221.173	19.563	217.226	6.756
228.945	14.671	225.687	6.185
236.416	9.063	234.455	4.874
243.552	2.685	243.552	2.685

x/c = 0.90		x = 742.950	
Upper surface		Lower surface	
y	z	y	z
0	18.743	0	-7.089
10.864	18.743	10.864	-7.082
21.722	18.651	21.722	-7.066
32.586	18.537	32.586	-7.036
43.447	18.385	43.447	-6.988
54.308	18.191	54.308	-6.922
65.169	17.958	65.169	-6.840
76.030	17.704	76.030	-6.721
86.891	17.424	86.891	-6.571
97.752	17.115	97.752	-6.391
108.613	16.797	108.613	-6.165
119.474	16.462	119.474	-5.898
130.335	16.109	130.335	-5.588
141.196	15.753	141.196	-5.227
152.057	15.387	152.057	-4.818
162.918	15.011	162.918	-4.364
173.779	14.605	173.779	-3.879
184.643	14.171	184.643	-3.366
195.504	13.716	195.504	-2.817
206.365	13.160	206.365	-2.311
217.310	12.507	217.142	-1.844
228.239	11.770	227.935	-1.400
239.169	10.825	238.727	-1.107
250.104	9.652	249.514	-0.983
261.038	8.293	260.302	-0.978
271.968	6.528	271.094	-1.318
282.875	4.298	281.910	-2.060
293.738	1.699	292.771	-3.114
304.533	-1.572	303.698	-4.793
315.237	-5.629	314.714	-7.239
325.836	-10.310	325.836	-10.310

Co-ordinates of:- Leading-edge apex x = 0, y = 0, z = 76.825
Starboard tip x = 825.500, y = 333.375, z = 0
Port tip x = 825.500, y = -333.375, z = 0

Table 3 - TEST CONDITIONS

(a) Transition free

Mach number	Reynolds number $R_c \times 10^{-6}$	Nominal incidence range, degrees
0.40	4.1 8.2 14.2	-2 to 20 -2 to 15 ½ to 11
0.70	4.1	-2 to 17
0.85	4.1 6.0	-1½ to 12 -½ to 10
0.90, 0.92	4.1	-1½ to 10
0.94	4.1 5.4	-1 to 10 -1 to 9
0.96	4.1 5.4	-1 to 10 -½ to 8
0.98, 1.05	4.1	-1 to 10

(b) Transition fixed, $R_c = 4.1 \times 10^6$

Roughness configuration	Mach number	Nominal incidence range, degrees
Shoulder roughness band, 85 grade ballotini, see Fig 7	0.4 0.7 0.85 0.90, 0.92 0.94	-2 to 20 -2 to 17 -1½ to 12 -1½ to 10 -1 to 10
Shoulder roughness band, 72 grade ballotini, see Fig 7	0.4 0.7 0.85 0.90, 0.92 0.94, 0.96	-2 to 20 -2 to 17 -1½ to 12 -1½ to 10 -1 to 10
Shoulder band, 72 grade ballotini + rear band 36 grade ballotini, see Fig 7	0.94, 0.96	-1 to 10
Leading-edge roughness bands. 100 grade ballotini, see Fig 8	0.40 0.70 0.85 0.90, 0.92 0.94, 0.96, 0.98 1.05	-2 to 20 -2 to 17 -1½ to 12 -1½ to 10 -1 to 10
Leading-edge roughness bands 120 grade ballotini, see Fig 8	0.4 0.55 0.7 0.8 0.85, 0.88 0.90, 0.92, 0.94 0.96, 0.98, 1.00 1.02, 1.05, 1.10	-2 to 20 -2 to 18 -1½ to 17 -1 to 15 -1 to 12 -1 to 10 -1 to 10 -1 to 10

LIST OF SYMBOLS

c	centre-line chord
C_D	drag coefficient D/qS
C_L	lift coefficient L/qS
C_m	pitching moment coefficient taken about 0.54c from wing apex M/qSc
C_x	axial force coefficient
R_c	Reynolds number based on centre-line chord
q	tunnel kinetic pressure $\frac{1}{2}\rho V^2$
S	wing area
x	chordwise distance from apex in plane of definition
y	spanwise distance from centre line
z	third axis forming a right handed system of axes with x and y
α	angle of incidence (incidence of line joining apex to centre of trailing edge)

REFERENCES

No.	Author	Title, etc
1	P.J. Butterworth	Low speed wind-tunnel tests on a family of cambered wings of mild gothic planform of aspect ratio 1.4. ARC CP No.1163 (1970)
2	Patricia J. Davies	The design of a series of warped slender wings for subsonic speeds. ARC CP No.1263 (1971)
3	H.C. Garner (Editor)	Subsonic wind tunnel wall corrections. AGARDograph 109 (1966)

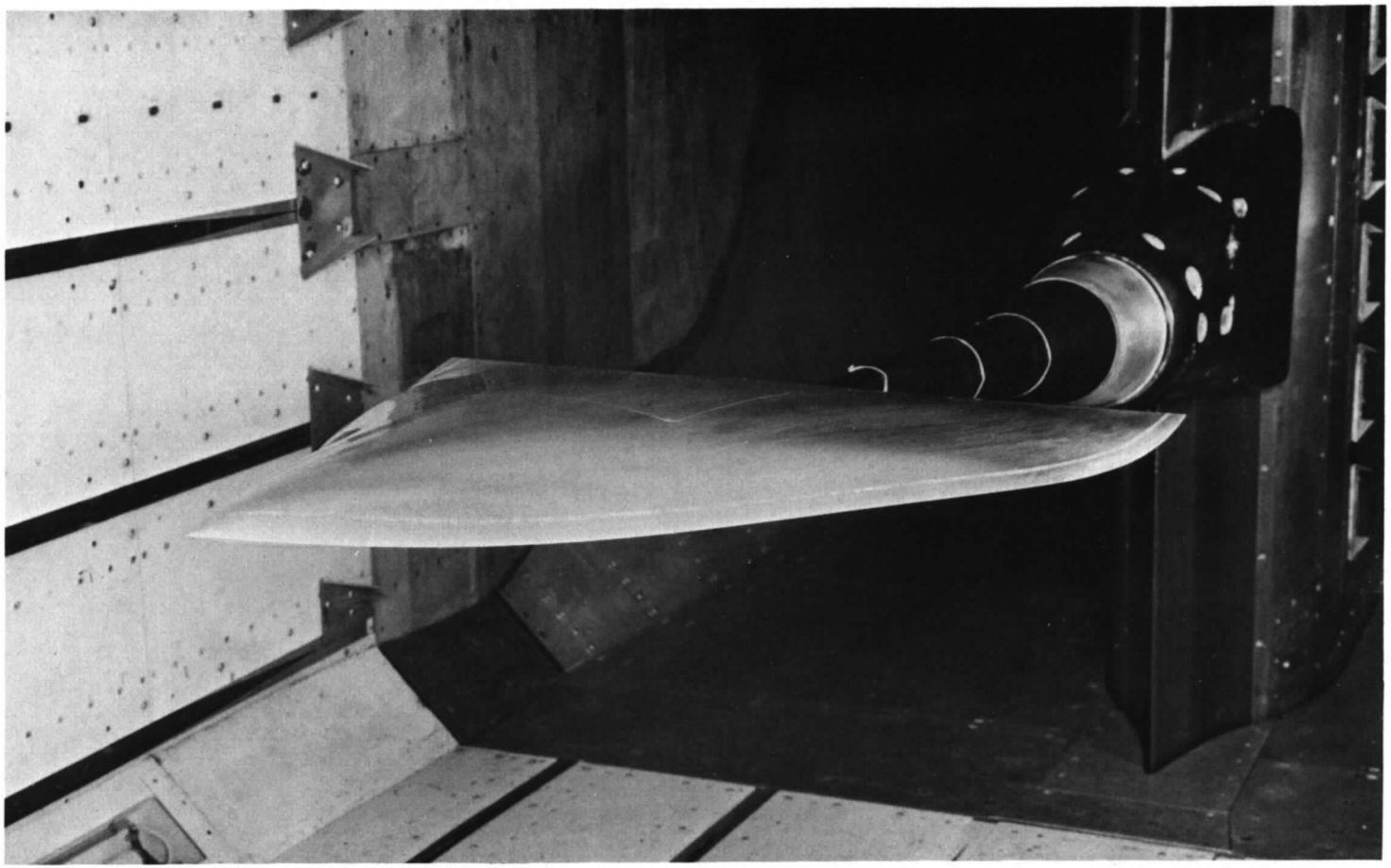

Fig 1 Model in 8ft x 6ft transonic wind tunnel

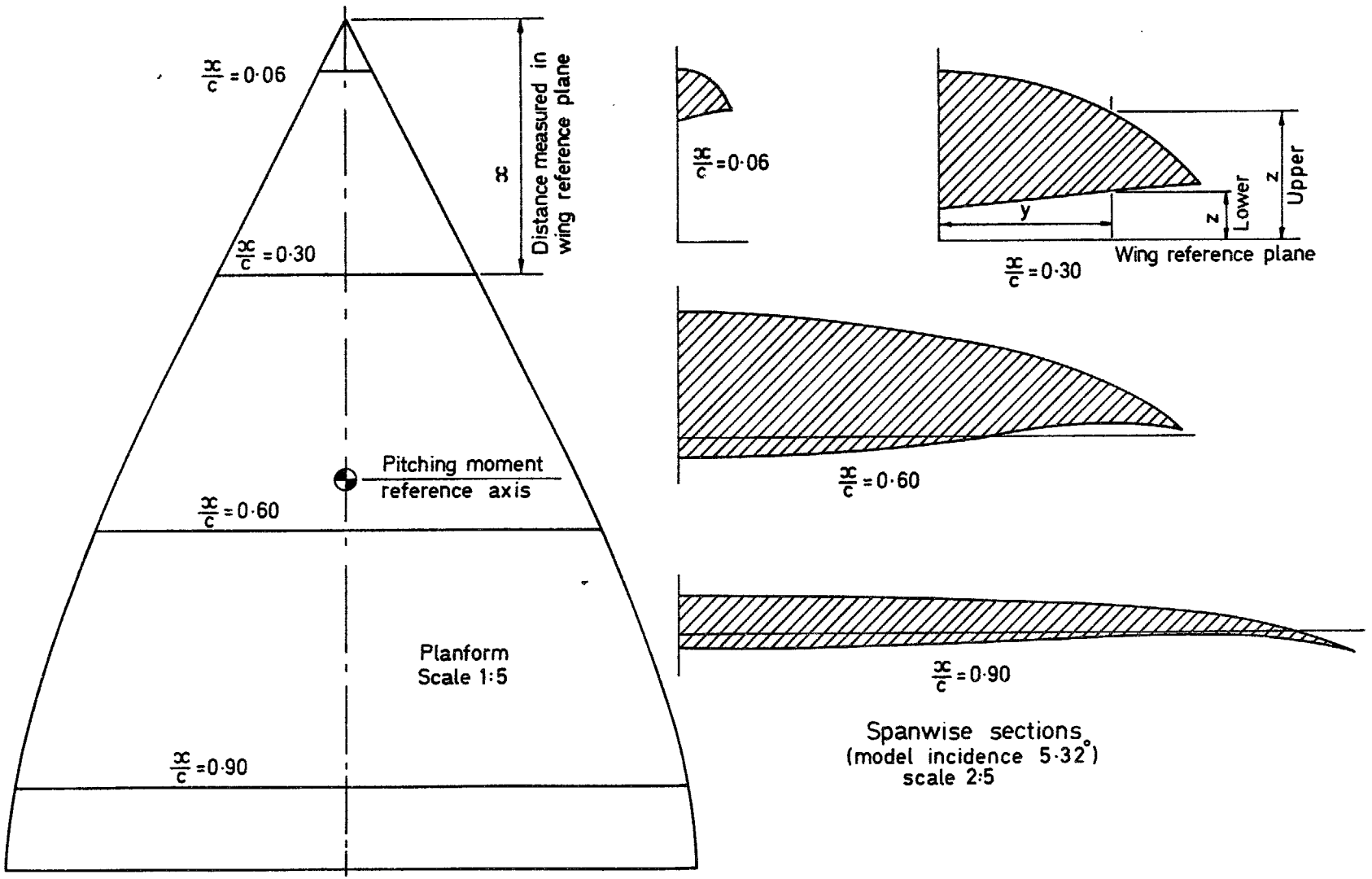

Fig 2 Geometric details of wing

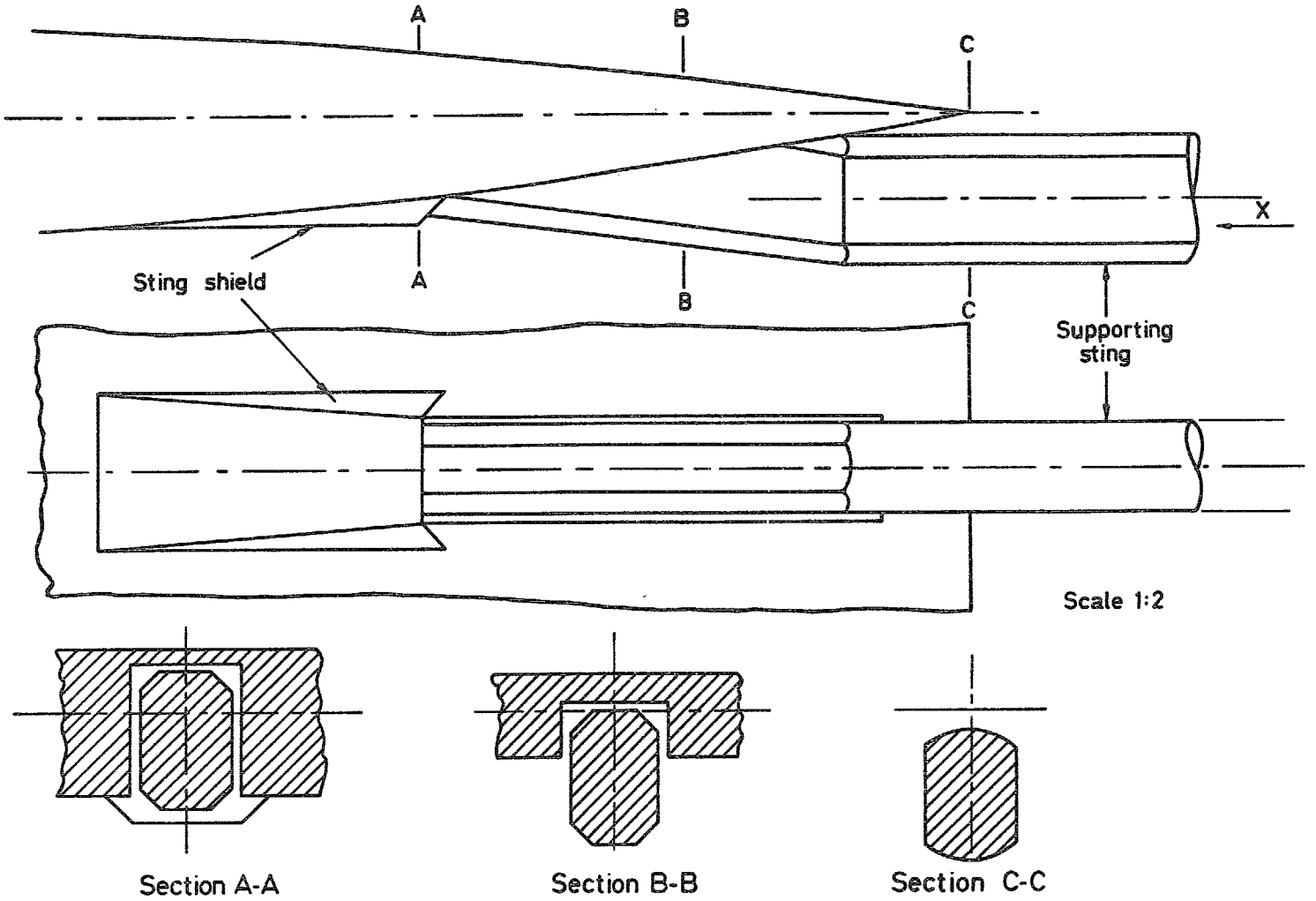

Fig 3 Modification of wing lower surface to accommodate supporting sting

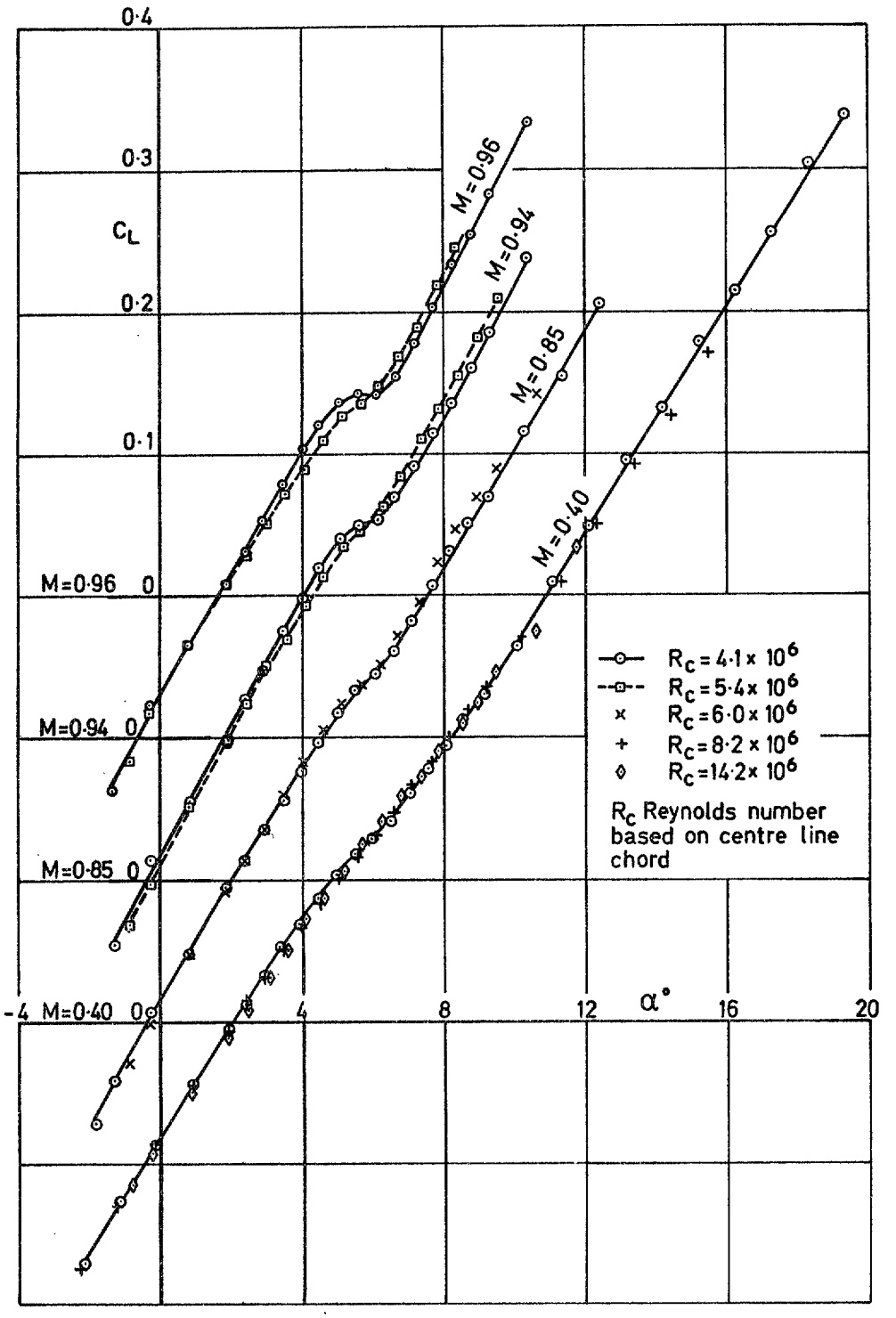

Fig 4 Effect of Reynolds number on the variation of C_L with incidence, transition free

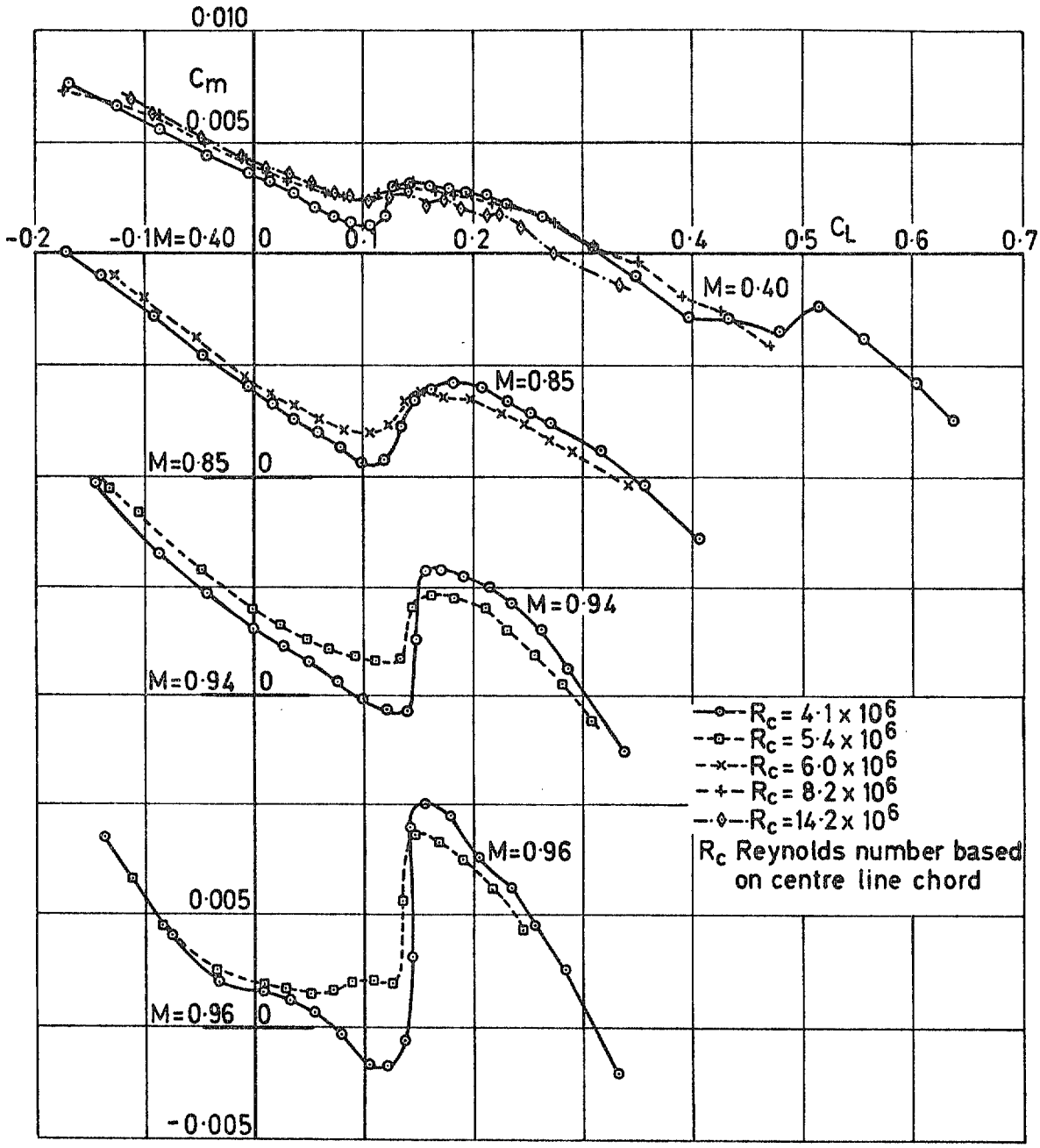

Fig 5 Effect of Reynolds number on the variation of C_m with C_L, transition free

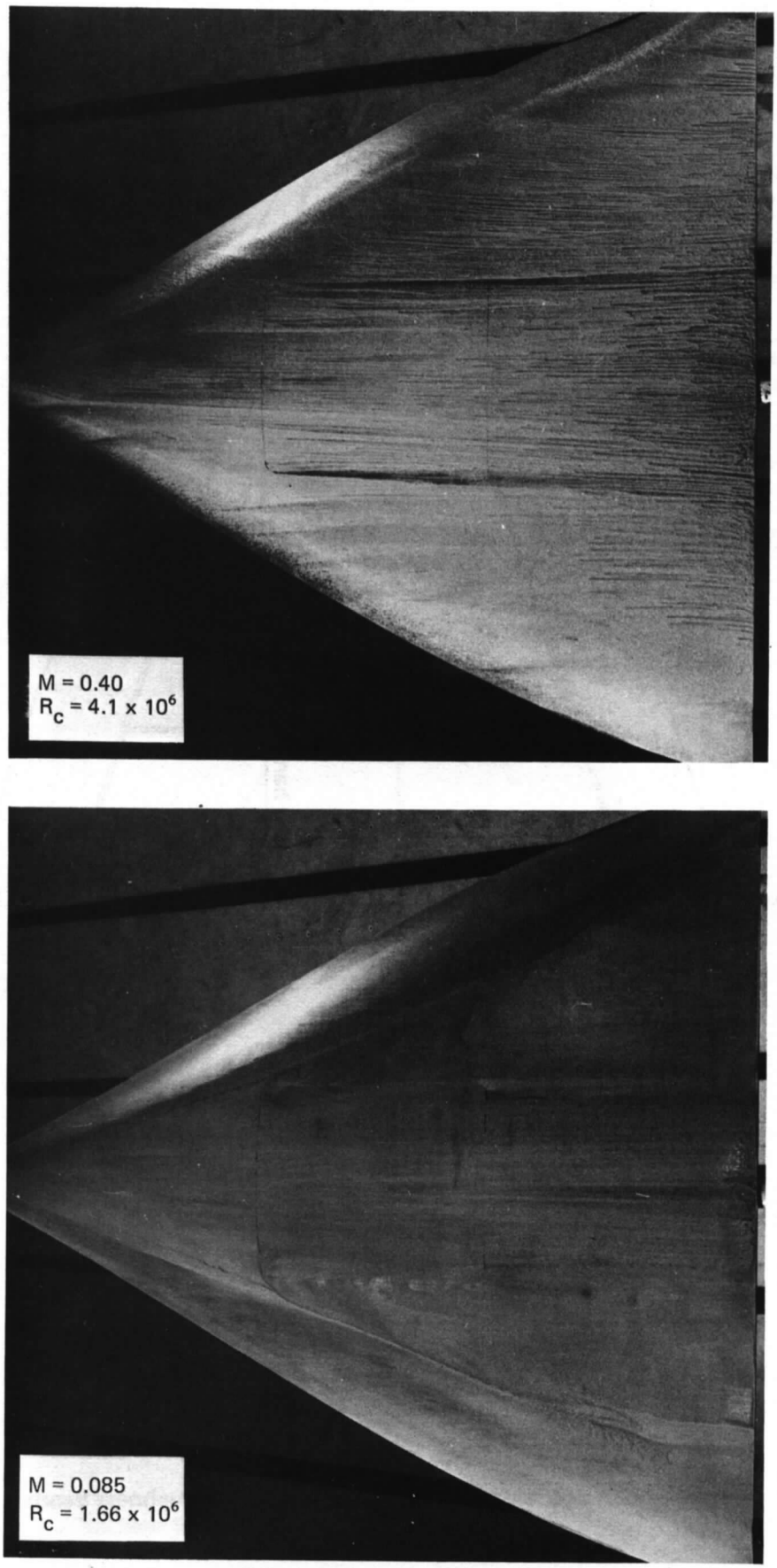

Fig 6 Transition free flow patterns. $\alpha = 5.32°$

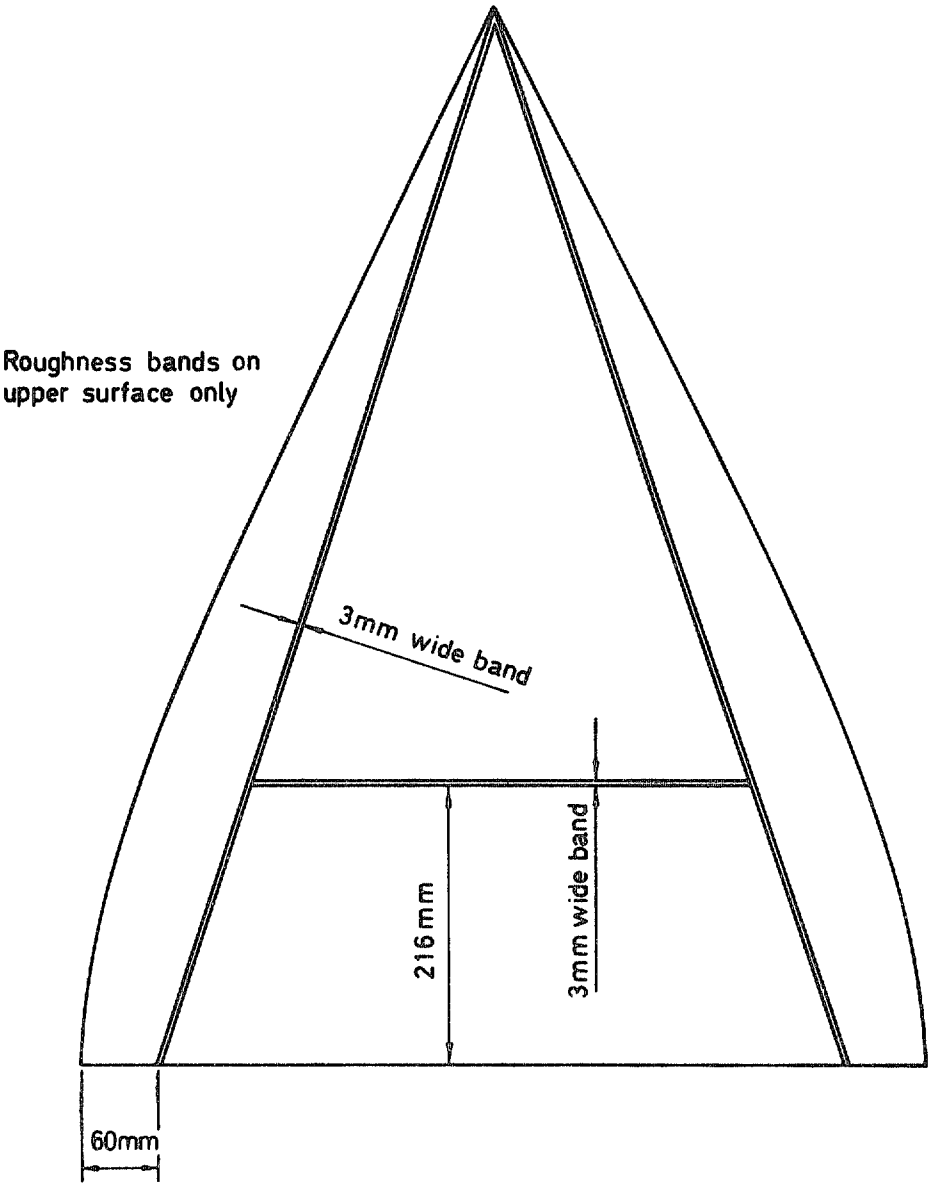

36 grade Ballotini 0·424 - 0·500 mm dia (rear band)
72 grade Ballotini 0·224 - 0·264 mm dia } alternative
85 grade Ballotini 0·178 - 0·211 mm dia } shoulder bands

Fig 7 Geometric details of shoulder and rear roughness bands

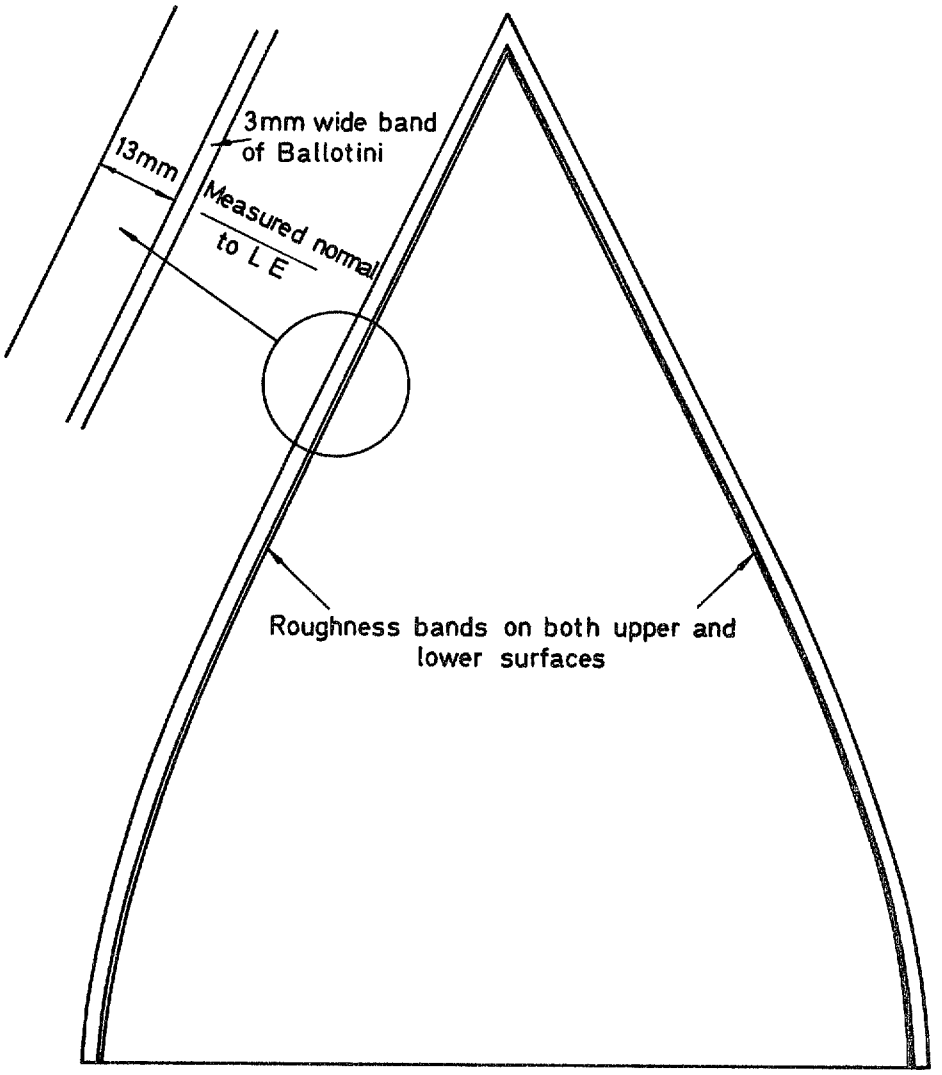

100 grade Ballotini 0·157 - 0·188mm dia
120 grade Ballotini 0·127 - 0·162mm dia

Fig 8 Geometric details of leading edge roughness bands

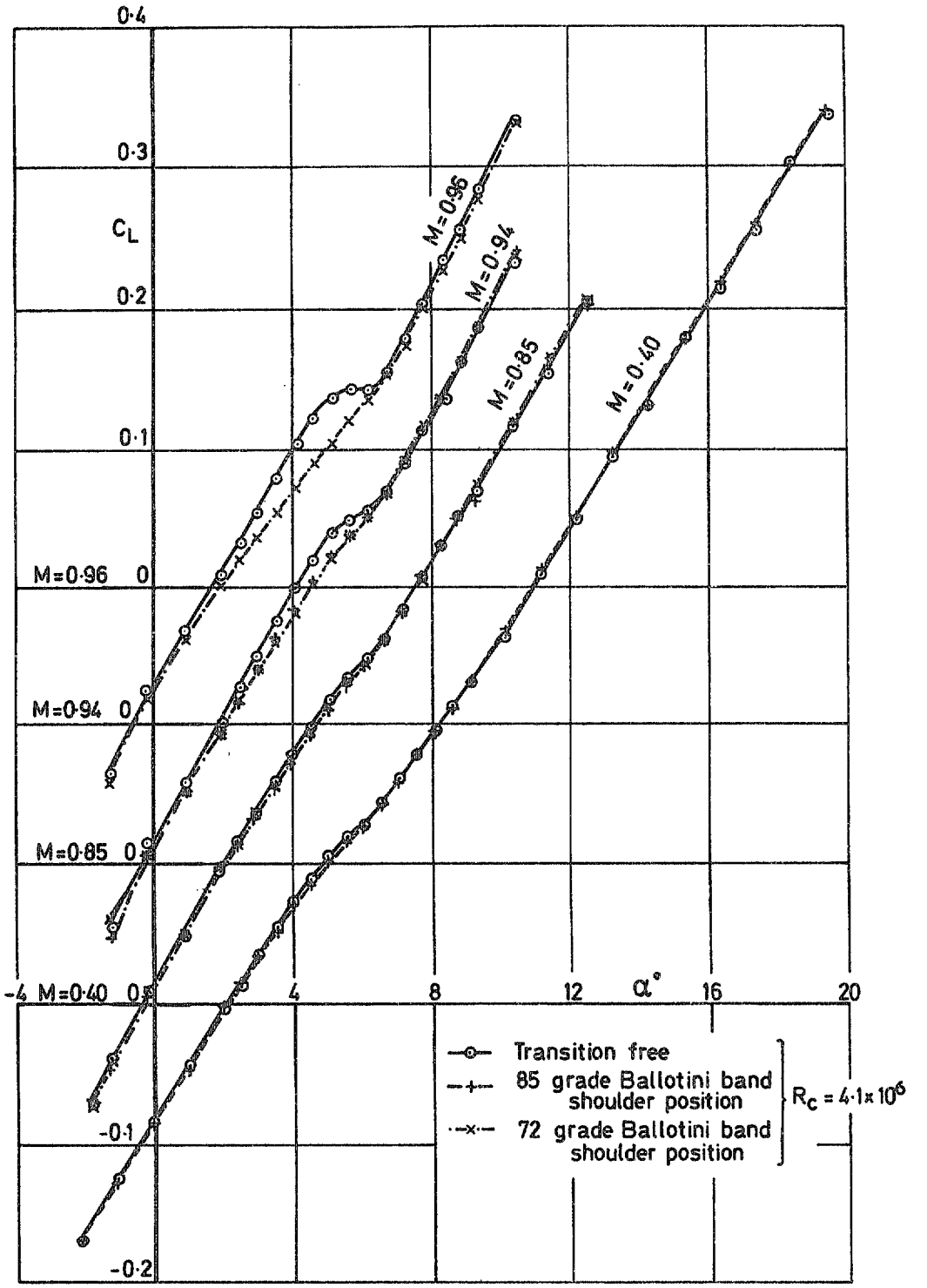

Fig 9 Effect of shoulder roughness bands on the variation of C_L with incidence

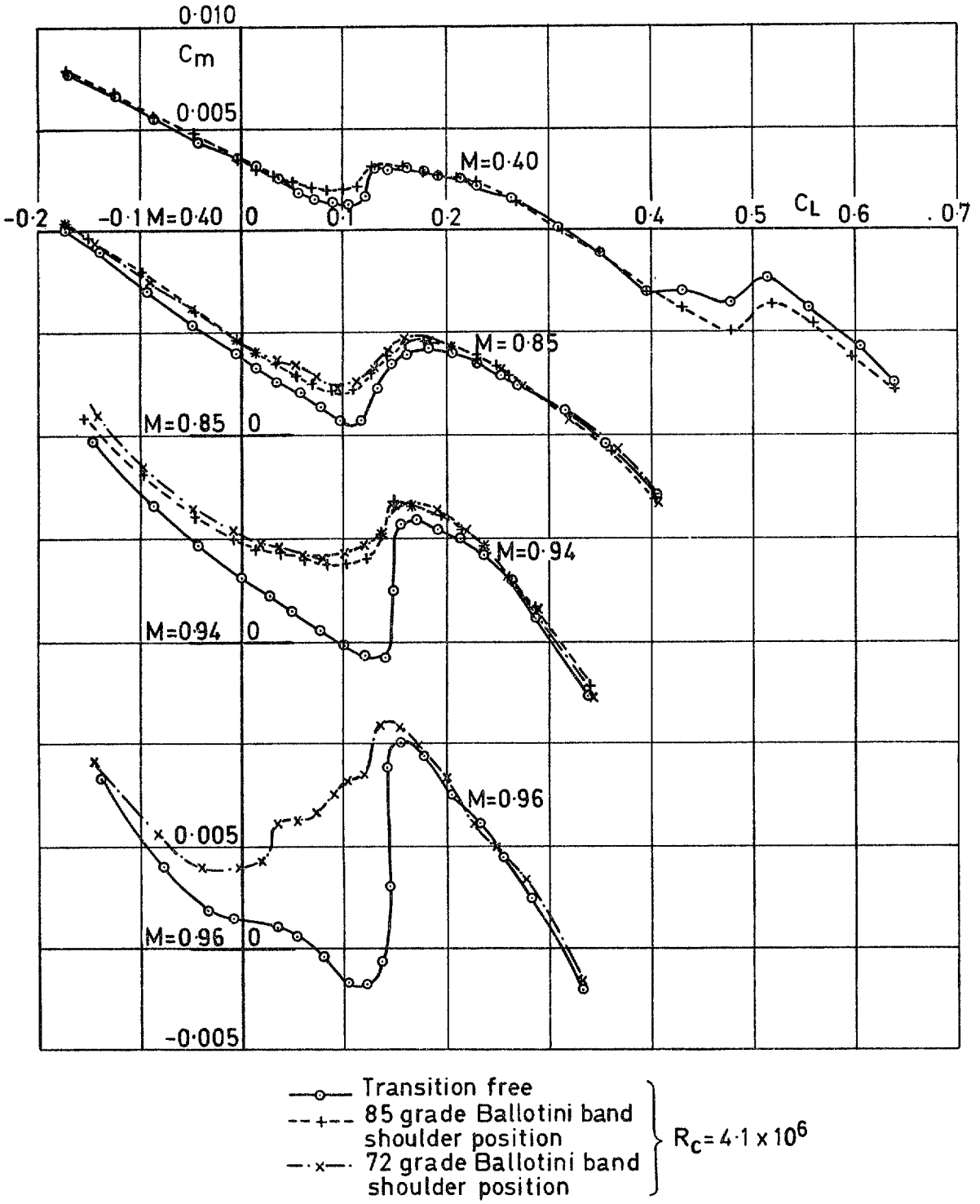

Fig 10 Effect of shoulder roughness bands on the variation of C_m with C_L

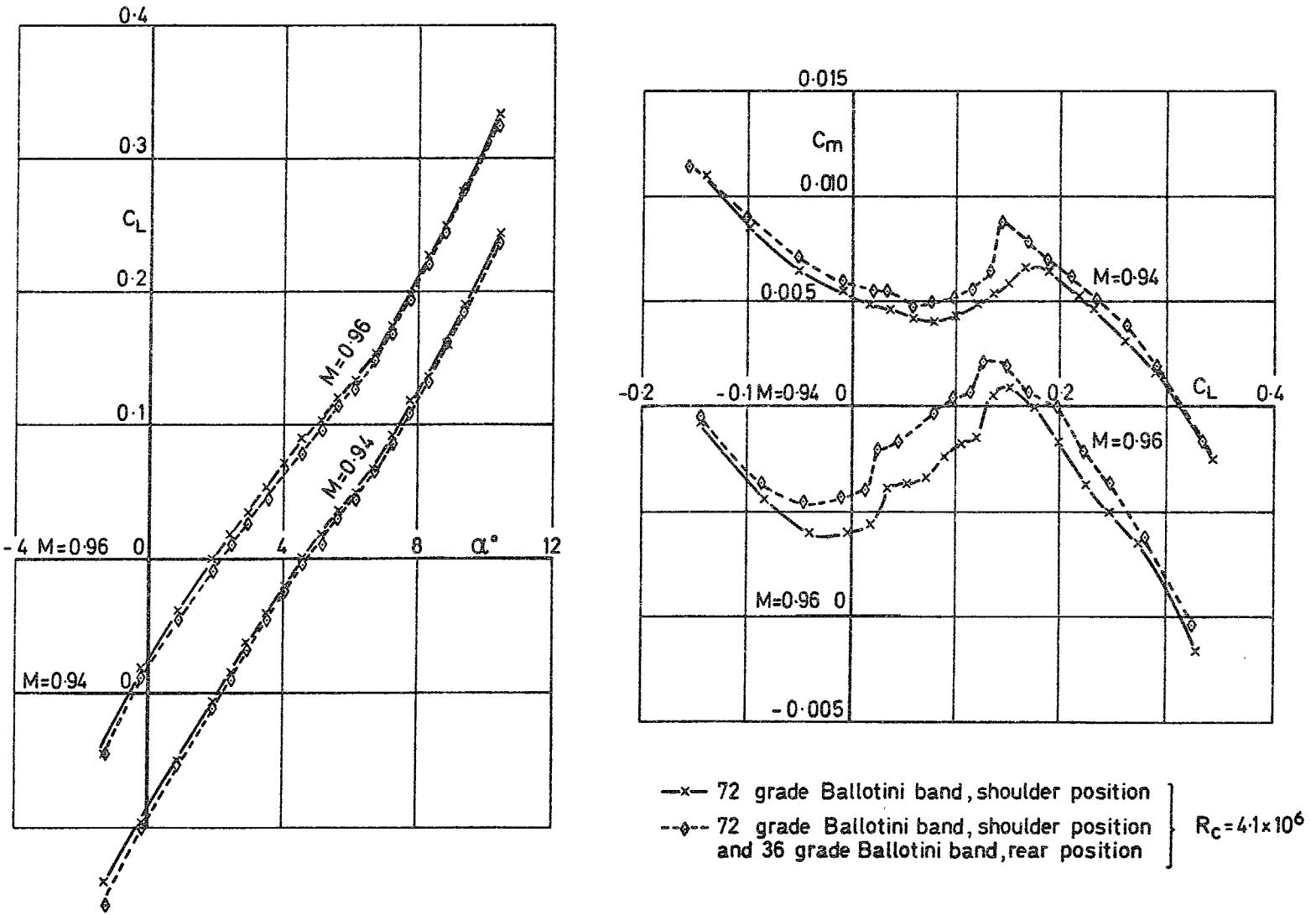

Fig 11 Effect of a roughness band in the rear position on lift and pitching moment at M = 0.94 and M = 0.96

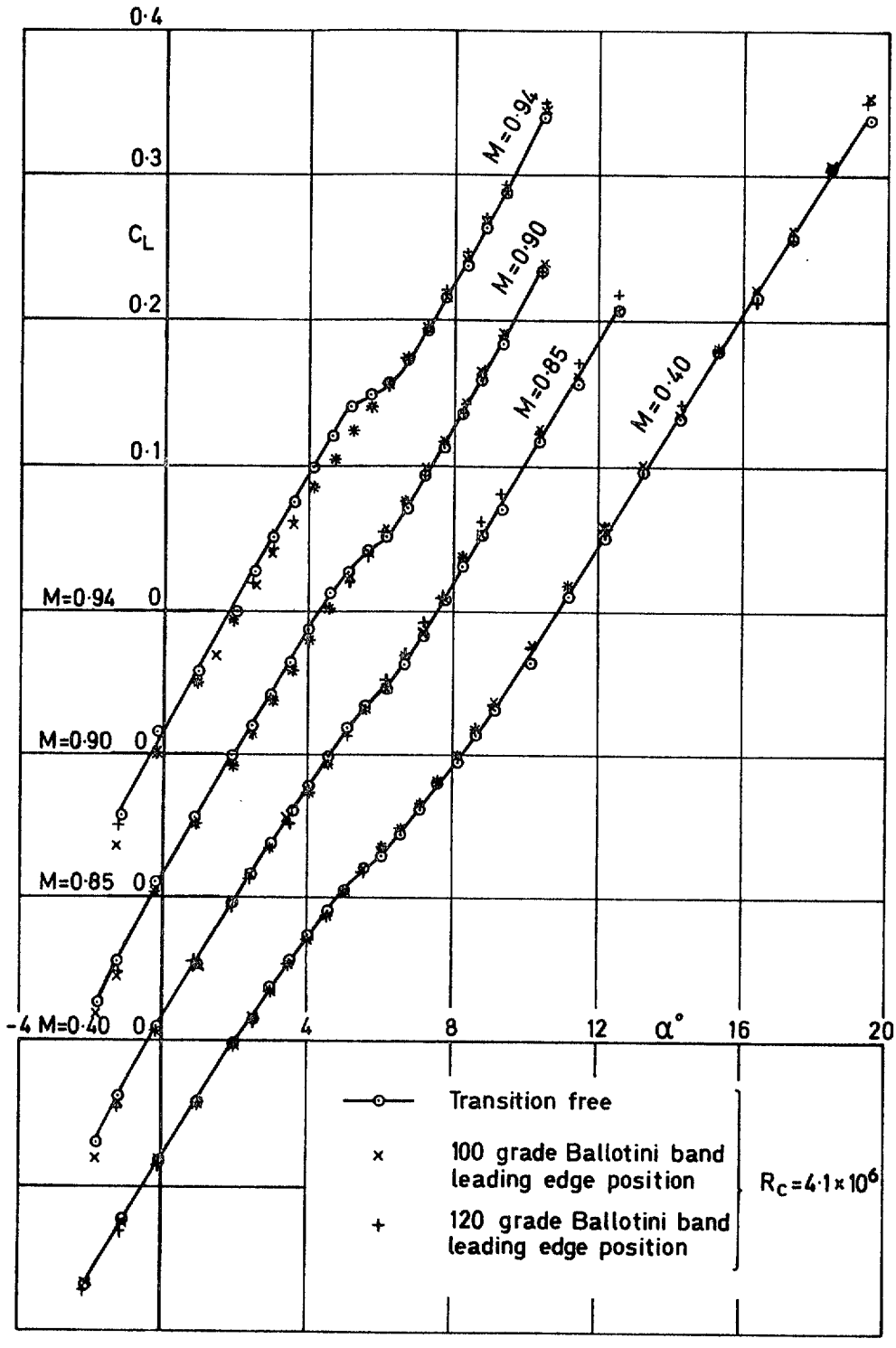

Fig 12 Effect of leading edge roughness bands on the variation of C_L with incidence, M = 0.40 to 0.94

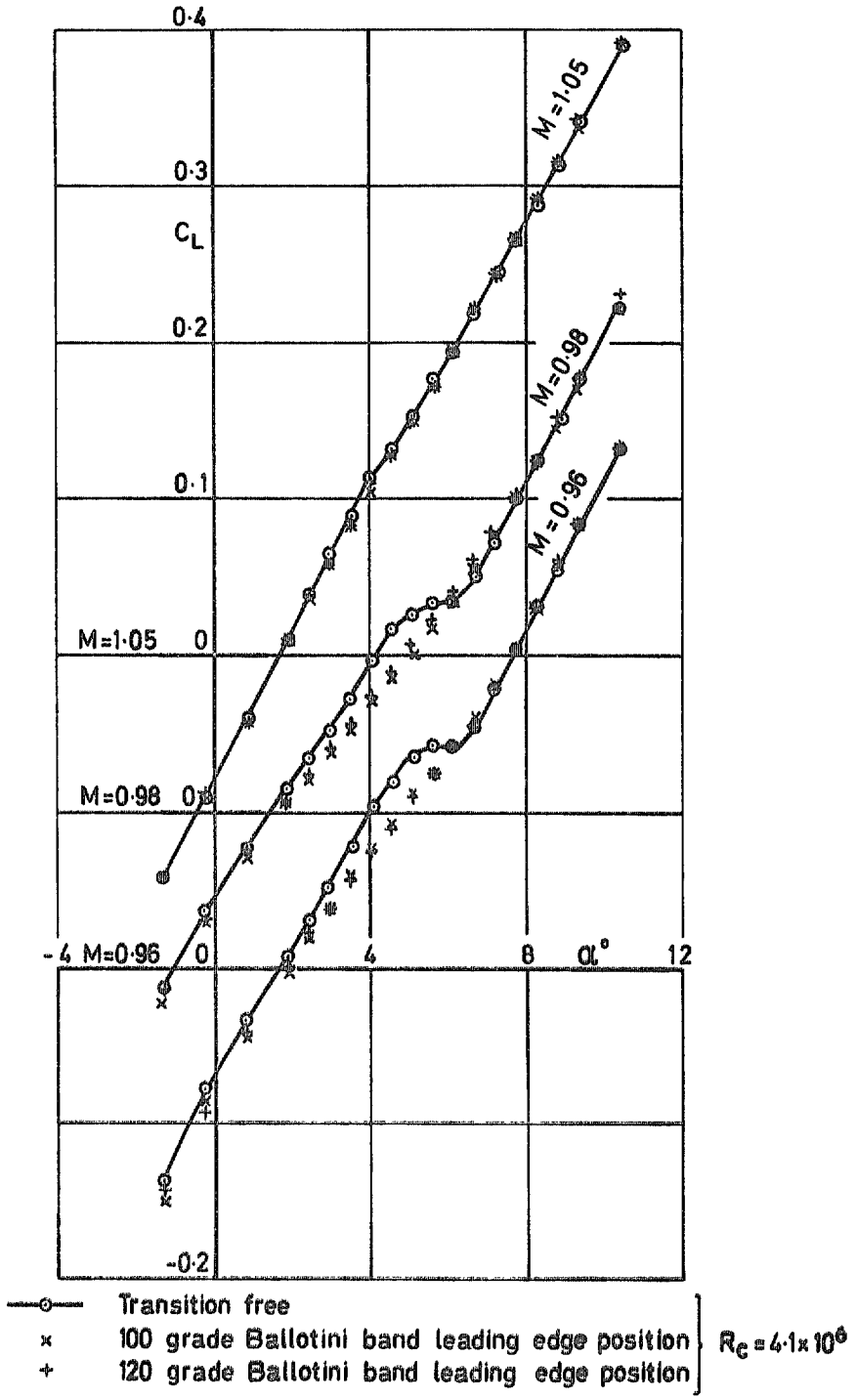

Fig 13 Effect of leading edge roughness bands on the variation of C_L with incidence, M = 0.96 to 1.05

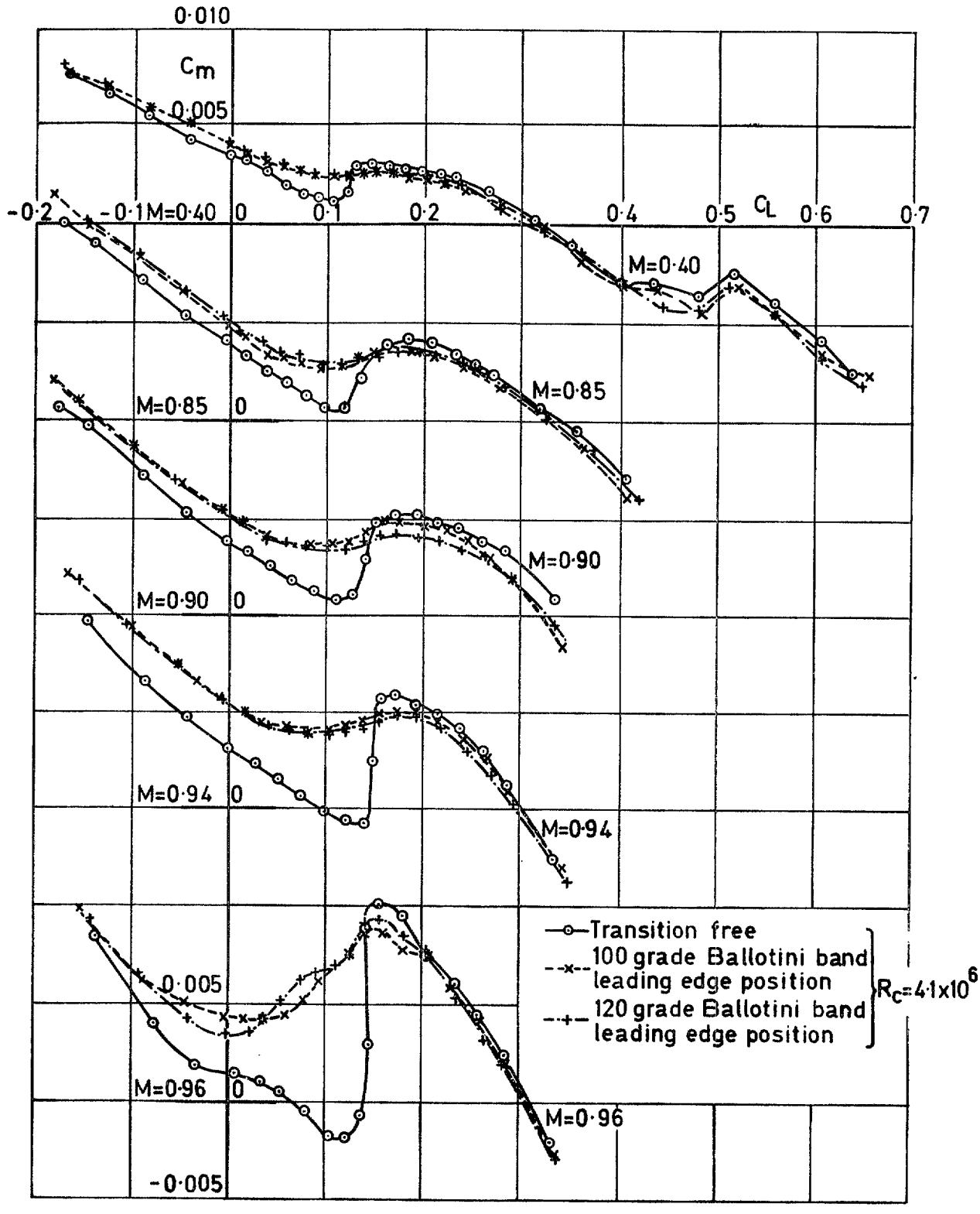

Fig 14 Effect of leading edge roughness bands on the variation of C_m with C_L, M = 0.40 to 0.96

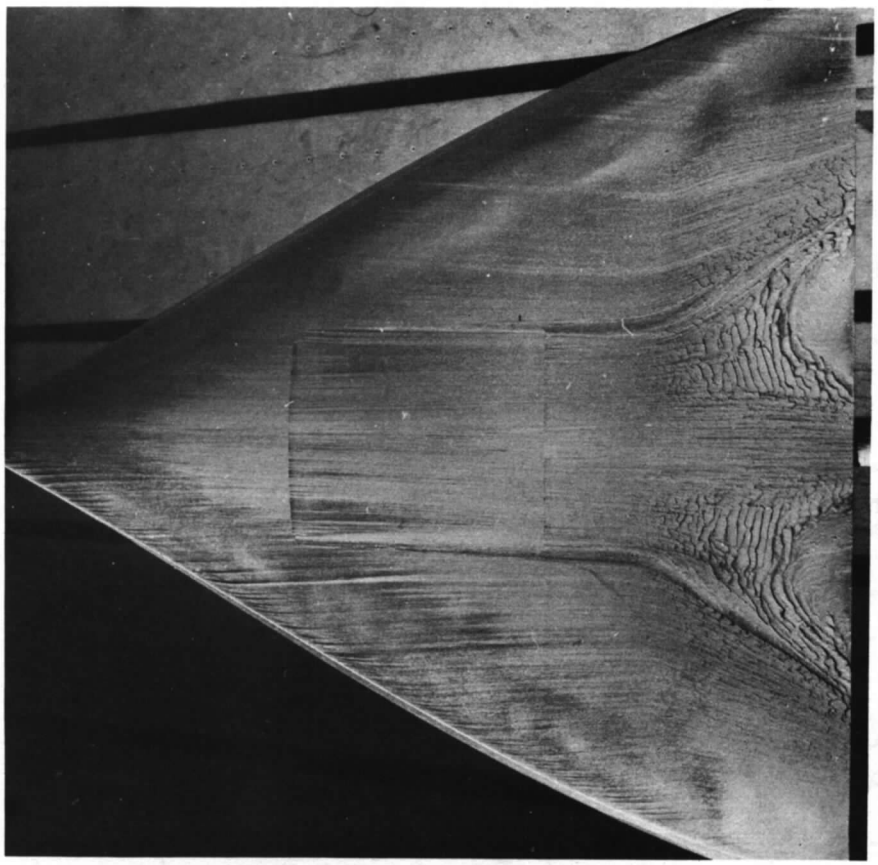

100 grade ballotini
leading edge bands
$C_L = 0.0760$
$C_m = 0.00614$
(mean values measured
during flow visualization
run)
From Fig 14 at
$C_L = 0.076$, $C_m = 0.0051$)

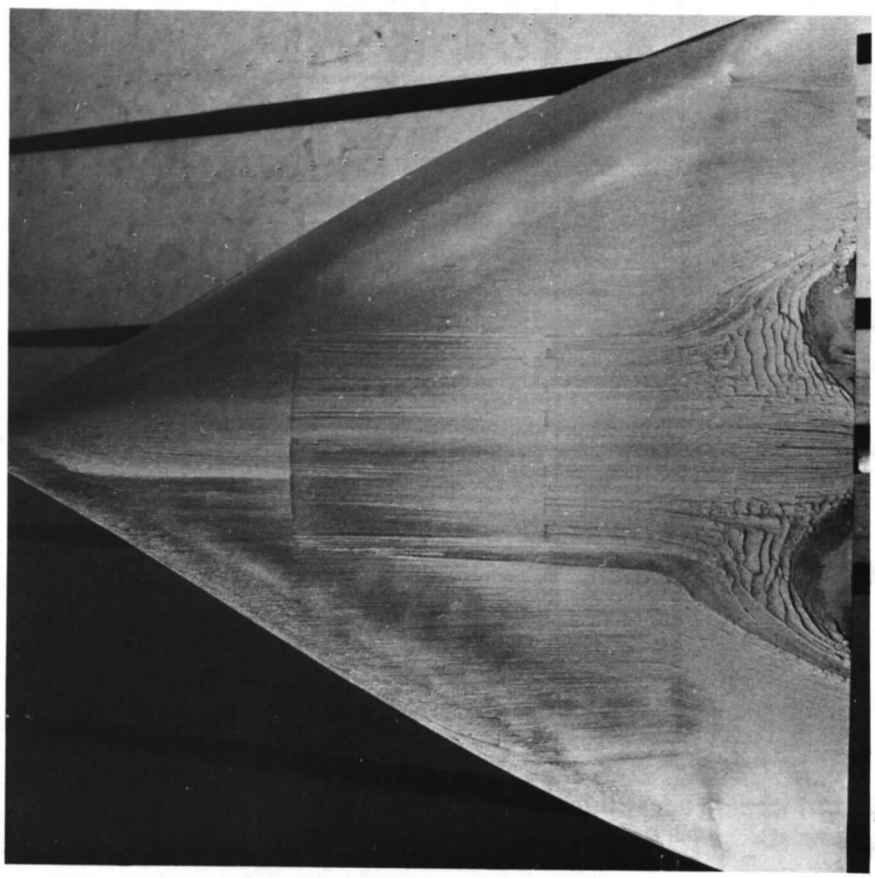

Leading edge roughness
bands removed
$C_L = 0.0782$
$C_m = 0.00523$
(mean values measured
during flow visualization
run)
From Fig 14 at
$C_L = 0.078$, $C_m = -0.0004$

Fig 15 Flow patterns at M = 0.96, $\alpha = 4.2°$, $R_c = 4.1 \times 10^6$ with and without leading edge roughness bands

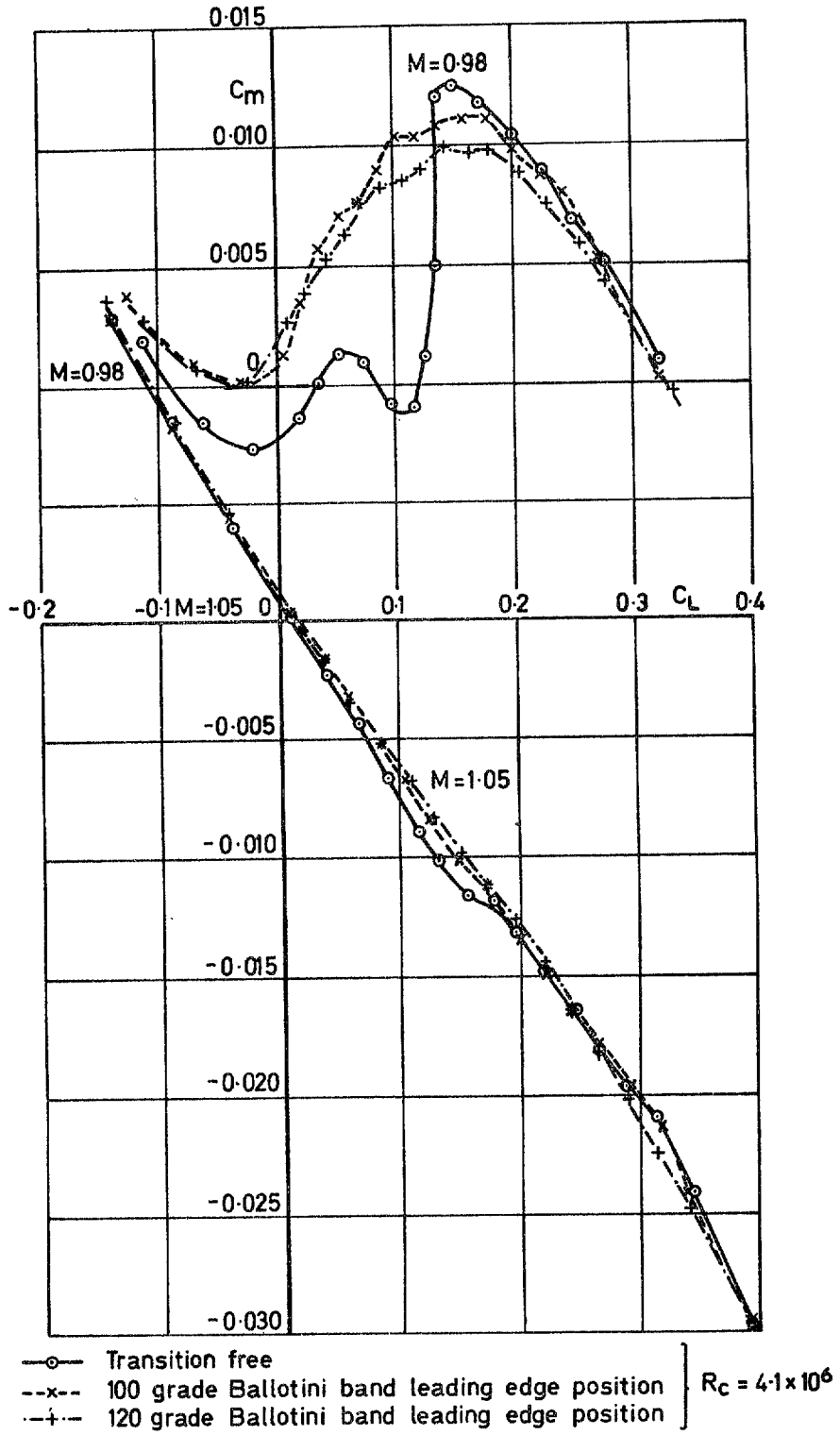

Fig 16 Effect of leading edge roughness bands on the variation of C_m with C_L, M = 0.98 and 1.05

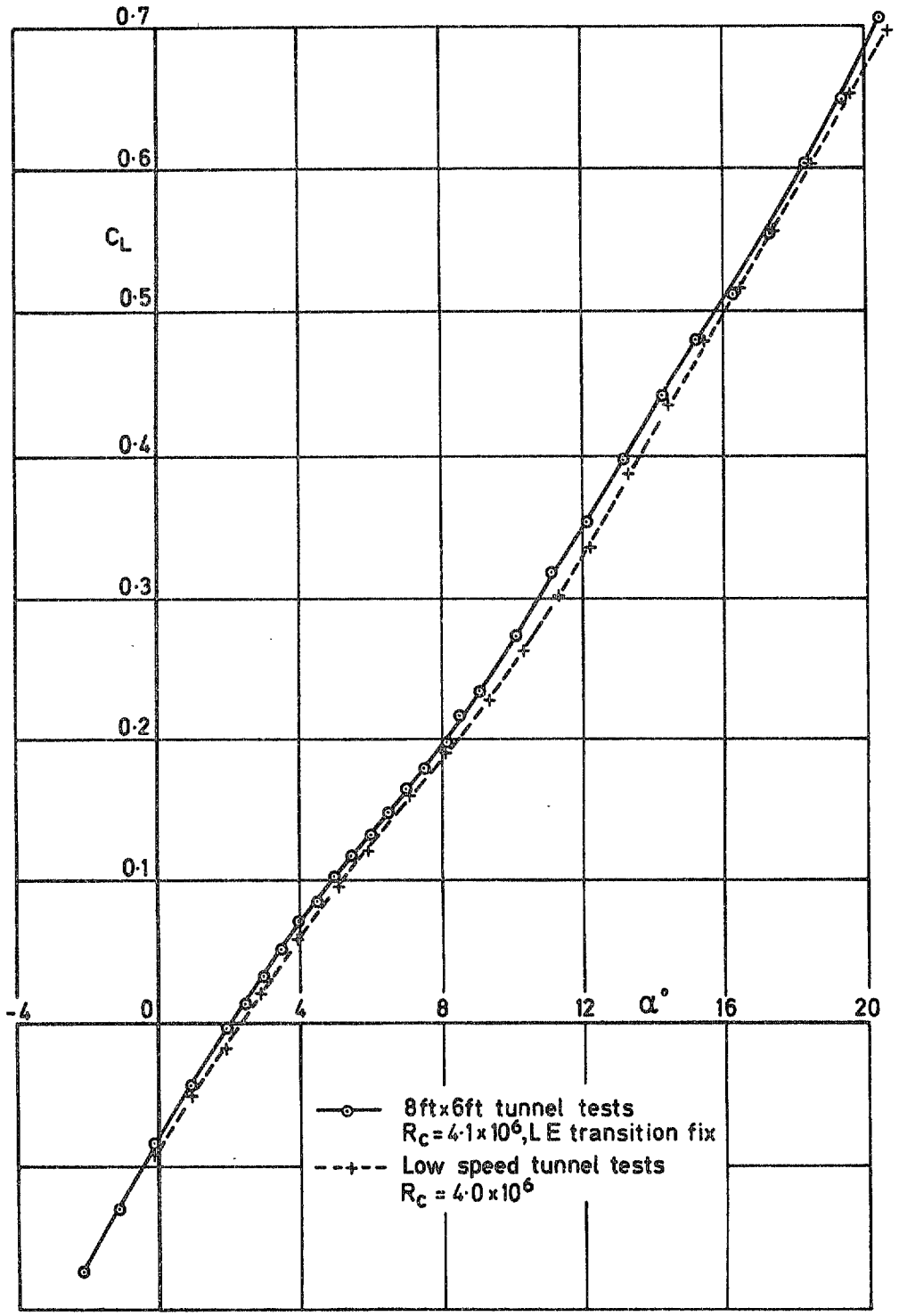

Fig 17 Variation of C_L with incidence, low speed measurements compared with 8ft x 6ft tunnel results at M = 0.4

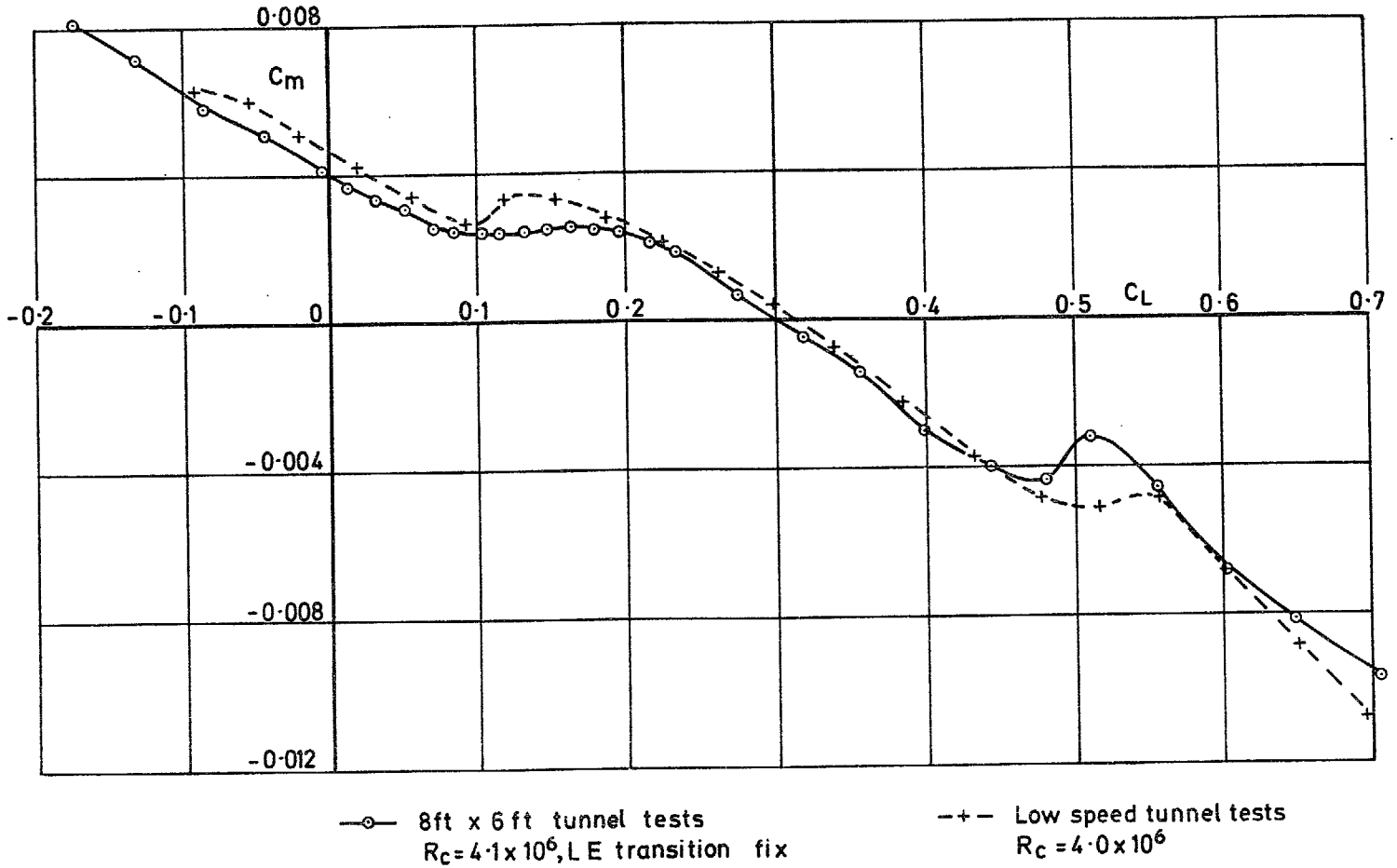

Fig 18 Variation of C_m with C_L, low speed measurements compared with 8ft x 6ft tunnel results at M = 0.4

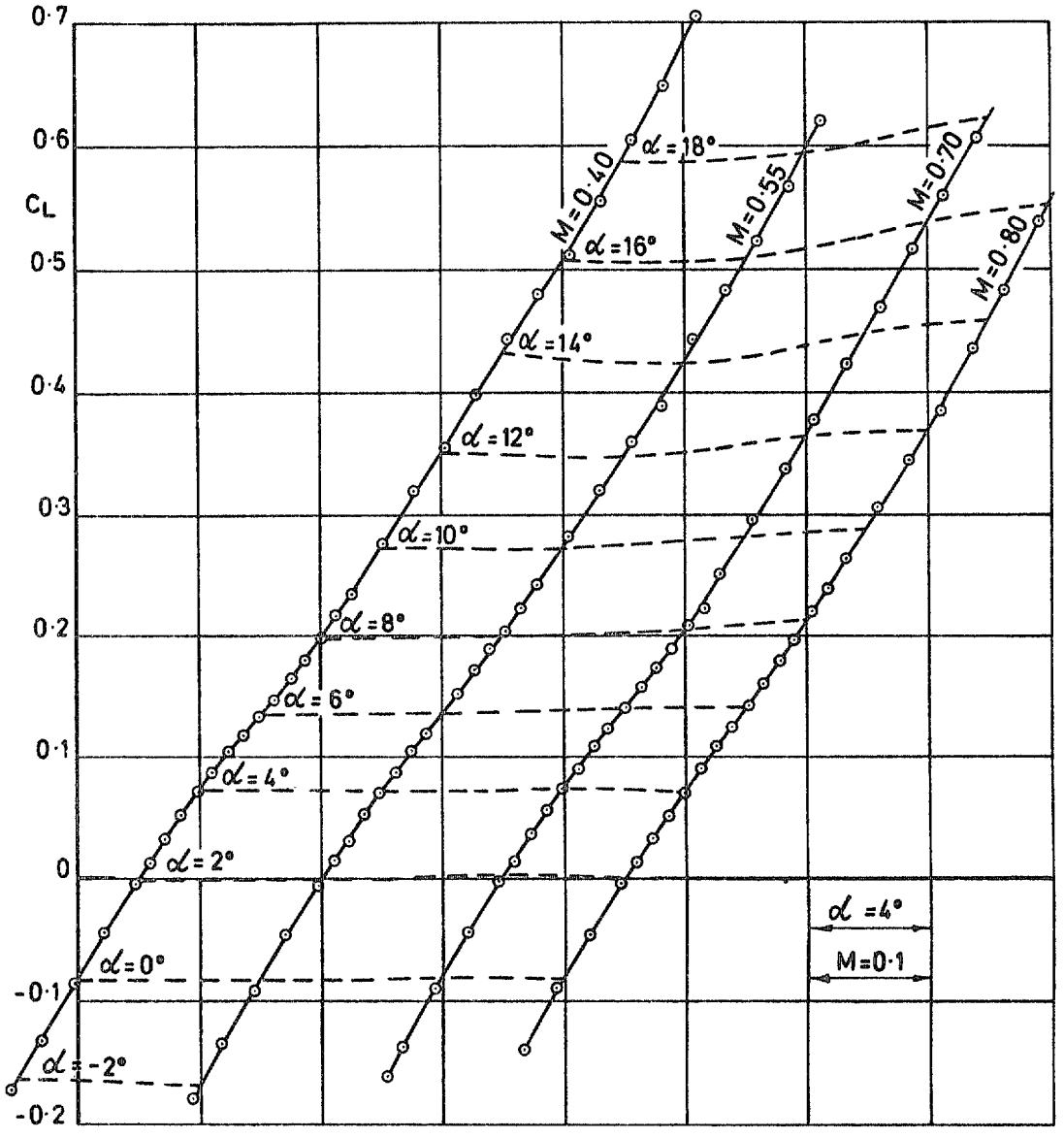

120 grade Ballotini bands, leading edge position, $R_c = 4{\cdot}1 \times 10^6$

Fig 19 Lift carpet, M = 0.40 to 0.80

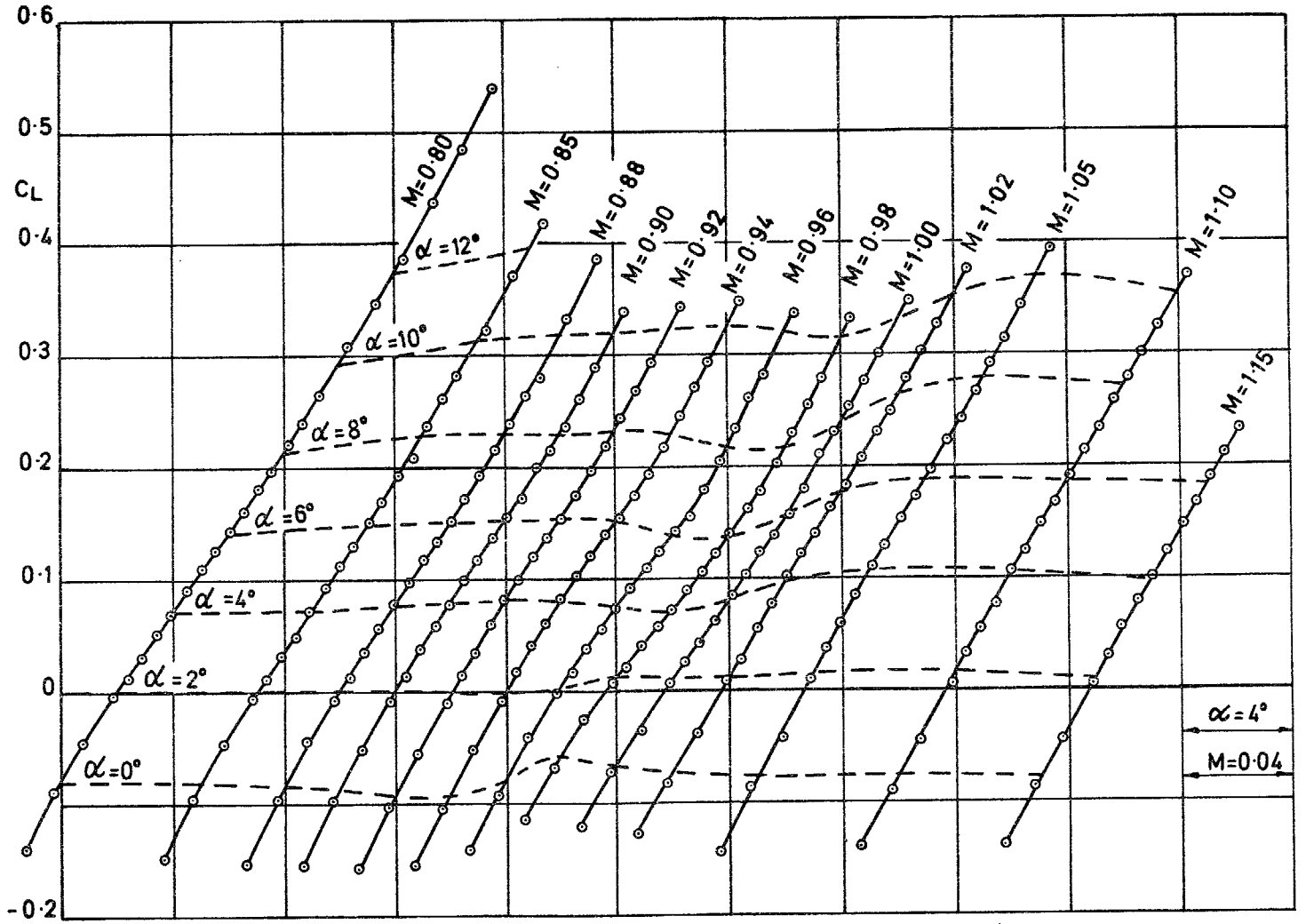

Fig 20 Lift carpet, M = 0.80 to 1.15

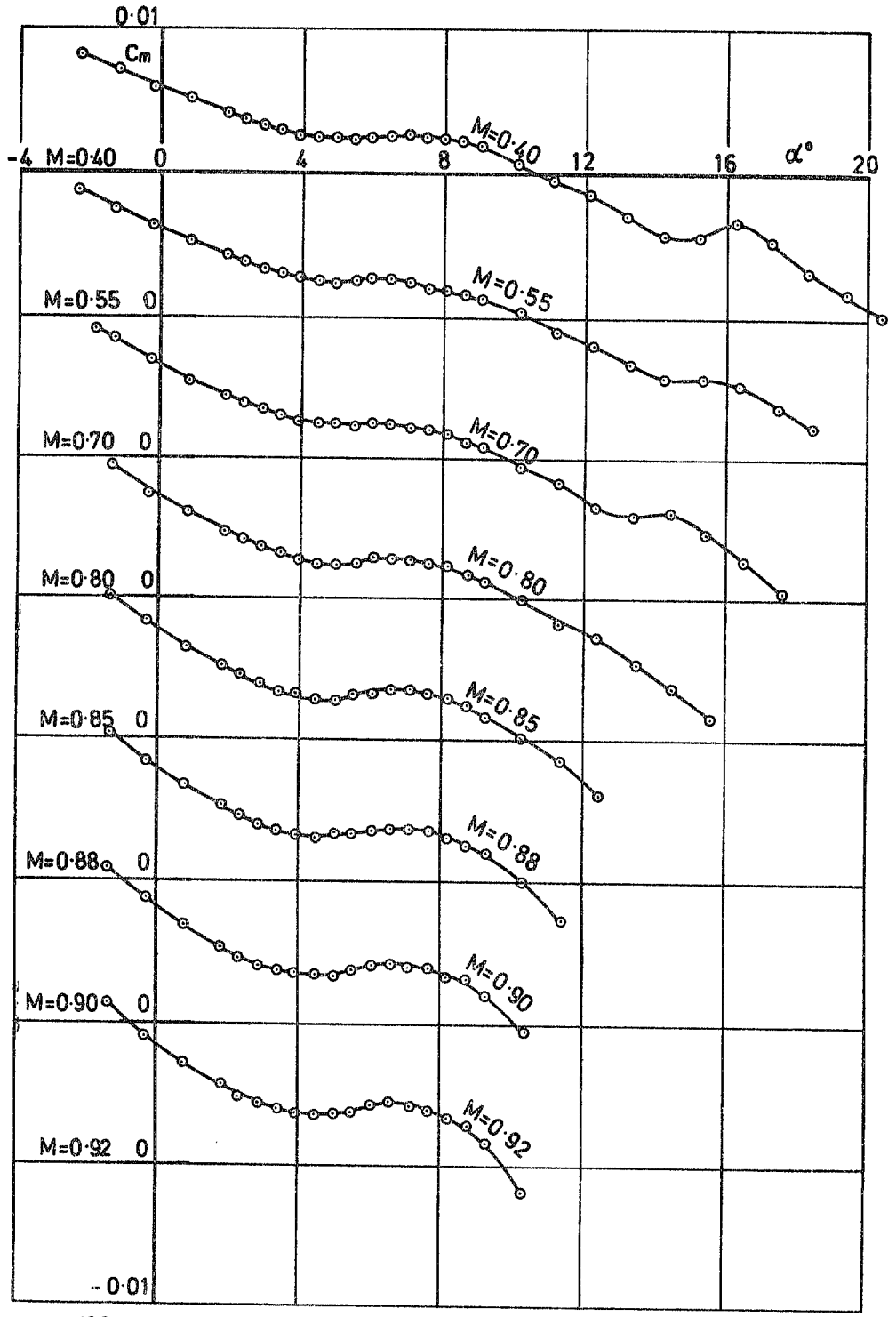

120 grade Ballotini bands, leading edge position, $R_c = 4{\cdot}1 \times 10^6$

Fig 21 Variation of C_m with incidence, M = 0.40 to 0.92

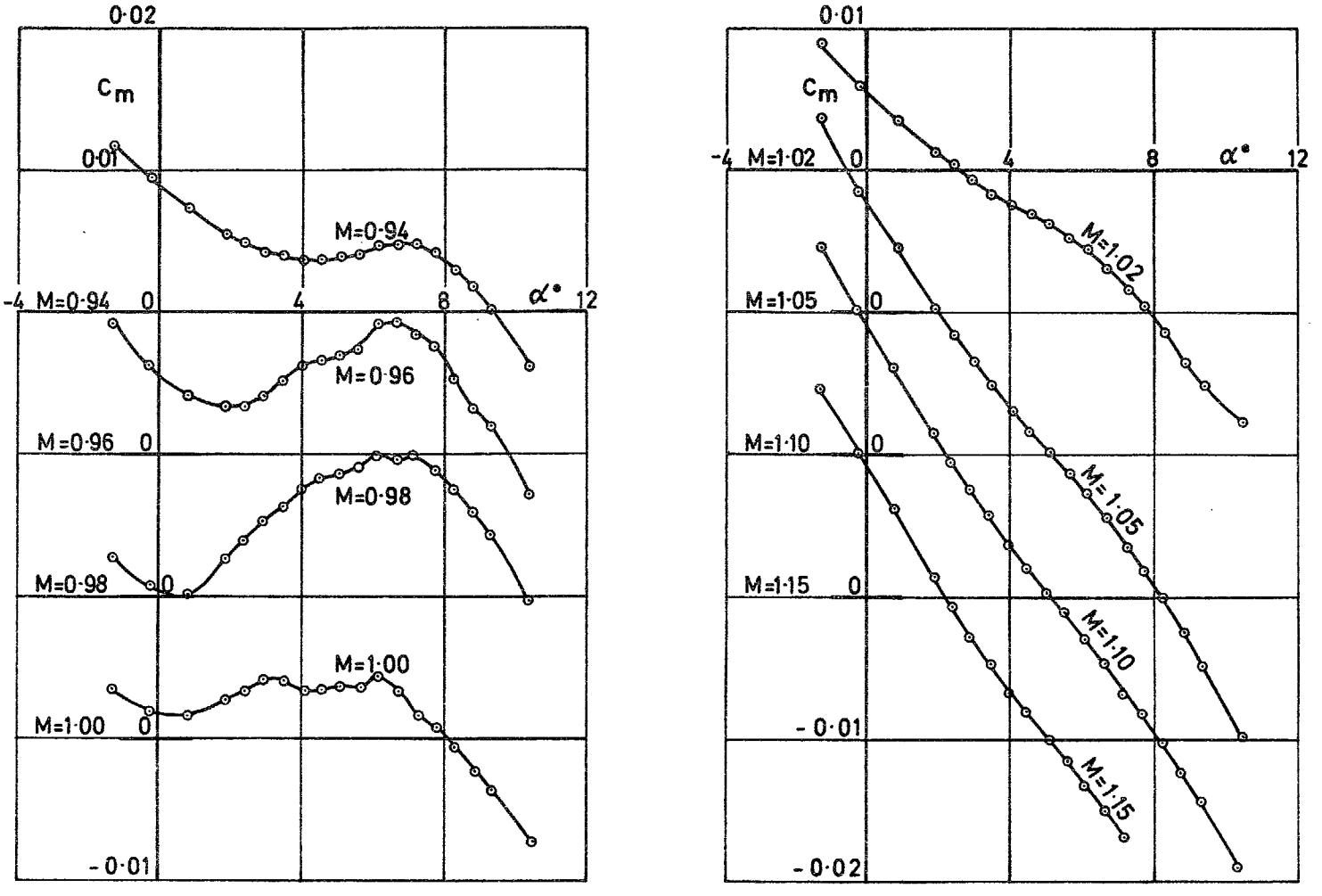

120 grade Ballotini bands, leading edge position, $R_c = 4{\cdot}1 \times 10^6$

Fig 22 Variation of C_m with incidence, M = 0.94 to 1.15

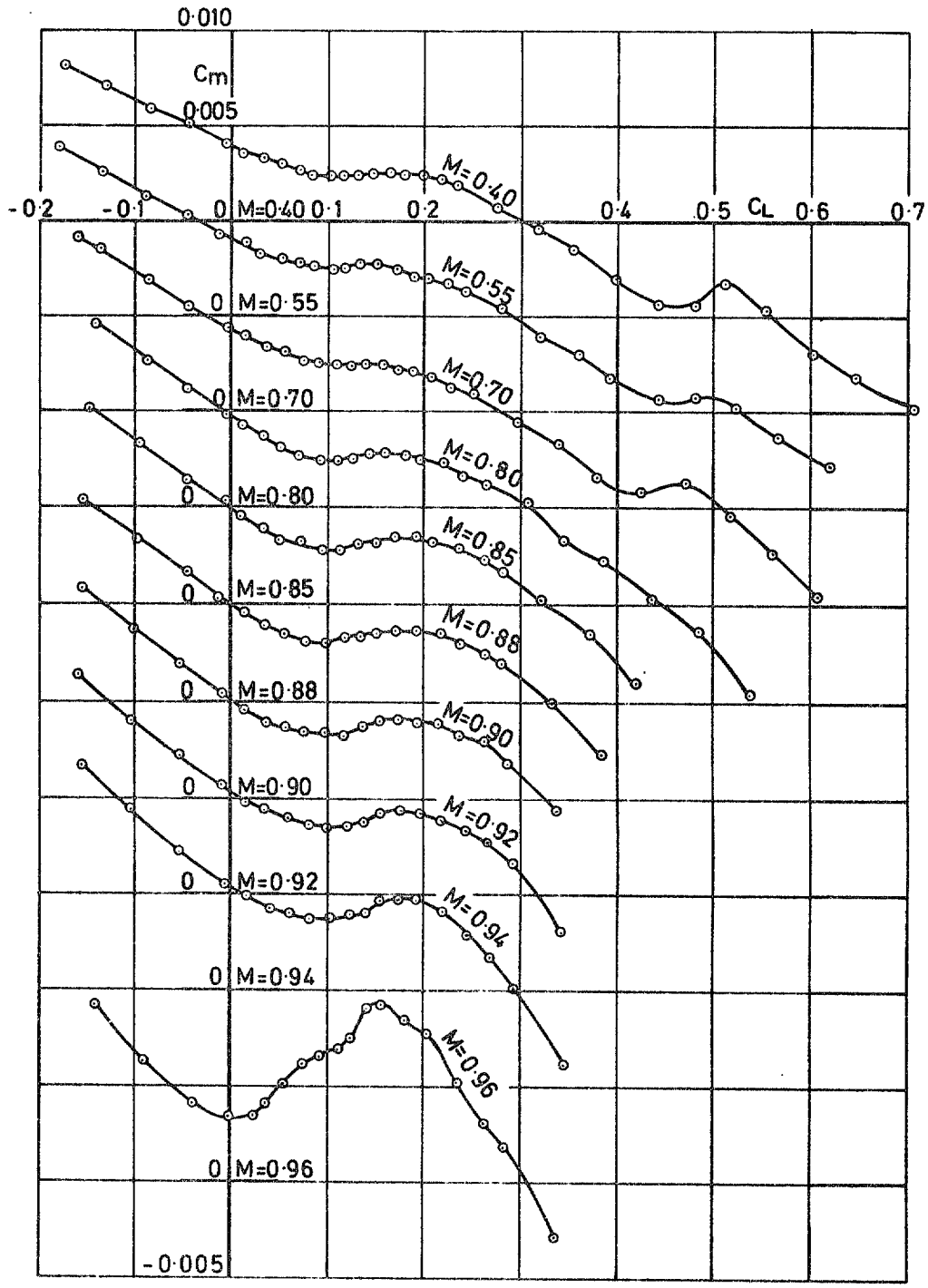

120 grade Ballotini bands, leading edge position, $R_c = 4{\cdot}1 \times 10^6$

Fig 23 Variation of C_m with C_L, M = 0.40 to 0.96

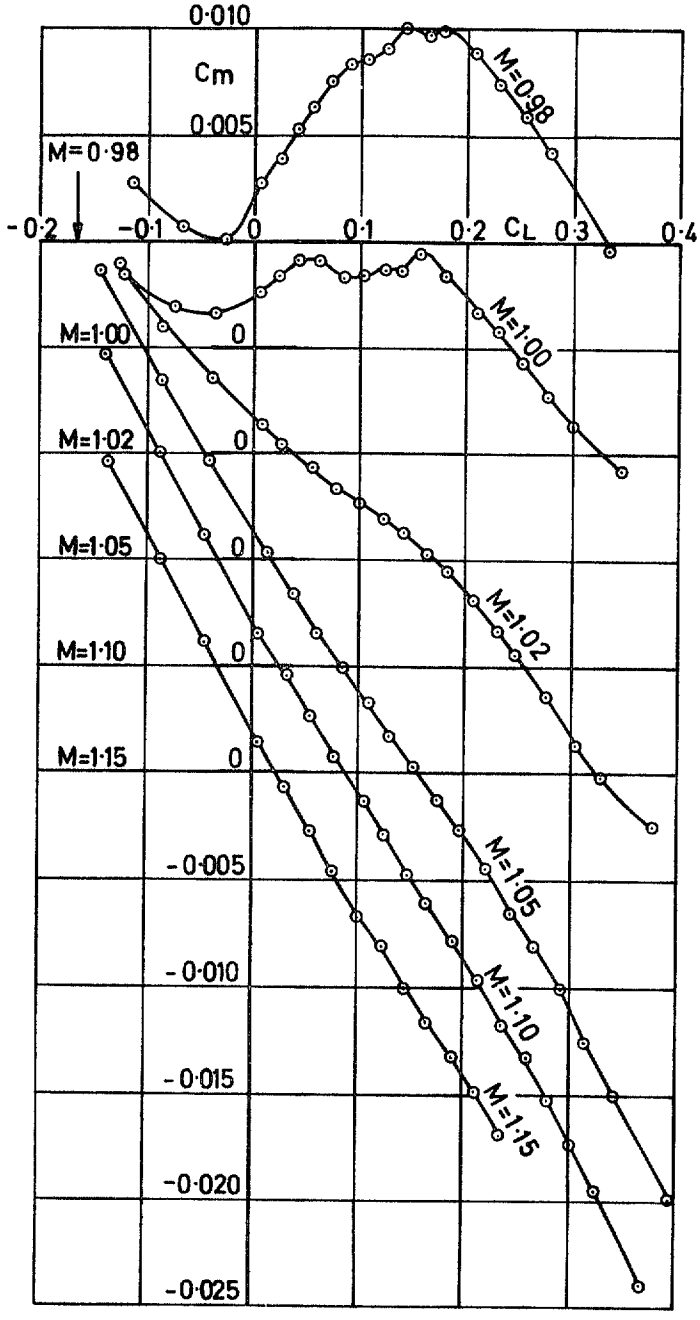

120 grade Ballotini bands , leading edge position, $R_c = 4{\cdot}1 \times 10^6$

Fig 24 Variation of C_m with C_L , M = 0.98 to 1.15

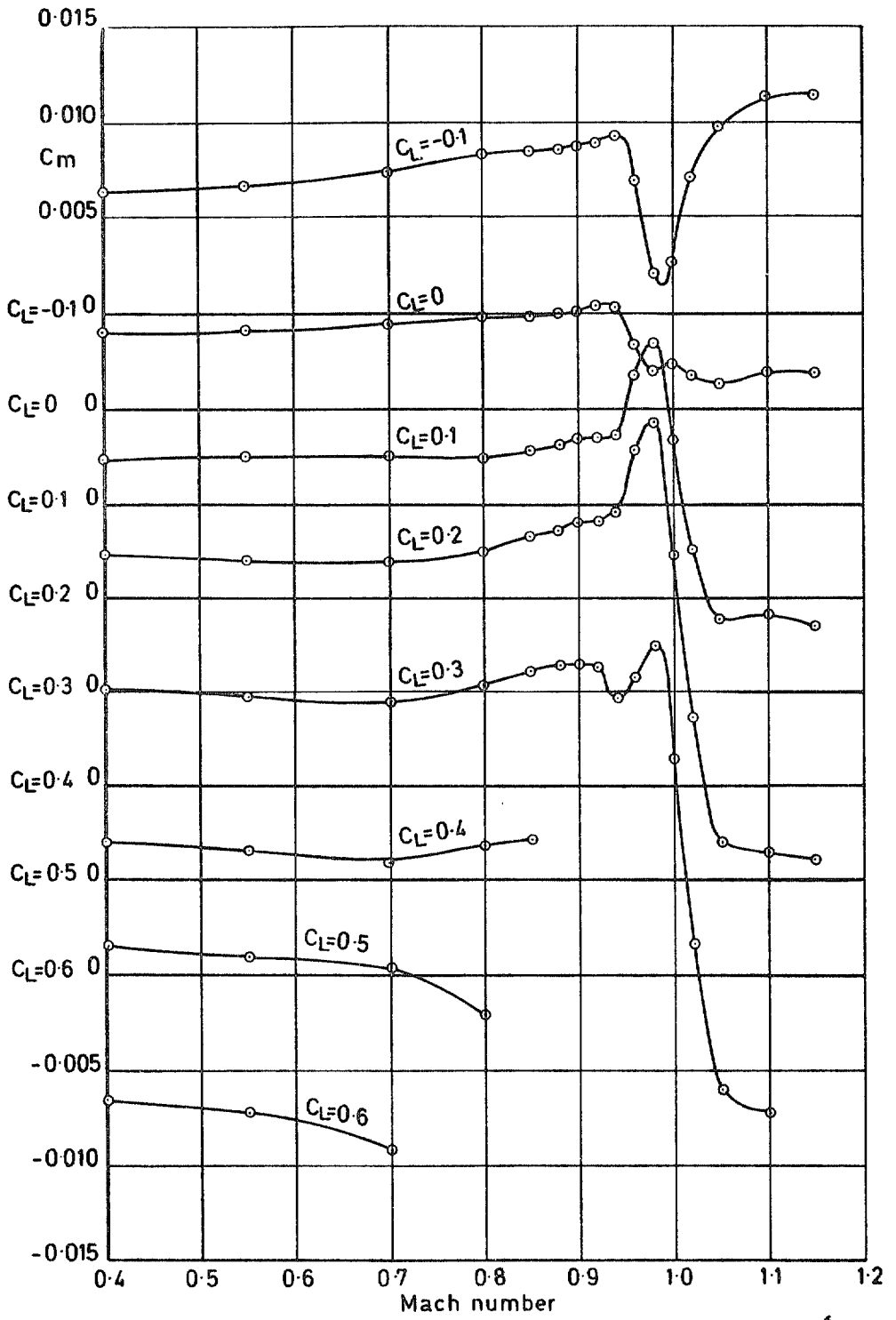

Fig 25 Variation of C_m with Mach number, at constant C_L

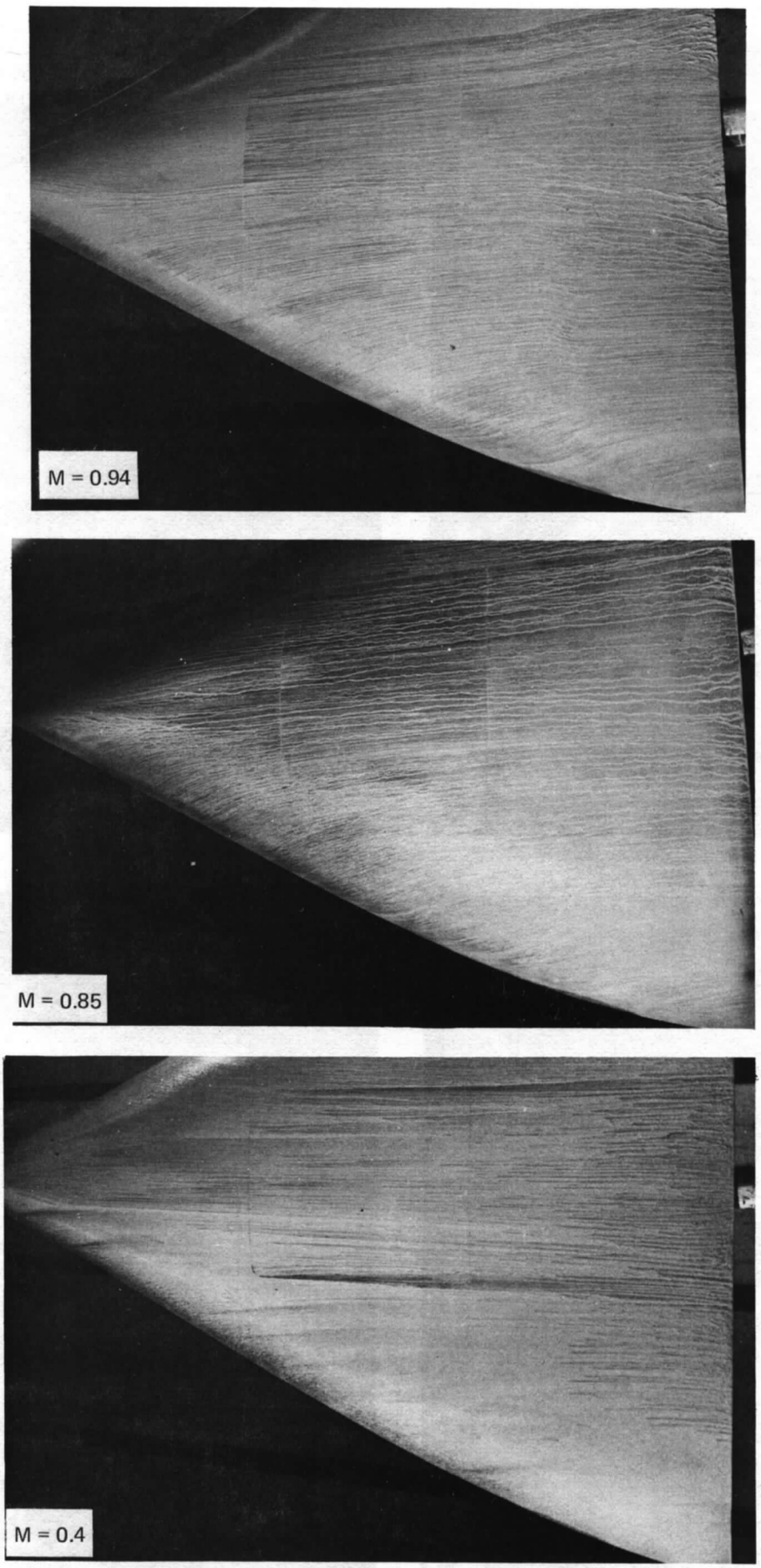

Fig 26 Flow patterns at the design incidence $\alpha_{nom} = 5.32°$ transition free, $R_c = 4.1 \times 10^6$

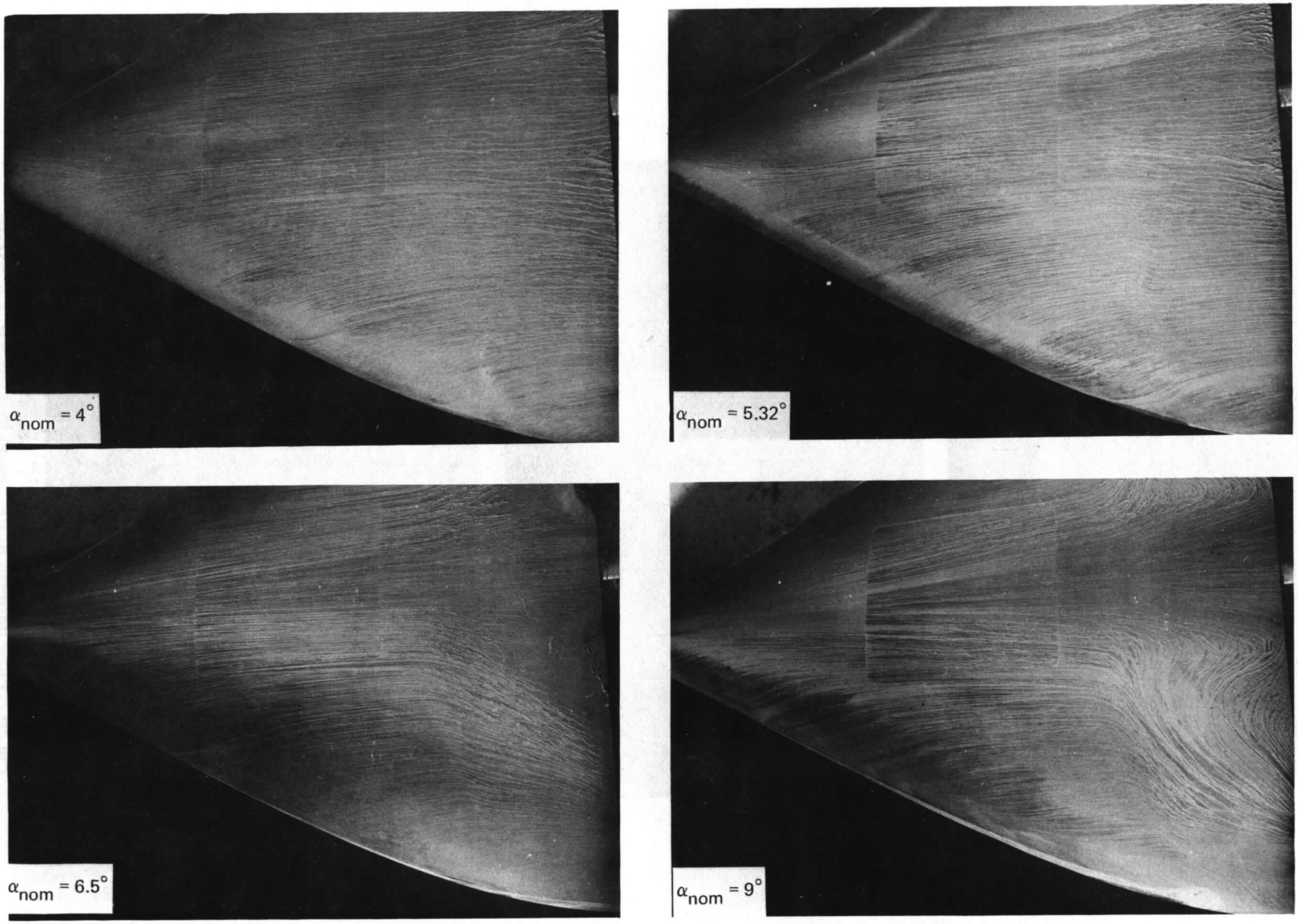

Fig 27 Flow patterns at M = 0.94 transition free, $R_c = 4.1 \times 10^6$

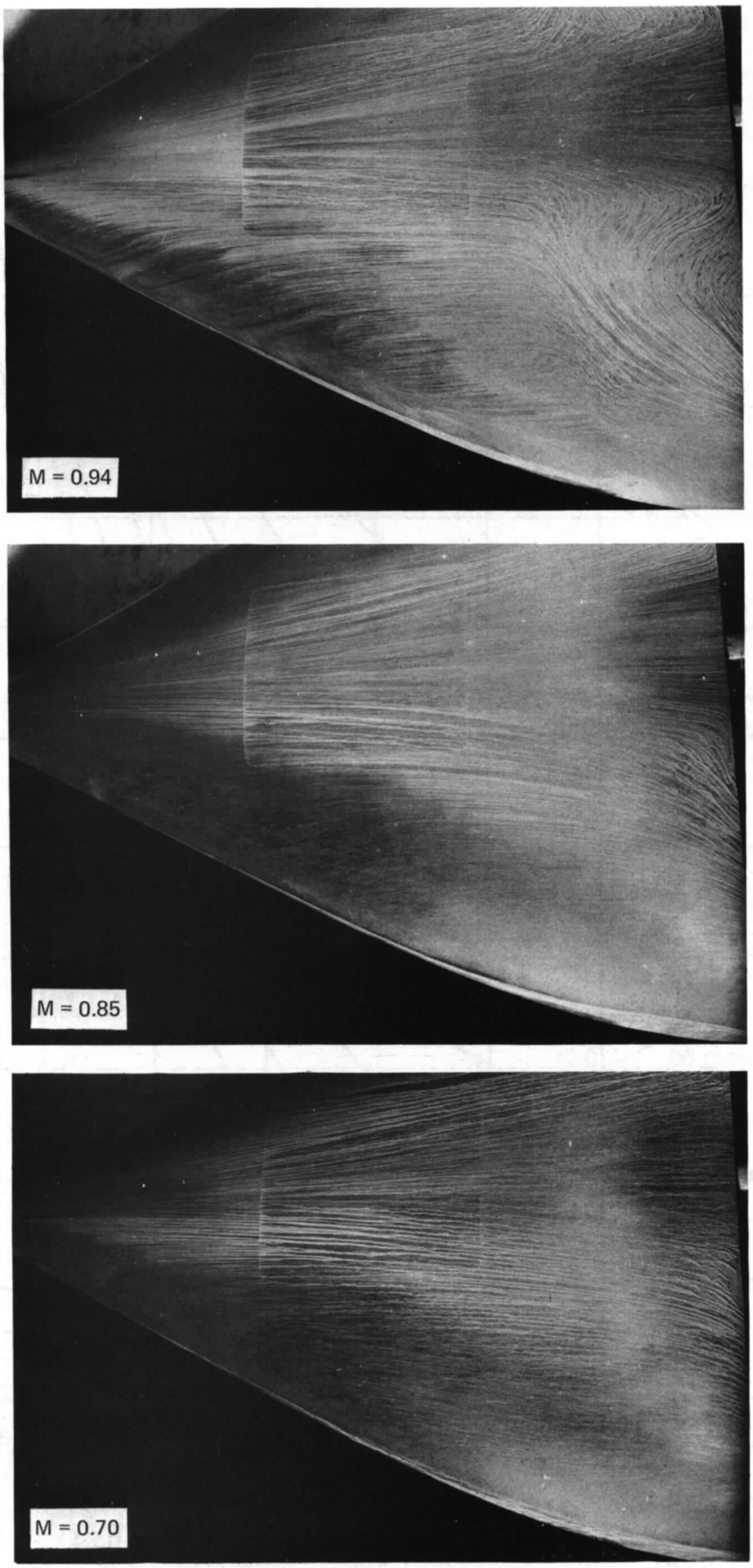

Fig 28 Flow patterns at $\alpha_{nom} = 9^{\circ}$ transition free, $R_c = 4.1 \times 10^6$

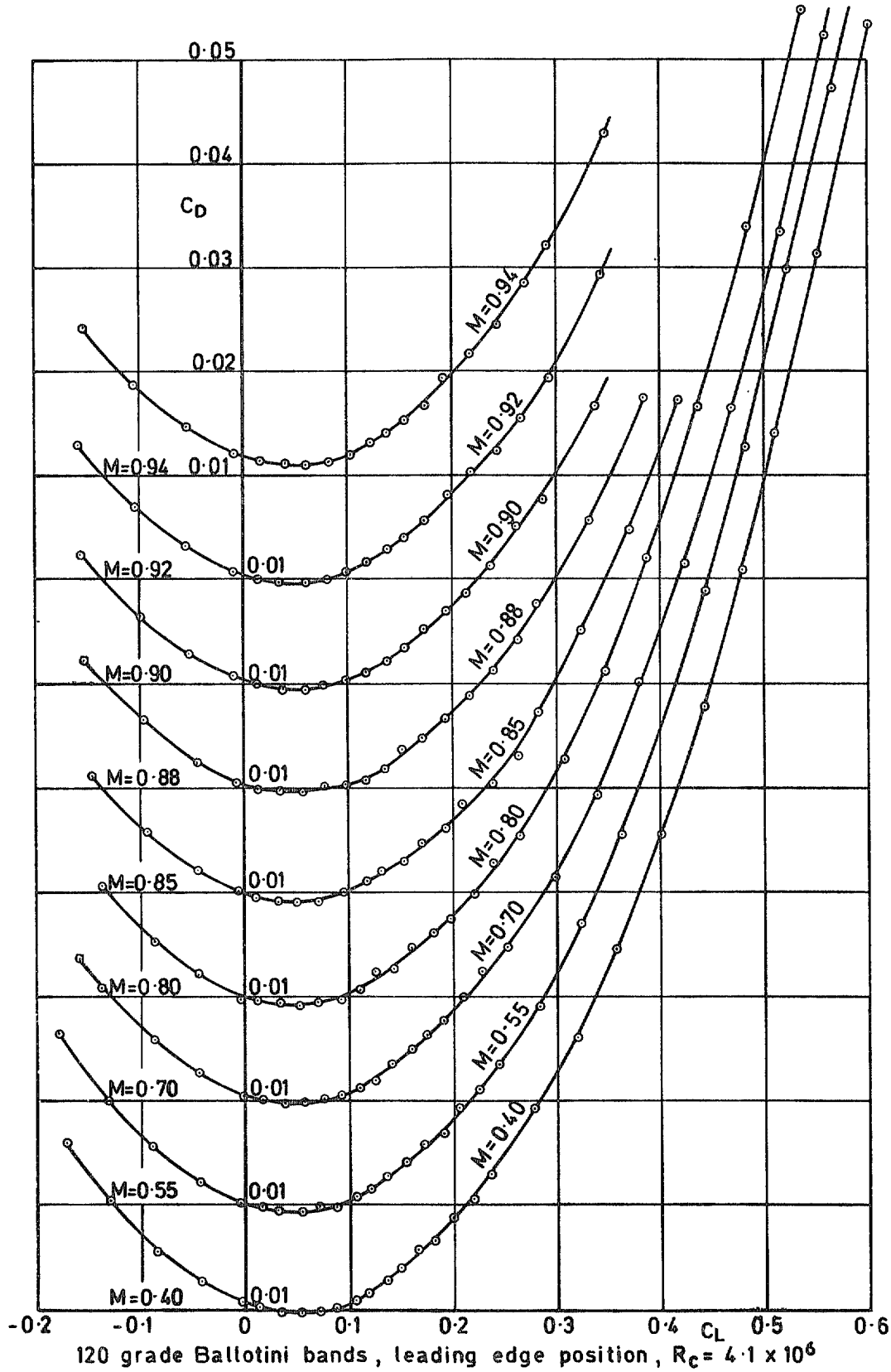

Fig 29 Variation of C_D with C_L, M = 0.40 to 0.94

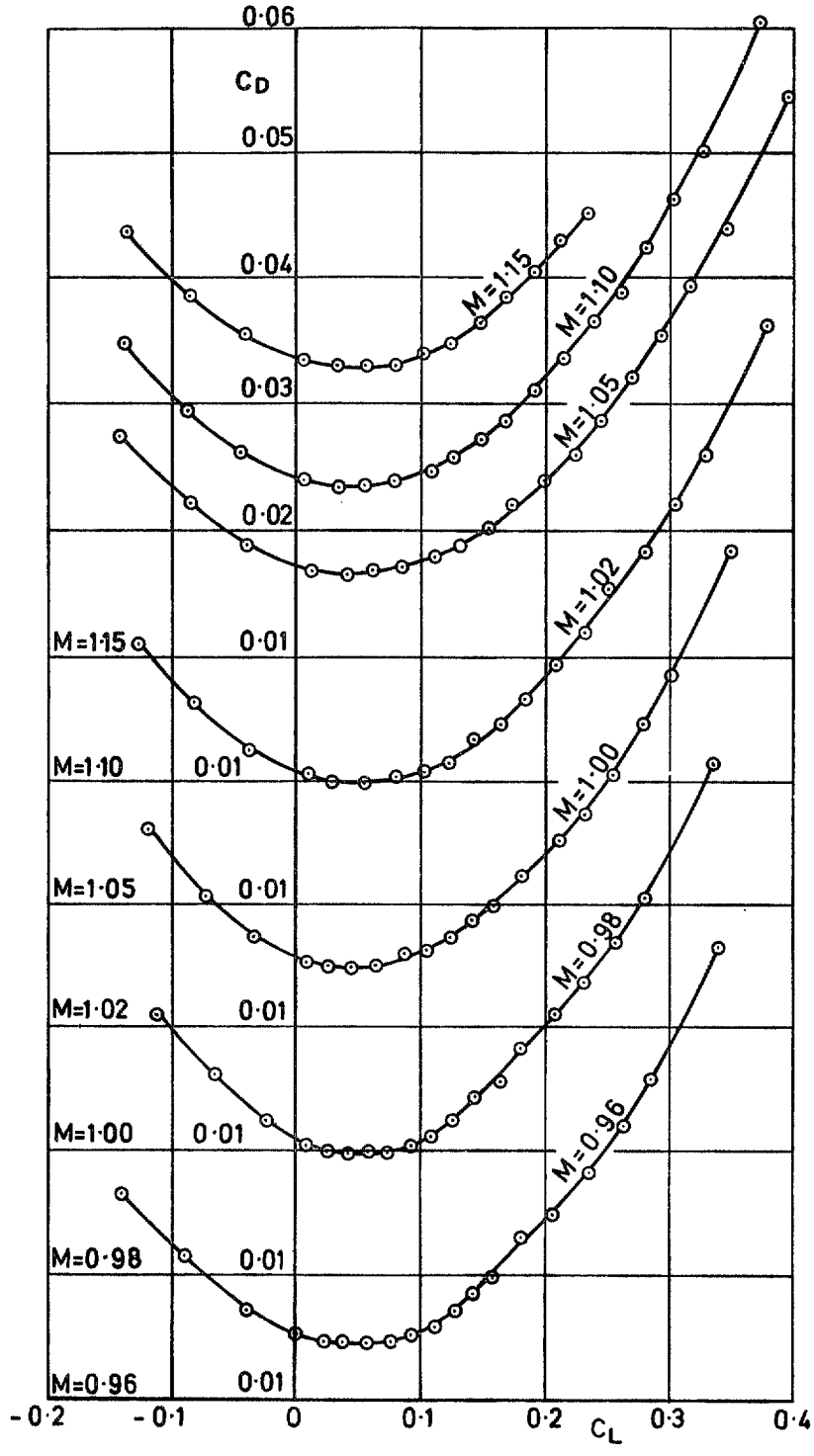

120 grade Ballotini bands , leading edge position, $R_c = 4 \cdot 1 \times 10^6$

Fig 30 Variation of C_D with C_L , M = 0.96 to 1.15

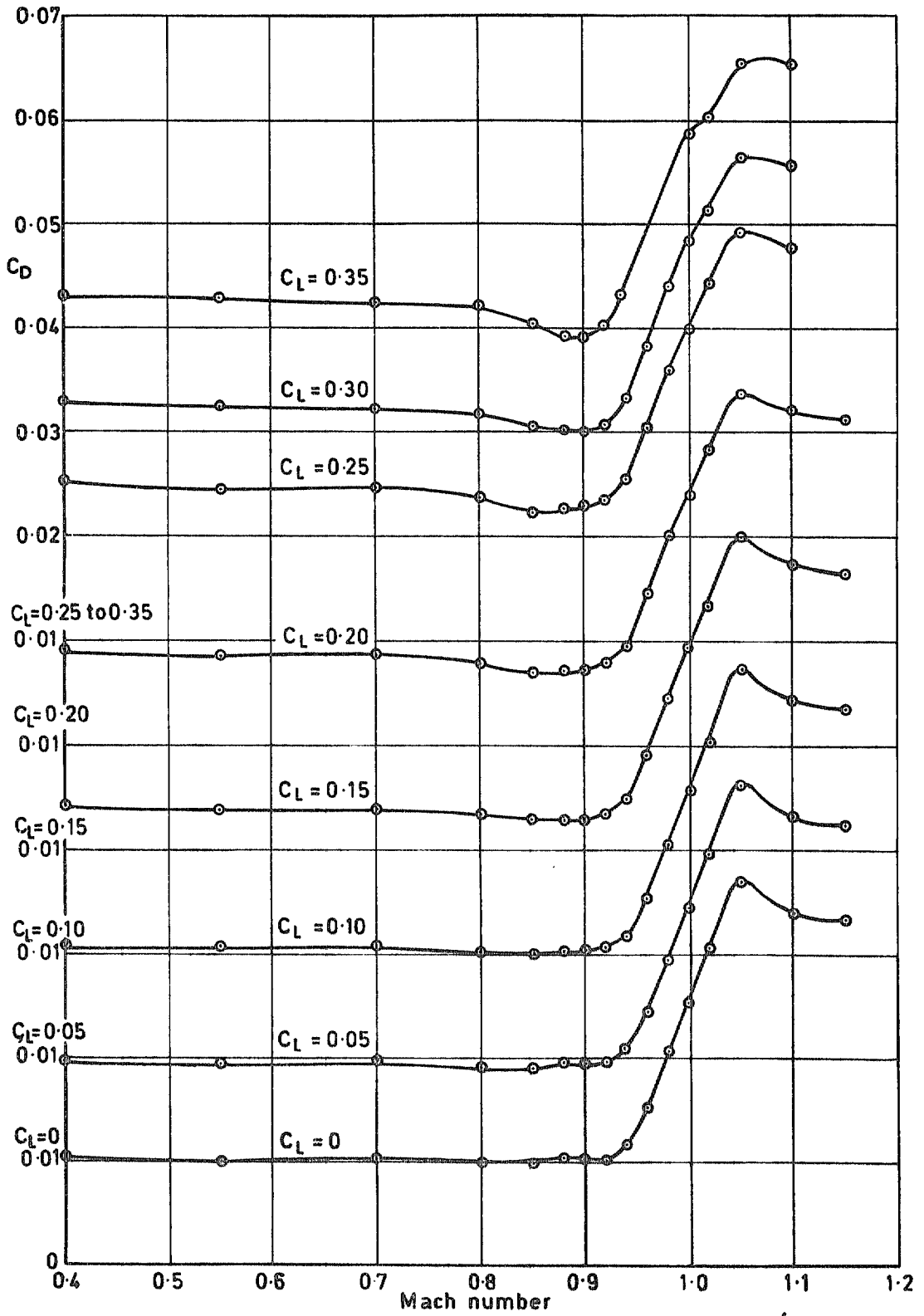

Fig 31 Variation of C_D with Mach number, at constant C_L

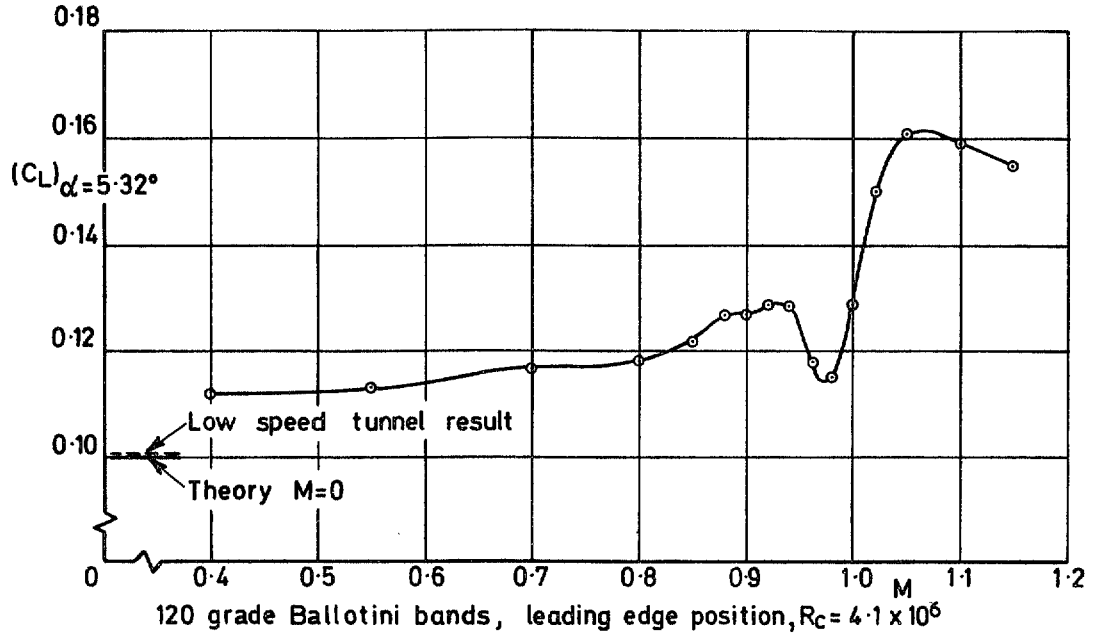

Fig 32 Variation of $(C_L)_{\alpha}$ design with Mach number

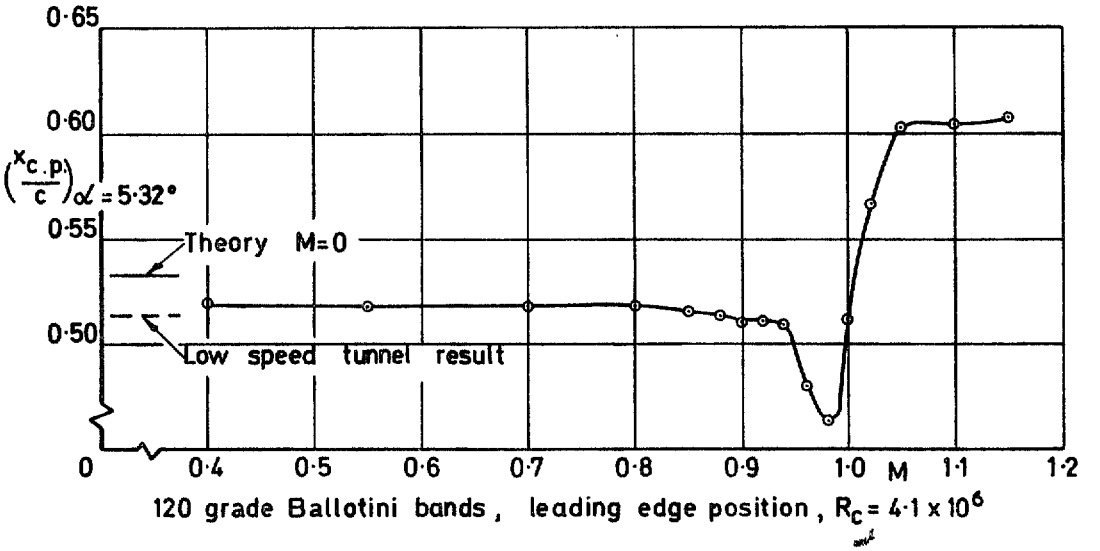

Fig 33 Variation of $(x_{c.p.}/c)_{\alpha}$ design with Mach number

Printed in England for Her Majesty's Stationery Office by the Royal Aircraft Establishment, Farnborough. Dd. 586386 K4 10/78.

Published by
HER MAJESTY'S STATIONERY OFFICE

Government Bookshops
49 High Holborn, London WC1V 6HB
13a Castle Street, Edinburgh EH2 3AR
41 The Hayes, Cardiff CF1 1JW
Brazennose Street, Manchester M60 8AS
Southey House, Wine Street, Bristol BS1 2BQ
258 Broad Street, Birmingham B1 2HE
80 Chichester Street, Belfast BT1 4JY

Government Publications are also available through booksellers

R &M No.3827
ISBN 0 11 471160 7